RAMAN SCATTERING AND SYNCHROTRON X-RAY DIFFRACTION STUDIES ON RARE-EARTH BASED FUNCTIONAL OXIDES

A Thesis
Submitted for the Degree of

Doctor of Philosophy

By

VENKATA SRINU BHADRAM

CHEMISTRY AND PHYSICS OF MATERIALS UNIT
JAWAHARLAL NEHRU CENTRE FOR ADVANCED SCIENTIFIC RESEARCH
BANGALORE – 560 064, INDIA.
MARCH 2014

Dedicated to

My Family

DECLARATION

I hereby declare that the matter embodied in this thesis entitled “**Raman scattering and synchrotron x-ray diffraction studies on rare-earth based functional oxides**” is the result of the investigations carried out by me in the Chemistry and Physics of Materials Unit, Jawaharlal Nehru Centre for Advanced Scientific Research (JNCASR), Bangalore, India, under the supervision of Professor Chandrabhas Narayana.

In keeping with the general practice of reporting scientific observations, due acknowledgements have been made whenever the work described is based on the findings of other investigators. Any omission which might have occurred by oversight or error in judgement is regretted.

(Venkata Srinu Bhadram)

CERTIFICATE

I hereby certify that the matter embodied in this thesis entitled "**Raman scattering and synchrotron x-ray diffraction studies on rare-earth based functional oxides**" has been carried out by Mr. Venkata Srinu Bhadram at the Chemistry and Physics of Materials Unit, Jawaharlal Nehru Centre for Advanced Scientific Research (JNCASR), Bangalore, India under my supervision and that it has not been submitted elsewhere for the award of any degree or diploma.

Prof. Chandrabhas Narayana

(Research Supervisor)

ACKNOWLEDGEMENTS

I take this opportunity to acknowledge people who have inspired, motivated and supported me by sharing their knowledge and wisdom. It's a matter of pleasure to extend my gratitude to all of them who had a great impact on my academic as well as personal life.

First of all, I had been extremely fortunate to get a wonderful mentor like Prof. Chandrabhas Narayana. I would like to thank him and convey my deepest sense of gratitude for providing excellent guidance, immense support, enormous freedom in workplace and giving an opportunity to work on wide variety of scientific problems. He has been very supportive in my professional as well as personal life. All this has been crucial in making me a better scientist and a good human being. I shall always remember his extraordinary energy and enthusiasm in everything that he does.

I want to thank Prof. C. N. R. Rao for his never ending enthusiasm for science. He continues to be a source of inspiration for many of us.

I would like to thank all of my collaborators Prof. A. Sundaresan (JNCASR, Bangalore), Prof. P. S. Anil Kumar (IISc, Bangalore), Prof. C. N. R. Rao (JNCASR, Bangalore), Dr. A. Murugavel (University of Delhi, New Delhi), Prof. Timothy Fisher (Purdue University, USA), Prof. G. U. Kulkarni (JNCASR, Bangalore), Dr. Pranab Mandal (JNCASR, Bangalore), Dr. Narendra (JNCASR, Bangalore), Dr. Kaustuv Manna (IISc, Bangalore), Mr. Viswanathan (IISc, Bangalore), Mr. Bharath Rajeswaran (JNCASR, Bangalore), Dr. Diptikanta Swain (JNCASR, Bangalore),Dr. Gopal K Pradhan (JNCASR, Bangalore), Dr. Papia Chowdhury (Jaipee University, Gurgaon). I have learnt a lot from the scientific discussions which we had. Particularly, I would like to thank Dr. Gopal K. Pradhan who has introduced me most of the experimental techniques present in our lab. Also, special thanks to Dr. Diptikanta Swain from whom I *learnt basics of crystallography and Rietveld refinement method. I would also like to take this opportunity to thank Dr. Maurizio Polentarutti, Mr. Giorgio Bais and Mr. Nicola Demitri for the help at XRD beamline in Elettra.*

I am pleased to acknowledge Prof. Alain Polian (UPMC, Paris) and Dr. Sandercock (JRS Co.) who spent couple of days in the lab and taught me the critical alignment procedures of Brillouin spectrometer which helped in a big way.

I would like to thank the faculties of CPMU, TSU, Prof. A. K. Sood, Prof. T. N. Guru Row (IISc) for their wonderful courses. I had some useful discussions with Prof. Umesh V. Waghmare. I thank him for that.

I had some amazing lab mates (past and present) like Drs Gopal, Dipti, Navneet, Santosh, Sorb; Partha, Soumik, Ritu, Gayatri, Dhanya, Rajaji, Shantanu, Jyothi. We had lots of fun together and had wonderful scientific discussions. They have always kept the lab atmosphere a terrific place to work. I thank all of them. A special thank to Gayatri and Dhanya for their critical reading of my thesis. I thank Sujith and Shiva who spent couple of months with me in the lab. I thank them for their help in some of the experiments.

I would also like to thank my batch mates, friends at JNCASR. Few of them need special mention. They are Sandeep, Narendra, Dasari, Dhanya, Sharma, Pandu, Krishna, Malli, Tangi, Satya, Karthik, Bharath. I thank all of them for their support and encouragement.

It's my pleasure to thank some wonderful friends, seniors from my MSc and BSc days. The list includes Venkat, Priyanka, Rama Krishna, Sunil, Sanved, Padmanath, Krishna, Bharath, Bavan, Trinath, Vijay. I would like to thank all these wonderful and sweet personalities for making my life memorable and pleasant.

I express my heartfelt thank to all the academic, technical, library and computer lab staff members of JNCASR. A special thank to Mr. Arokyanathan, who has been instrumental in fabricating many of our experimental designs.

I have been very fortunate to be taught by many great teachers during my MSc, BSc and +2 days. I thank all of them. Prof. G. D. Varma has provided me outstanding support during my MSc days. I would also like to thank three outstanding teachers Mr. Madhu Srinivas, Mr. Chandrashekar, Mr. Radha Krishna who have influenced me in a big way and are the main motivation to choose research as my career.

I acknowledge CSIR, India for fellowship and contingency grants sanctioned to me. I would also like to acknowledge DST, India for the travel award to attend MRS spring meeting 2013 and financial support for my trip to Elettra, Trieste.

I would like to take this very special opportunity to thank my family who have been very supportive and I dedicate this work to them.

Contents

Chapter 1 Introduction

Chapter 2 Experimental techniques

Chapter 3 Influence of lattice distortion on Curie temperature and spin-phonon coupling in $LaCo_{0.5}Mn_{0.5}O_3$

Chapter 4 Raman scattering studies on spin-phonon coupling in multiferroic *R*CrO_3 (*R*= Y, Lu, Gd, Eu, Sm).

Chapter 5 Effect of pressure on the octahedral distortions in RCrO3: A Raman scattering study

Chapter 6 Structural aspects of *R*CrO$_3$ (*R* = Gd, Eu, Sm) as a function of pressure

Preface

This thesis is unified based on the sensitivity of the Raman scattering in probing the structural distortions and thereby understanding the intriguing physical properties of some of the rare-earth functional oxides as a function of temperature and pressure. Apart from Raman scattering, for structural characterization as a function of pressure, synchrotron powder x-ray diffraction (XRD) has also been used. This thesis is divided into seven chapters. Introduction to Raman scattering and brief overview of structural aspects of perovskites based functional oxides is included in chapter 1. A detailed description of the experimental techniques utilized for the present work has been included in chapter 2. Raman scattering studies on the two distinct Curie temperature (T_c) behaviour in $LaCo_{0.5}Mn_{0.5}O_3$, spin-phonon coupling in multiferroic rare-earth chromites ($RCrO_3$), and pressure induced evolution of structural distortions in $RCrO_3$ each carries a chapter. Last chapter presents pressure dependent synchrotron XRD studies on $RCrO_3$. Each chapter includes topical introduction on the problem which is being addressed.

Chapter 1 accounts a thorough introduction about the general aspects of Raman scattering and the fundamental excitations which affects the Raman scattering. Effect of temperature and pressure on materials is also touched upon. Also, there is a brief overview on the perovskite oxides and how various structural distortions in these oxides affect the physical properties is discussed.

Chapter 2 describes the experimental details which include the design and working principle of Raman setup and the methods of doing high pressure experiments. Also, there is a brief overview on the powder x-ray diffraction experiments at synchrotrons.

Chapter 3 discusses the Raman studies on polycrystalline and single crystalline $LaCo_{0.5}Mn_{0.5}O_3$ (LMCO). Here we have addressed the two distinct T_c behaviour of LMCO by analysing the distortion dependent Raman modes. From the temperature dependence of Raman modes, through the spin-phonon coupling phenomenon, we have found the co-existence of two magnetic phases in LMCO.

Chapter 4 presents our temperature dependent Raman studies on rare-earth chromites, RCrO$_3$ (R=Y, Lu, Gd, Eu, Sm) which exhibit an intriguing magnetoelectric coupling below the Néel temperature of Cr^{3+} only in the case of magnetic rare-earth (Gd, Sm). We have investigated the origin of ferroelectric property by analysing the temperature dependence of Raman modes. From the temperature dependence of Raman line widths, we found the presence of spin –phonon coupling in $GdCrO_3$ and $SmCrO_3$, which could be a possible reason for the observed multiferroicity in these systems.

In **Chapter 5** we have studied pressure induced evolution of octahedral distortions in RCrO$_3$ for the first time using Raman scattering. From our study we found a critical rare-earth size, above which distortions in RCrO$_3$ decrease with pressure. Our study explains the contrasting reports on the pressure dependent behaviour of $YCrO_3$ and $LaCrO_3$.

Chapter 6 deals with high pressure synchrotron XRD studies on RCrO$_3$ (R=Gd, Eu, Sm). We have calculated the cell distortion factor to estimate the distortions in the lattice and from this we found a critical rare-earth size above which distortions decrease with pressure and is in close agreement Raman results in chapter 5, thereby giving further support to our claims. We have also described the corresponding implications in pressure dependent change in T_N.

Chapter 7 describes brief summery and future directions of the present thesis.

Chapter 1

Introduction

1.1 Raman scattering:

When light interacts with a medium, it is either transmitted or absorbed following the laws of reflection and refraction, but a tiny fraction is scattered by inhomogeneties in the medium. These inhomogeneties can be static or dynamic. Scattering from defects and dislocations in a crystal is considered as static and light scatters elastically from them. Fluctuations in the optical inhomogeneties in the medium that are associated with lattice vibrations (phonons or vibrons) are the examples of dynamic scatterers. They inealstically scatter the light. Raman scattering is an inelastic scattering of light which occurs due to the interaction of the light with elementary excitations (quasi-particles) of the matter such as optical phonons, polaritons, magnons, plasmons and vibrons in liquids and gases.

In Raman scattering, the incident photon with momentum $\hbar k_i$ and energy $\hbar \Omega_i$ interacts with the medium resulting in a scattered photon of momentum $\hbar k_s$ and energy $\hbar \Omega_s$.

Based on laws of conservation:

$$\hbar k_i \pm \hbar k_s = \hbar q \tag{1.1}$$

$$\hbar \Omega_i \pm \hbar \Omega_s = \hbar \omega_p \tag{1.2}$$

Here $\hbar q$ and $\hbar \omega_p$ are the momentum and energy of the photon transferred to the medium. In case of Raman scattering there will be an energy transfer from these photons for creation or annihilation of a phonon with frequency ω_p and wave vector q.

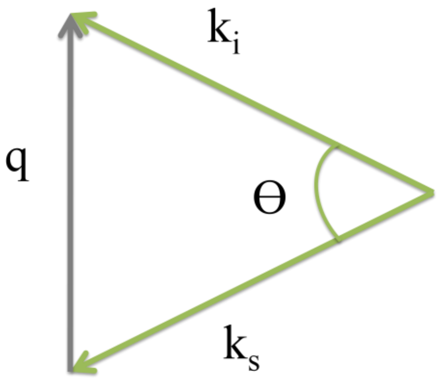

Figure 1.1: Schematic representation of scattering geometry.

As shown in the Fig. 1.1, the direction of phonon wave vector depends on the scattering geometry (determined by angle ϴ). In a backscattering geometry (ϴ =180^0), the maximum allowed value of q (q_{max}) is obtained from Eq. (1.1) as,

$$q_{max} = k_i + k_s \approx 2k_i \tag{1.3}$$

Here k_i is of the order of 10^5 cm^{-1} for visible light, which is much smaller than the size of the Brillouin zone (~10^8 cm^{-1}). So, in 1st order inelastic light scattering process, one probes the crystal excitations very close (q ~ 0) to the Brillouin zone centre i.e., Γ-point (see Fig. 1.2).

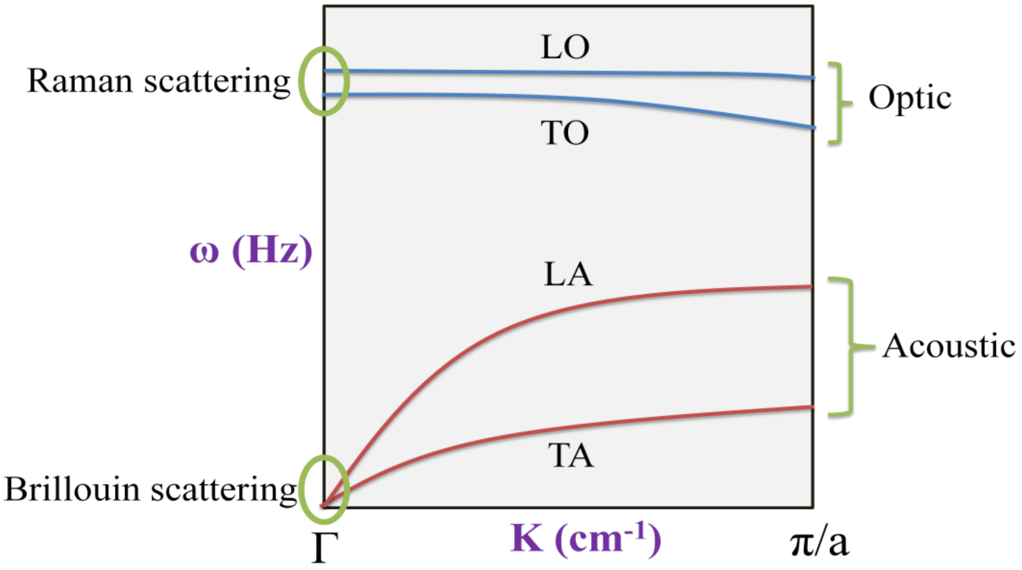

Figure 1.2: schematic representation of the dispersion relation of phonons in a lattice.

In higher order processes, the individual phonon wave vector can span from zero to the entire length of the first Brillouin zone. Hence a second order Raman gives the density of states (DOS) of phonon.

1.1.1 Classical theory of Raman scattering:

When a medium is subjected to an oscillating electromagnetic radiation $E = E_0 e^{i\Omega t}$, it induces a polarization in the crystal. The induced polarization can be written as $P = \alpha E$, where α is the polarizability of the molecule. In the case of the crystals, the polarizability is replaced with a susceptibility tensor χ_{ij}. This susceptibility will be modified due to atomic or lattice vibrations. Since polarizability is a function of the displacement coordinate of the normal mode, the modified susceptibility can be expanded in Taylor series (since these vibrations are simple harmonic motion in the first approximation)

$$\chi_{ij} = (\chi_{ij})_0 + \sum_k \left(\frac{\partial \chi_{ij}}{\partial Q_k}\right)_0 Q_k + \sum_{k,m} \left(\frac{\partial^2 \chi_{ij}}{\partial Q_k \partial Q_m}\right)_0 Q_k Q_m + \text{higher order terms} \qquad (1.4)$$

where the sum runs over all the normal coordinates. The second term $\left(\frac{\partial \chi_{ij}}{\partial Q_k}\right)_0$ is called the "Raman tensor" for a particular normal mode of vibration with wave vector k. Here, $Q_k = Q_0 e^{\pm i\omega_k t}$ is the normal coordinate of the atomic displacements with frequency ω_k expressed as Bloch wave. The induced polarization can be written as

$$P_i = \chi_{ij} E_{0j} e^{i\Omega t}$$

$$P_i = (\chi_{ij})_0 E_{0j} e^{i\Omega t} + \sum_k \left(\frac{\partial \chi_{ij}}{\partial Q_k}\right)_0 Q_0 E_{0j} e^{i(\Omega \pm \omega_k)t} + \sum_{k,m} \left(\frac{\partial^2 \chi_{ij}}{\partial Q_k \partial Q_m}\right)_0 Q_0{}^2 E_{0j} e^{i(\Omega \pm \omega_k \pm \omega_m)t}$$

$$+ \text{.... higher order terms.} \qquad (1.5)$$

The above expression is a linear combination of three oscillating induced dipoles for each normal modes with frequencies Ω, $\Omega+\omega$ (anti-stokes) and $\Omega-\omega$ (stokes). The radiated intensity (I) from an oscillating dipole is proportional to $\left|\frac{d^2p}{dt^2}\right|$, so one can write,

$$I \propto \Omega_i^4 (\chi_{ij})_0^2 E_{0j}{}^2 + \Omega_s^4 \left(Q_0 E_{0j} \frac{\partial \chi_{ij}}{\partial Q_k} Q_k\right) + \text{higher order terms} \qquad (1.6)$$

First term in Eq. (1.6) corresponds to the intensity due to Rayleigh while the second term is related to the intensity of the Raman scattering. For the visible light, as the phonon frequencies are much smaller compared to the excitation frequency, one can write $\Omega_i = \Omega_s$; so the Raman intensity varies as Ω_i^4.

The partial derivatives in Eq. (1.6) constitute the polarizability tensor, also called as Raman tensor ξ which is a second rank tensor and can be written as

$$\xi = \left(\frac{\partial \chi}{\partial Q}\right)_0 \hat{Q}_0(\omega) \qquad (1.7)$$

and the corresponding Raman intensity is given by

$$I_S \propto |\hat{e}_s.\xi.\hat{e}_i|^2 \tag{1.8}$$

where $\hat{e}_s$ and $\hat{e}_i$ are the directions of the incident and scattered radiation. So, it is clear that the intensity of the Raman line mainly depends on the scattering geometry and the symmetry of the vibration. Though the macroscopic theory described above predicts the Raman intensities qualitatively, it cannot predict the magnitude and the frequency variations of the susceptibility derivatives. Thus, it becomes necessary to set up a quantum mechanical picture to describe the scattering cross-section. It should be noted here that the classical picture is sufficient, without loss of generality, to explain the Raman phenomenon. It is only to have a quantitative understanding one needs to invoke quantum mechanics.

1.1.2 Quantum theory of Raman scattering:

The first order Raman process can be explained using quantum mechanics in the time dependent third order perturbation theory. This process involves an intervention of electronic excitations. The interaction of electrons with photons and phonons leading to the scattering of phonons can be explained in three steps;[1-3] 1) the incident photon excites the electron from its ground state $|i\rangle$ to a virtual state $|f\rangle$ by creating an electron-hole pair, 2) the excited electron (hole) interacts with the lattice and either gives away its energy or absorbs energy from phonon which gives rise to either creation (stokes process) or annihilation (anti-stokes process) of phonons and 3) finally, the electron recombines with the hole leading to the emission of the scattered photon. A schematic description of the above process is shown in Fig. 1.3.

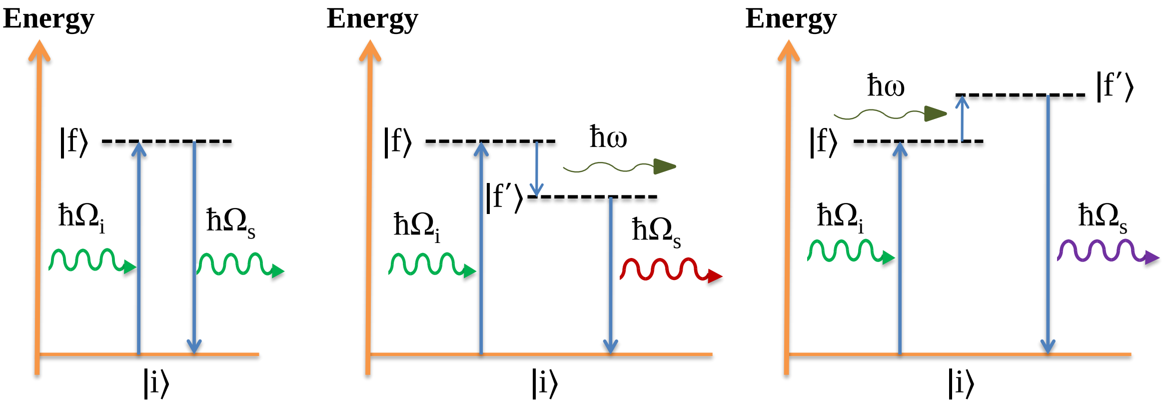

Figure 1.3: Schematic representation of Rayleigh, Stokes and anti-Stokes Raman processes.

Using the combination of the above three process, the scattering cross section in third order perturbation theory can be written as [1]

$$|\hat{e}_s.\xi.\hat{e}_i| \sim \frac{\langle i|H_{ep}|f\rangle\langle f|H_{eph}|f'\rangle\langle f'|H_{ep}|i\rangle}{(E_f - \hbar\Omega_s)(E_{f'} - \hbar\Omega_i)} \tag{1.9}$$

Here H_{ep} is the Hamiltonian which describes the electron-photon interaction and the H_{eph} describes electron-phonon interaction. $|f'\rangle$ is an intermediate electronic state. E_f, $E_{f'}$, $\hbar\Omega_s$ and $\hbar\Omega_i$ are electronic energy levels as shown in the Fig. 1.3. In the normal Raman scattering process, the virtual energy state $|f\rangle$ cannot be a real electronic state, which is the reason why the Raman process is weaker than the fluorescence. However, when $|f\rangle$ becomes a real electronic state, the scattering cross section will enhance (by a factor of 10^6) drastically and is called as resonant Raman scattering.

The differential scattering cross section in terms of the solid angle $d\Theta$ with a scattering frequency between Ω_s and $\Omega_s + d\Omega_s$ can be written

for Stokes process as,

$$\frac{d^2\sigma}{d\Theta d\Omega_s} = vV\frac{\hbar\Omega_s^4}{2N\Omega_i c^4}|\hat{e}_s.\xi.\hat{e}_i|^2(n(\omega)+1)g_i(\omega) \tag{1.10}$$

for anti-Stokes process as,

$$\frac{d^2\sigma}{d\Theta d\Omega_s} = vV\frac{\hbar\Omega_s^4}{2N\Omega_i c^4}|\hat{e}_s.\xi.\hat{e}_i|^2 n(\omega)g_i(\omega) \tag{1.11}$$

Where $g_i(\omega)$ is the spectral line shape function, often taken to be a Lorentzian, N is the number of oscillators, $n(\omega) = \left[e^{\hbar\omega/2KT} - 1\right]^{-1}$ is the Bose-Einstein thermal population factor for phonons. It is clear from the Boltzmann factor that the phonons in the excited states are less populated compared to the ground states. Thus, the Stokes lines should be of higher intensity compared to anti-Stokes lines. From Eqs.(1.10) and (1.11), one can show

$$\frac{I_{Stokes}}{I_{anti\ -Stokes}} = \left[\frac{\Omega_{i-\omega}}{\Omega_i + \omega}\right]^4 e^{\frac{\hbar\omega}{KT}} \tag{1.12}$$

Using the above relation, from the intensity ratio of Stokes and anti-Stokes Raman of a particular vibration, one can measure the in-situ sample temperature.[4]

It is clear from the Eqs. (1.10), (1.11) that the scattering efficiency depends on *i) incident light frequency* Ω_i; As the incident and scattered light frequencies are almost the same we can say that the scattering intensity increases as Ω_i^3, *ii) scattering volume* V; which increases with increase in the penetration depth ($d = \frac{\lambda_i}{\kappa}$, κ is absorption coefficient), hence, the scattering volume can be increased by increasing λ_i and *iii) scattering geometry, symmetry of the vibration which are included in* $|\hat{e}_s.\xi.\hat{e}_i|$; incident and scattered light polarizations ($\hat{e}_s$ and $\hat{e}_i$) pick a particular set of components in the scattering tensor ξ which contribute to the intensity of the corresponding Raman line. The components of the scattering tensor will be decided by the crystal symmetry and the symmetry of the particular vibrational mode. Group theory enables the determination of the vibrational species which can have non-vanishing components in the scattering tensor. The list of the scattering tensors for different point groups and the corresponding polarization selection rules are listed elsewhere in great detail.[2,3,5,6] In the next subsection, there will be a brief discussion on how symmetry can be imparted to the lattice vibrations. This information is useful in understanding the mode assignments discussed in the following chapters of this thesis.

1.1.3 Symmetry consideration of the vibrational modes:

In general, if Q_i is a normal coordinate of the vibration and R is a symmetry operator, then,

$$RQ_i = \pm Q_i \begin{cases} if\ RQ_i = +Q_i, & Symmetric \\ if\ RQ_i = -Q_i, & anti-symmetric \end{cases} \tag{1.13}$$

Symmetry of the modes are represented by using Mulliken symbols (*A, B, E* and *T(F)*).[7] *A* and *B* are designated to single, non-degenerate modes, which are respectively, symmetric and anti-symmetric with respect to a rotation about principal axis. For example, H_2O molecule with C_{2v} group will contain two symmetry elements; namely, C_2 axis (principal axis, “Z”) and σ_v (vertical plane XZ of symmetry). The vibrational modes ν_1 and ν_2 are symmetric with respect to both C_2 and σ_V, whereas ν_3 is anti-symmetric (as shown in Fig. 1.4). The subscripts 1 and 2 are used when the mode is respectively, symmetric and anti-symmetric with respect to a C_2 axis or vertical plane of symmetry. In case of H_2O it happens to be the only symmetry elements available. Subscripts *g* (gerade) and *u* (ungerade) are used when the modes are respectively, symmetric and anti-symmetric with respect to inversion centre. The modes which are doubly degenerate are represented with *E* and the modes which are triply degenerate are represented with *T or F*.

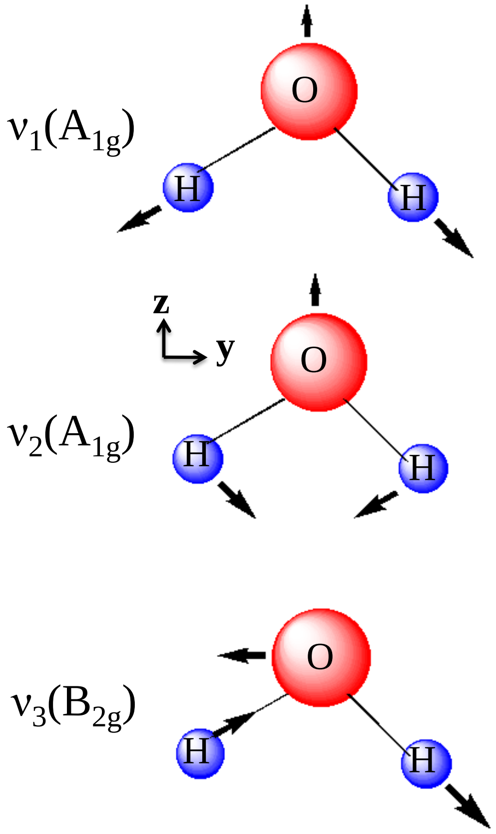

Figure 1.4: Schematic representation of the normal modes of vibration in H_2O.

1.2 Various interactions which affect phonons:

Phonons often interact with fundamental particles like electrons, atomic spins and even with other phonons. These interactions affect the phonon mode parameters like frequency, linewidth and intensity in the light scattering experiments. This is an important information, which an absorption process is devoid off. The onset of interactions in the light scattering experiments can be seen by varying the thermal parameters like temperature and pressure. To understand the effect of temperature on the phonon modes, one has to consider the phonon-phonon interactions (anharmonicity). Apart from this, in magnetic systems, below the spin-ordering temperature, there will be additional effects due to spin-ordering. Electron-phonon interactions can lead to exciting changes in the transport properties of materials. For example, superconductivity is believed to be the result of electron-phonon interactions. Detailed theoretical and experimental illustration on electron-phonon coupling can be found elsewhere. [8-10] Here, we discuss the effects of anharmonicity and spin-phonon interactions on the Raman modes. This discussion is useful in understanding the temperature dependence of the Raman mode parameters of material systems discussed in Chapters 1 &2.

1.2.1 Anharmonicity (phonon-phonon interactions):

The classical harmonic approximation holds good for small oscillations. In this case, the theory of lattice vibrations is limited in the potential energy to quadratic terms of the atomic displacements. But this theory cannot explain the thermal expansion phenomenon, the dependence of the elastic constants on the thermodynamic parameters and Dulong-Petit’s law etc. In a harmonic crystal (ideal system) with N-oscillators, there will be 3N normal modes. For a particular wave vector *k*, each normal mode has energy [11]

$$(n_k + {}^1\!/_2)\hbar\omega(k) \tag{1.14}$$

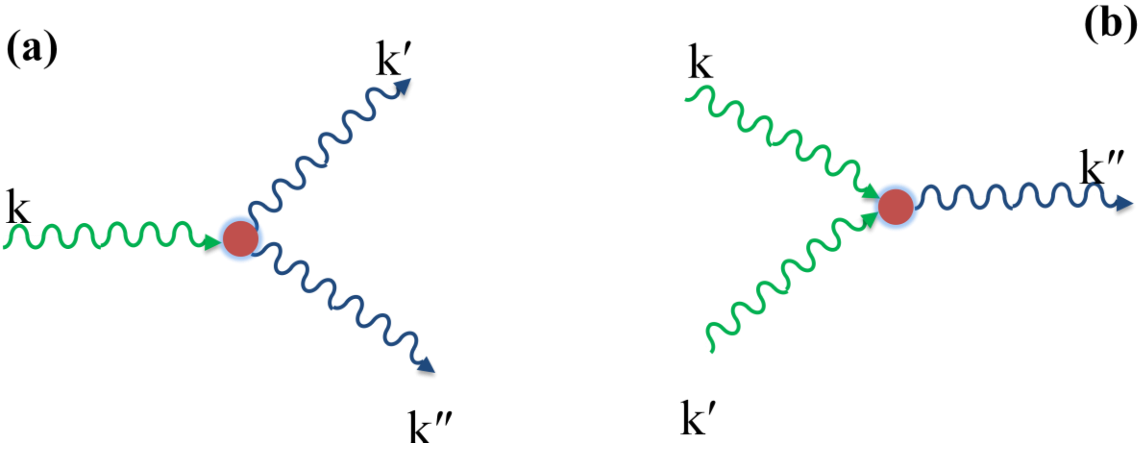

Figure 1.5: Schematic depicting the cubic anharmonic process where (a) one phonon decays into two other phonons, (b) two phonons could merge and form another phonon.

where “n_k” is the excitation number of normal mode (n_k = 0, 1, 2, …). n_k can also be treated as the number of phonons with wave vector *k* present in the crystal.

In a perfectly harmonic crystal, phonon states are stationary, and the distribution of phonons is unaltered with time. Whereas, in real systems, at non-zero temperatures, phonon occupation number n_k is no more a constant due to the presence of phonon-

phonon interactions (anharmonicity). The dependence of n_k on temperature can be given by the Bose-Einstein distribution as:

$$n_k = \frac{1}{e^{\hbar\omega(k)/KT} - 1} \tag{1.15}$$

where K is Boltzman constant. These processes are analogous to the collisions of particles in a thermodynamic system explained by Boltzman equation. In this analogy, phonon relaxation time (τ_{ph}), which is the time elapsed between the collisions, is nothing but the lifetime of the phonons. It is important to note that the finite width (Γ) of the Raman lines is mainly due to a) the anharmonicity and b) inversely proportional to the lifetime of the phonons.

In a cubic anharmonic process (adding third term to the harmonic potential), a phonon can decay into two other phonons or two phonons can merge to form a single phonon. These processes are illustrated clearly in Fig.1.5. The corresponding changes in the phonon linewidth and frequency can be written in the following way:

$$\Gamma_T = \Gamma_0 - A\left(1 + \frac{2}{e^{\hbar\omega_0/2KT} - 1}\right) \tag{1.16}$$

$$\omega_T = \omega_0 + B\left(1 + \frac{2}{e^{\hbar\omega_0/2KT} - 1}\right) \tag{1.17}$$

where A, B are fitting parameters. When dealing with temperature much below the melting point of the system, the cubic terms in the anharmonic potential work well to explain the temperature dependence of the Raman lineshapes as well as many other physical properties of the system. Higher order terms can also be used while dealing with very high temperatures.

1.2.2 Spin-phonon coupling:

Light scattering in magnetic materials has long been a fascinating subject for scientists. It all started with Bloch who introduced spin waves (magnons) which are low-lying excitations in ordered magnetic materials. Spin waves can be explained as a disturbance in an ordered spins which propagates like a wave through the crystal. Though, the early experimental evidence of magnons came from measurements of thermodynamic properties, a direct observation of magnons is possible through light scattering experiments other than neutron scattering experiments. These magnons in a magnetic material can cause spatially periodic modulation of permittivity of the medium and the light scattered from these permittivity fluctuations results in the observation of magnons in light scattering experiments.[12] The typical energies of the magnons are of the order of a few μeV.

Apart from magnons, the magnetic ordering has a direct influence on the phonons which is termed as spin-phonon coupling (Fig. 1.6). Raman line parameters like mode frequency, linewidth and intensity will be modified around the spin-ordering temperatures in magnetic materials. The phonon frequency (ω_T) in magnetic materials below magnetic ordering temperature can be written as [13,14]

$$\omega_T = \omega_0 \pm \kappa < S_i . S_j > \tag{1.18}$$

where, ω_0 is frequency in the absence of coupling, S_i, S_j are spins in two neighbouring sublattices and κ is coupling constant. Coupling constant κ caries the information related to the type of magnetic ordering. Phonon frequency can decrease (mode softening) or increase (mode hardening) depending on the type of interactions.

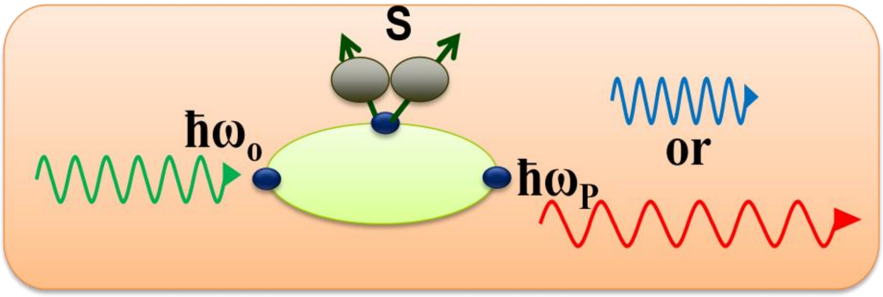

Figure 1.6: Schematic depicting spin-phonon coupling.

Granado *et al.* [15] have derived the theoretical formulation for the spin-ordering effects on phonons. According to them, the effective Hamiltonian for a spin system is given as:

$$H_S \approx -\sum_{ij} J_{ij} \; < S_i . S_j > \tag{1.19}$$

where J_{ij} is spin-exchange integral. Due to spin-phonon coupling J_{ij} will be modified across the magnetic ordering temperatures. One can write J_{ij}^{α} , which is the change in J_{ij} due to the αth Raman active normal mode, in Taylor series expansion,

$$\Delta J_{ij}^{\alpha}\left(u_m^{\alpha}(t)\right) = [u_m^{\alpha}(t).\Delta_m] J_{ij} + \frac{1}{2}\,[u_m^{\alpha}(t).\Delta_m]^2 J_{ij} \tag{1.20}$$

where $u_m^\alpha(t)$ is the displacement vector of the m^th^ atom involved in the vibration. The frequency shift of the phonons due to magnetic ordering can be given as

$$(\Delta\omega_\alpha)_{sp-ph} \propto \sum_m u_m^\alpha \, D_{sp} u_m^\alpha \qquad (1.21)$$

D_{sp} is an operator related to the potential energy term in the Hamiltonian H_S. Depending on the spin system, one can quantify the coupling strength. For example, in A-type antiferromagnetic $LaMnO_3$, it was shown that the shift of the MnO_6 octahedral stretching mode frequency from its regular temperature dependence $(\Delta\omega_{str})_{sp-ph}$ is related to the bulk magnetisation (M) of the system.

$$(\Delta\omega_{str})_{sp-ph} \propto {[M_{sublatt}\,(T)]^2}/{4\mu_B} \qquad (1.22)$$

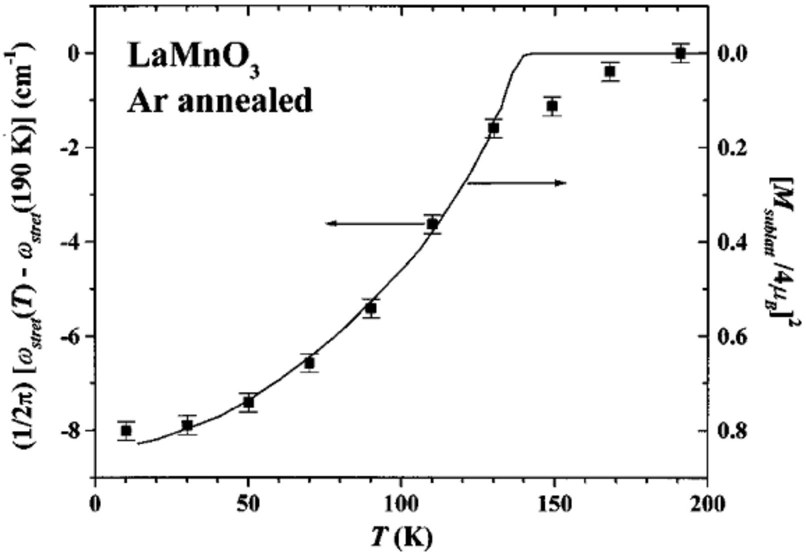

Figure 1.7: Temperature dependence of the shift of the octahedral stretching mode frequency with respect to its value at 190K for $LaMnO_3$. Solid line is $[[M_{sublatt}\,(T)]^2/4\mu_B]$ for an AFM $LaMnO_3$ sample with T_N = 140K (adopted from Ref. 4).

Proportionality constant is called the coupling constant which is a measure of the strength of the coupling. This can also help in modelling the magnetic structure. For the case of MnO_6 octahedral breathing mode in $LaMnO_3$, there is a good agreement between the experimentally observed softening of the mode and the above relation (shown in Fig. 1.7). Similarly, given the magnetic structure of the material, one can estimate the spin-phonon coupling strength of a particular Raman mode using the above methodology.

Similarly, there were attempts to estimate the spin-phonon coupling effects on the integrated intensities in Raman scattering. In this case, polarizability tensor is expanded in terms of the spin-operators.[16,17] Raman linewidths are related to the lifetime of the phonons. Coupling of the phonons with spin ordering causes the broadening of the phonon energy states and opening of new decay channels for the phonons. Thus, phonon lifetime decreases and correspondingly, Raman lines broaden due to spin-phonon coupling. This analogy has been used in Chapters 1 and 2 to explain the anomalous temperature dependent behaviour of Raman linewidths.

1.3 High pressure effects:

Pressure is one of the independent thermodynamic parameters which is more cleaner and stronger perturbation than temperature. Hydrostatic pressure induces only volume changes whereas temperature induces changes in the population of the excitations along with the expected volume change. For example, in Si, a pressure change of 10 GPa, produces a reduction in volume of 5%, whereas the total volume change due to increase in temperature from 0 K to melting is just 1.8%.

There are two important applications of high pressure technique in material science. 1) To synthesize novel materials (irreversible) which are not accessible by other techniques 2) To transform a given material from one phase to another phase (reversible). High pressure is used in synthesizing super hard materials like synthetic diamond and cubic boron nitride which are major commercial high pressure materials.[18-20] Also, amorphous and nanocrystalline diamond materials have been successfully synthesized from graphite, carbon nanotubes (CNTs) and fullerenes (for instance, C_{60}).[21-23] High pressure is a powerful tool for understanding electronic phenomenon in condensed phase. The electronic properties of the materials depend on the interactions of the outer electrons with the atoms, molecules or ions. Pressure perturbs the electronic orbitals and tunes the electronic properties of the materials which is called “pressure tuning”, examples of this kind include insulator-metal transitions. By exerting force on a small area, one can generate very high pressures. Using a simple diamond anvil-cell (DAC), pressure up to 5 megabar (500 GPa) has been achieved on tiny samples of size < 10 μm. Using DAC one can perform various characterizations at high pressures like X-ray diffraction, Raman scattering, infra-red, optical reflectivity and resistivity. [24] As it is relevant to the present thesis, pressure effects on Raman experiments will be discussed in the following sections.

1.3.1 Pressure effects on Raman mode parameters:

There are two major pressure induced changes in the Raman spectra of the materials: 1) pressure induced frequency shift and 2) pressure induced changes in the Raman line shape. Apart from these changes, one can also encounter changes in the selection rules due to pressure induced structural changes in the materials.

(a) Pressure - induced frequency shift:

As pressure induces reduction in the lattice volume, corresponding changes in interatomic distances clearly manifest themselves in the vibrational mode frequencies. The volume dependence of α^{th} normal mode frequency ω_α in an isotropically expanding (contracting) material can be written using Gruneisan's law,[25]

$$\frac{\partial V}{V} = -\gamma_\alpha \frac{\partial \omega_\alpha}{\omega_\alpha} \tag{1.23}$$

$$\text{or} \quad \gamma_\alpha = -\frac{\partial \ln \omega_\alpha}{\partial \ln V} \tag{1.24}$$

where Gruneisan parameter

$$\gamma_\alpha = -\frac{1}{\beta}\frac{\partial \ln \omega_\alpha}{\partial P} \tag{1.25}$$

where β is the isothermal volume compressibility. Here γ_α is independent of temperature and Grüneisan approximated that all γ_α's are the same i.e. $\gamma_\alpha = \gamma_{avg}$, which leads to a scaling law $\omega \propto V^{-\gamma_{avg}}$. This law holds well only when volume changes uniformly from all the directions in a crystal (isotropic). This happens only in covalently bonded 3D crystals. It breaks down in molecular crystals and ionic compounds. For example, in perovskite type materials (ABO_3 type), volume expansion (or contraction) is not uniform on the subunits of the lattice having different compressibilities (BO_6 and AO_{12} polyhedra). These issues have been explained in detail in the following chapters.

(b) Pressure - induced Raman lineshape changes:

Raman lineshape will be modified if the lifetimes of the phonons (τ_{ph}) are affected by pressure. Pressure directly doesn't change the lifetime of the phonons as it only changes volume, but indirectly, the volume change can increase or decrease certain types of interactions between excitations existing in the material. The lifetime of the phonons is inversely proportional to the linewidth of the Raman line. Thus, Raman linewidth is an important parameter as it results in anharmonic interactions among phonons causing their decay into combination of phonons of lower energy. Couple of classic examples include the pressure induced decrease in the phonon lifetimes in Si, Ge and SiC indicating the modification in phonon density of states and anharmonic decay of phonons, [26] pressure induced anharmonic decay of TO phonon into LA and TA phonons in GaP.[27] It is important to point out that the linewidth could also increase due to pressure induced amorphization, where the global ordering of the crystal is lost and trapped in a glassy state.

1.4 Functional oxides:

First example of functional oxides, perhaps the oldest oxide known is magnetite (Fe_3O_4) which was used by people in ancient Greece and China as a compass for navigating their boats across the sea. Similar iron oxide which is equally famous is hematite (Fe_2O_3) which has been used in magnetic recording tapes till recently. These two iron oxides happen to be magnetic oxides. The recent work on oxide materials led to the discovery of wide variety of physical properties like electrical/ionic conductivity, ferro/piezo electricity, magnetism, semi/super conductivity etc. These exciting properties have fascinating functionalities in devices like gas sensors, fuel cells, solar cells non-volatile memories etc.[28] There have been many groups of functional oxide materials known; zincite (AO), hematite (A_2O_3), rutile (AO_2), perovskites (ABO_3), spinel (AB_2O_4), garnets ($A_5B_3O_{12}$) are some of them. Among all these groups of oxides, perovskite oxides are widely studied due to its simple structure which can accommodate a variety of cations. The structural aspects of these perovskites oxides are addressed in the following subsections.

1.4.1 Perovskite oxides:

Perovskites are a group of materials with chemical formula ABO_3, where A and B are cations with different ionic radii. The atomic arrangement in a cubic perovskites is shown in Fig 1.8. It can be viewed in two ways. In one way, B-cation sits at the centre of the cube, surrounded by six oxygens in an octahedral geometry occupying the face centres of the cube and the A-cation sits at the corners of the cube. In another way, the A-cation sits at the centre of the cube and is surrounded by 12 oxygens in dodecahedral geometry and the B-cation sits at the corners of the cube. By varying the A and B cations

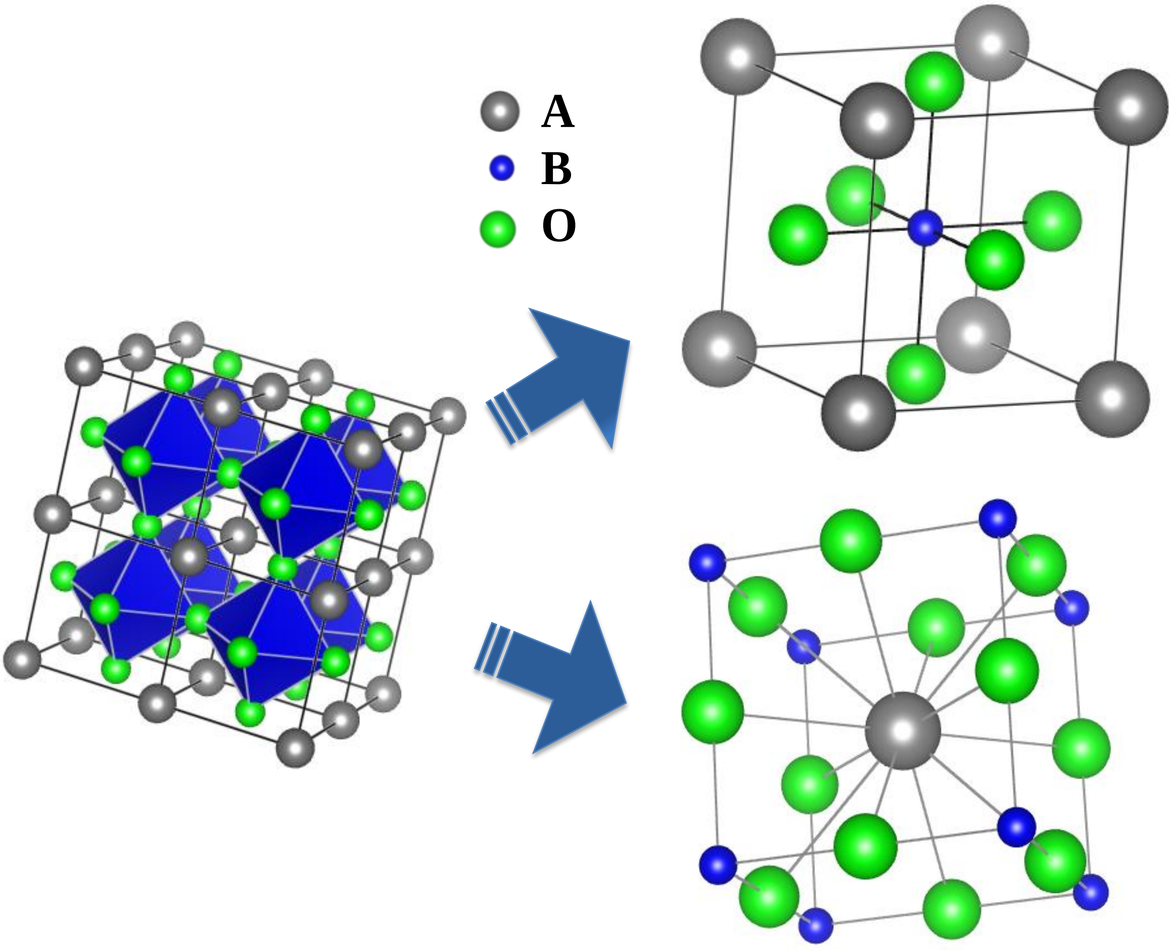

Figure 1.8: Representation of ABO_3 perovskite structure.

in ABO_3, a large number of different perovskites (almost 96) materials can be formed. The wide interest in these oxides is based on the variety of properties that can be realized in these systems. Depending on the combination of cations on the A and B sites, the materials may be conducting (even superconducting) or insulating, may show ferroelectricity or ferromagnetism, or may exhibit non-linear optical behaviour (Fig. 1.9 gives a collage of properties). In addition, substituting ions with different valences on the A site will result in different valences for the ion on the B site. If this B site ion carries some functionality, such as a magnetic moment, this may lead to competing interactions, which in turn alters the physical ground state of the material.

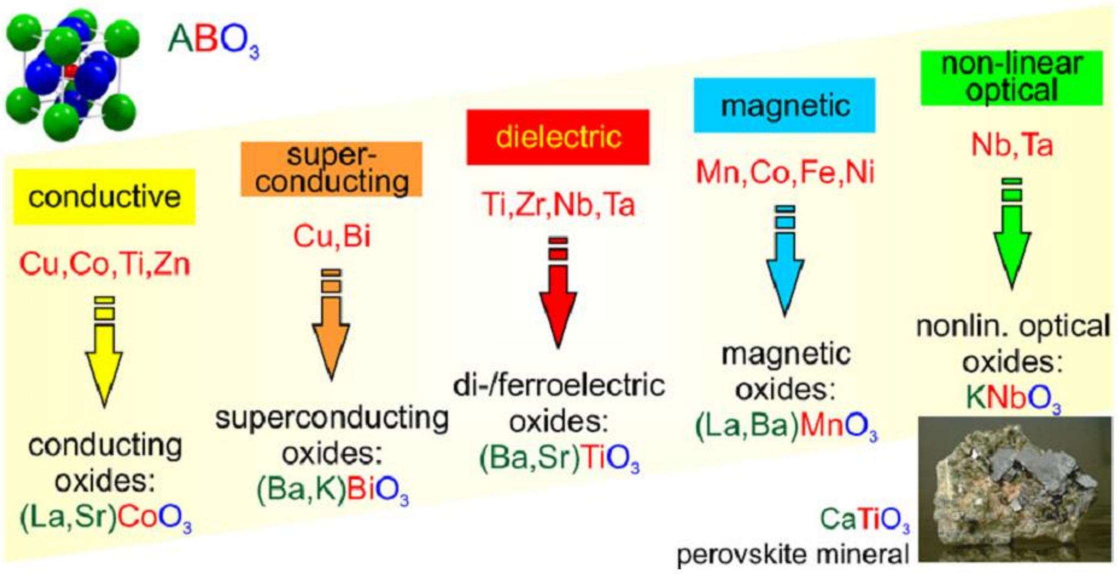

Figure 1.9: Functional perovskites oxides: Depending on the type of A and B cation different physical properties are realized. (Picture is adopted from Ref.1).

Even though, the perovskites family crystal structures have been studied extensively for long time, their basic physical properties are still unfolding surprising phenomenon. For example, high temperature superconductivity in $YBa_2Cu_3O_7$ [29] and colossal magnetoresistance in (La, Sr)MnO_3[30,31] are the most extensively studied. In some of the double perovskites, ferromagnetism lasts even at very high temperatures (up to 750K) with large spin-polarization values which have been reported.[32] These properties have been anticipated to be applied in spintronics to improve the existing schemes for magnetic random access memory (MRAM).[33]

1.4.2 Distortion in perovskite structure:

.

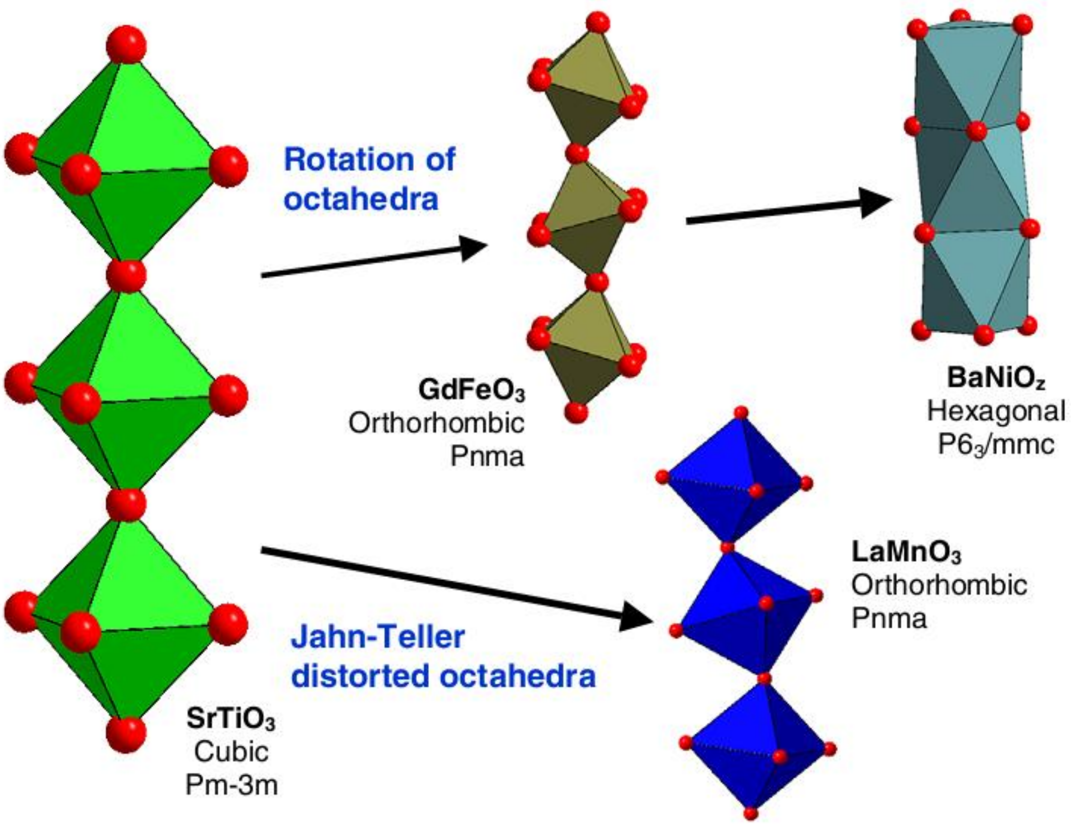

Figure 1.10: Different crystal symmetries of perovskites due to the octahedral tilting. (Picture reproduced from Ref.7).

Distortion in the perovskites structure is another important aspect which strongly influences the physical properties of the system. In magnetic materials, it directly affects the exchange interactions between the neighbouring magnetic ions. Thus, by controlling the degree of lattice distortion, one can control various physical properties of the system or can design new materials with novel properties for technological applications.

Distortions can be induced through various sources like size mismatch of A and B cation, oxygen vacancy or may be electronic origin (as in Jahn-Teller distortion). An ideal cubic perovskites exists in cubic symmetry with space group *Fm-3m*. The geometric tolerance factor (t) which is the ratio of A-O and B-O is given by $t = \frac{d_{A-O}}{\sqrt{2}d_{B-O}}$, where the value of t is unity for ideal cubic perovskite. The size mismatch of A and B cation

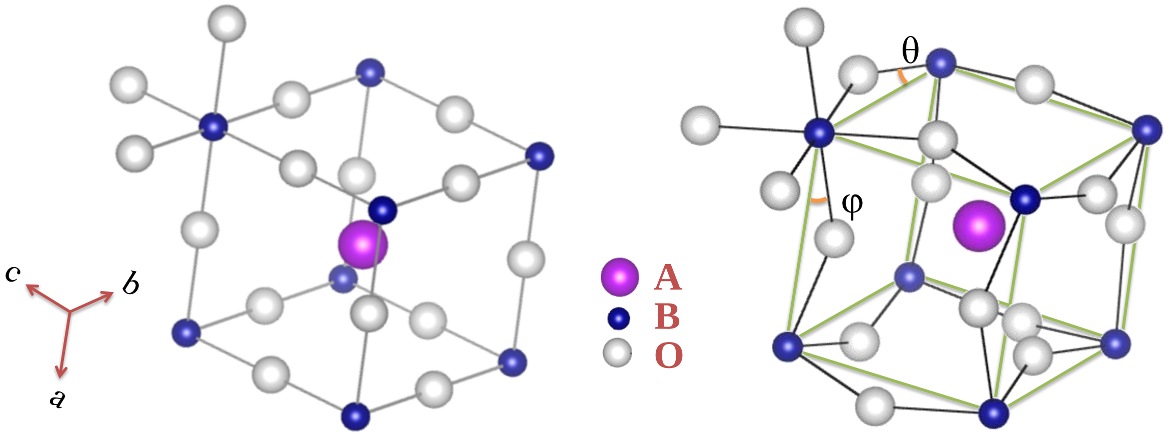

Cubic (*Fm-3m*)

Orthorhombic (*Pbnm*)

Figure 1.11: Comparison of orthorhombic perovskite to that of cubic. ‘θ’ and ‘φ’ are octahedral tilts with respect to [010] and [101] directions.

destroys the equilibrium between (A-O) and (B-O) bond lengths which leads to the lowering of tolerance factor and distortion in perovskites lattice (see Fig. 1.10). When $t < 1$, it causes a compressive stress on B-O bonds and tensile stress on A-O bonds. These internal stresses are relieved by a cooperative rotation of the BO_6 octahedra and a corresponding shift of the A-cation position. These octahedral rotations lower the crystal symmetry from the ideal cubic (*Fm-3m*). One of the most commonly observed symmetries where in the perovskites get stabilized are the tetragonal (*I4/m*), monoclininc ($P2_1/c$), orthorhombic (*Pnma*), Rhombohedral (*R-3c*) and hexagonal ($P6_3cm$).[34] A schematic diagram of various crystal structures in perovskites is shown in Fig. 1.10.

Among all these perovskite structures orthorhombic (*Pnma*) is widely studied and is relevant to the results discussed in this thesis. There are two distortions which explain the orthorhombic (*Pnma*) symmetry of the compounds compared to their cubic counterpart (*Fm-3m*): 1) BO_6 octahedral rotation (tilt) with respect to [010] and [101] directions and 2) A-cation displacement (see Fig. 1.11). The former distortions can be described by the tilting system $a^-a^-b^+$ in Glazer notation. [35] These rotations not only leads to the orthorhombic lattice parameters $b>a>c/\sqrt{2}$ but also a reduction in the B-O-B bond angle (inter octahedral angle) from 180^0. Also, distortion at octahedral site causes the M-O bond lengths to differ within the octahedra. These distortions increase or decrease with the size of A and B cations. The most widely studied orthorhombic perovskites are RMO_3 (R=rare-earth, M=transition metal). In these systems, octahedral tilts change continuously with the change in the size of the Rare-earth (R).[36]

Apart from the above mentioned perovskites distortions due to cation size mismatch, oxygen vacancies can also influence the perovskites structure. For example, in $SrFeO_x$, x can vary from 2.5 to 3 by changing the valency of 'Fe' through heating the sample in either oxidizing or reducing environment. In some perovskites, the electronic configuration of B-cation can lead to the distortion of the structure. In Jahn-Teller active B-ions (i.e Mn^{3+}, Cu^{2+}, Cr^{2+} etc.) elongation/contraction of the octahedral bonds occur due to the repulsion between 3d orbitals of B-ions and oxygen p-orbitals and it depends on the distribution of electrons in t_{2g} and e_g levels of the B-cation. This has serious implications in the magnetic properties of transition metal compounds.[37]

In this thesis, undoped rare-earth based perovskites RMO_3 (R = rare-earth, M= Mn, Co, Cr) have been studied. The main aim of the thesis is to study the structural distortions and their effect on the physical properties of these materials as a function of temperature and pressure. We have used mainly Raman scattering, since lattice vibrations (phonons) are very sensitive to external parameters like temperature, pressure, electric and magnetic fields. Thus, Raman scattering is a very sensitive tool for identifying structure, structural distortions and also identifying interactions like spin-phonon coupling etc. We have also used synchrotron powder x-ray diffraction for quantification of these distortions in some of these materials.

1.5 Bibliography:

1. M. Cardona, Light scattering in solids I: Introductory concepts, Topics in Applied Physics, Vol 8, *Springer-Verlag Berlin Heidelberg New York* (1982).
2. A. S. Barker and R. Loudon, *Reviews of Modern Physics* 44, 18 (1972).
3. R. Loudon, *Adv. Phys.* 50, 813 (2001).
4. M. Balkanski, R. F. Wallis, and E. Haro, *Phys. Rev. B* 28, 1928 (1983).
5. D. W. Feldman, J. Parker, W. J. Choyke, and L. Patrick, *Phys. Rev.*, 170, 698 (1968).
6. D. W. Feldman, J. H. Parker, W. J. Choyke, and L. Patrick, *Phys. Rev.*, 173, 787 (1968).

7. F. A. Cotton, Chemical applications of group theory, *John Wiley & sons, Inc*. (1999)
8. J. Bardeen, *Science*, 181, 1209 (1973).
9. R. K. Ferry, semiconductors: Bonds and bands, *IOP publishing, Bristol* (2003).
10. Jhang An-Min, Zhang Qing-Ming, *Chinese Phys.* B 22, 087103 (2013).
11. N. W. Ashcroft, N. D. Mermin, solid state physics, *Cengage learning (Indian edition)* (1976).
12. M. G. Cottam, D. J. Lockwood, light scattering in magnetic solids, *John Wiley & Sons* (1986).
13. W. Baltensperger and J. S. Helman, *Helv. Phys. Acta* 41, 668 (1968).
14. D. J. Lockwood and M. G. Cottam, *J. Appl. Phys.* 64, 5876 (1988).
15. Granado E., Garcia A., Sanjurjo J. A., Rettori C., Torriani I., Prado F., Sanchez R. D., Caneiro A. and Oseroff S. B., *Phys. Rev. B*, 60, 11879 (1999).
16. N. Suzuki and H. Kamimura, *J. Phys. Soc. Jpn*., 35**,** 985 (1973).
17. T. Moria, *J. Phys. Soc. Jpn*., 23, 490 (1967).
18. P. F. McMillan, *Nature Mater.*, 1, 19 (2002).
19. G. Damazeau, *Chem. scripta*, 28, 21 (1987).
20. Z. Hiroi and M. Takano, *Physica C: super conductivity and its applications* 29, 235 (1994).
21. S. Naka, K. Horii, Y. Takeda, and T. Hanawa, *Nature* 259, 38 (1976).
22. H. Yusa, *Diam. Relat. Mater.*, 11, 87(2002).
23. N. Dubrovinskaia, L. Dubrovinsky, F. Langenhorst, S. Jacobsen, and C. Liebske, *Diam. Relat. Mater.*, 14, 16 (2005).
24. A. jayaraman, *Rev. Mod. Phys.* 55, 65 (1963).
25. M. Blackman, *Proc. Phys. Soc.* B 70, 827 (1957).
26. C. Ulrich, E. Anastassakis,* K. Syassen, A. Debernardi, and M. Cardona, *Phys. Rev. Lett.*, 78, 1283 (1997).
27. B. A. Weinsteinand R. Zallen, in: Light Scattering in Solids IV, Eds. M. Cardona and G.Güntherodt , *Springer-Verlag, Berlin* (1984).
28. M. Opel, *J. Phys. D: Appl. Phys.*, 45, 033001 (2012).
29. J. Orenstein, and J. A. Millis, *Science* 288, 468 (2000).
30. M. B. Salamon, and M. Jaime, *Rev. Mod. Phys.* 73, 583 (2001).
31. D. Samal, C. Shivakumara, and P. S. Anil Kumar, *Phys. Rev., B* 77, 094510 (2008).

32. Krockenberger Y *et al*, *Phys. Rev. B* 75, 020404(R) (2007).

33. M. Bibes, and A. Barthemely, *IEEE Trans. Electron Dev.* 54, 1003 (2007).

34. M. Johnsson, and P. Lemmens, *J. Phys.: Condens. Mater.*, 20, 264001 (2008).

35. A. M. Glazer, *Acta Crystallogr. Sect. B*, 28, 3384 (1972).

36. J.-S. Zhou and J. B. Goodenough, *Phys. Rev. B*, 77, 132104 (2008).

37. K I Kugel', D I Khomskiĭ, *Phys. Usp.* 25, 231 (1982).

Chapter 2

Experimental Techniques

This chapter provides a basic overview of the various experimental techniques used in this thesis.

2.1 Raman spectrometer:

Raman scattering is a weak phenomenon with one photon getting inelastically scattered out of 10^9 incident photons. Detecting the week signals in the presence of intense background is by no means trivial. The achievable signal-noise ratio depends both on incident intensity and on the sensitivity of the detector. In recent years, there is a remarkable progress on the source as well as on the detector side.[1] Especially, in the post discovery of laser, the use of laser, modern monochromators and charge coupled device (CCD) as detector, Raman measurements have been relatively simple. To such an extent that even a novice can run a Raman spectrometer and it is used for routine characterization. However, the cost of the modern commercial Raman spectrometer and the flexibility in using them has been a matter of concern. In our laboratory, we have fabricated and used various custom-built Raman spectrometers for doing different kinds of Raman experiments.[2,3] One such Raman spectrometer has been used for the present studies discussed in this thesis. The salient features of the spectrometer are discussed below.

2.1.1 Design and performance of the Raman microscope:

To address the issue of cost, flexibility and versatility in our design of the Raman microscope, the collection optics have been assembled from the parts of a microscope by using the modular focusing unit (LV-IM), double port (Y-IDP), sextuple nosepiece (C-N), universal epi-illuminator (LV-U EPI 2), eyepiece lens (CFI 10x) and a trinocular tube (Y-TF2) all from NIKON, Japan. This collection optics can be mounted to the optical table using an L-shaped metal holder fabricated in-house. A simplified schematic of the design of the micro-Raman spectrometer using this microscope is shown in Fig. 2.1

In this set up, a linearly polarized, 532 nm line of a frequency doubled Nd-YAG solid state diode pumped continuous wave laser (model GDLM-5015L, Photop Suwtech Inc., China) is used as the excitation source. The output power of the laser is ~ 30 mW. Though the laser line is monochromatic it can contain plasma lines which have been filtered out by passing through laser plasma-line filters (PF) (LL01-633-12.5, Semrock). To avoid the light induced alteration of chemical or structural properties of certain materials, one has to cut down the power density of the laser light on the sample. To do that, one of several selectable neutral density filters (NDF) can be used. These filters can be moved in and out of the beam path depending on the intensity requirements. The light

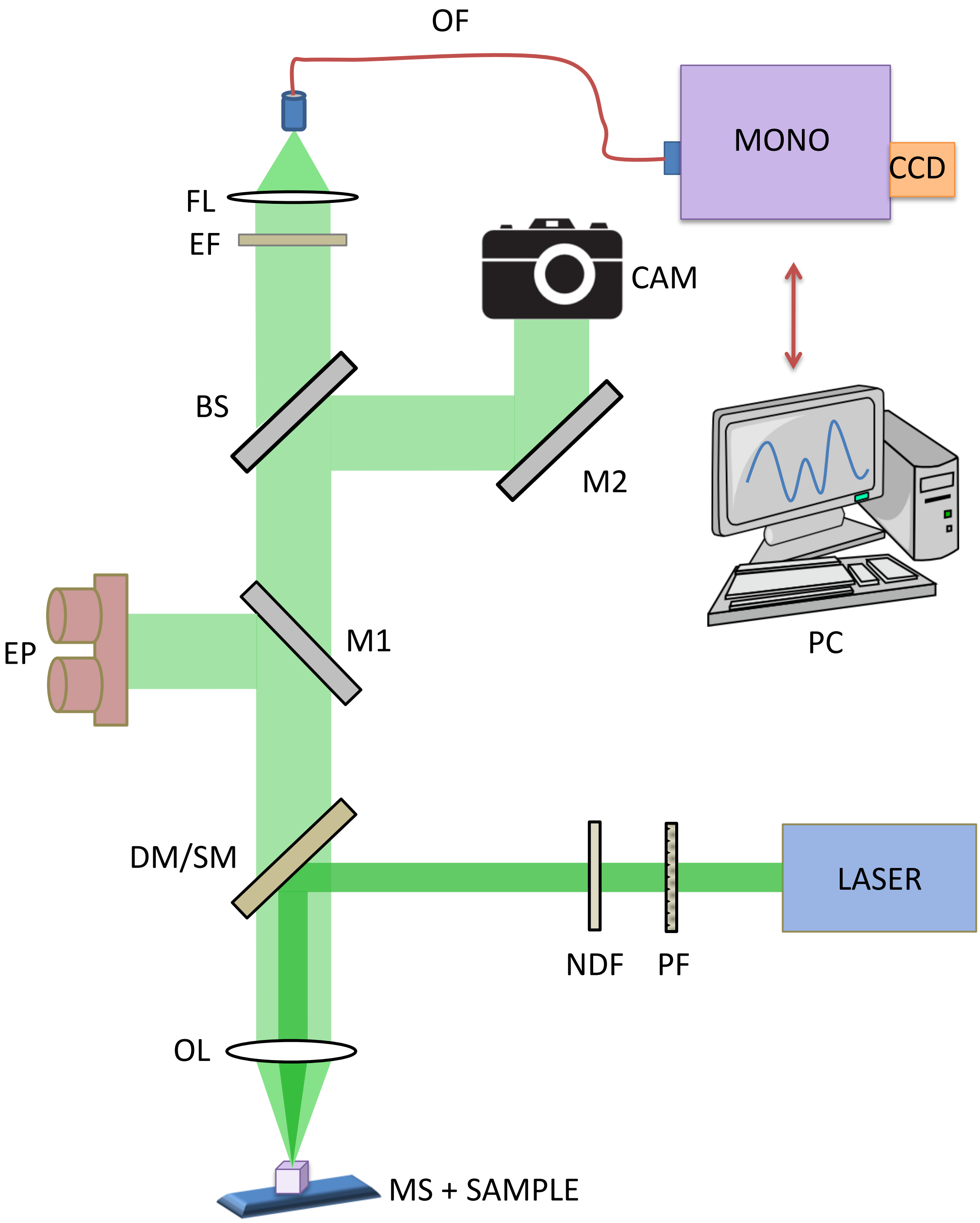

Figure 2.1: Schematic of the micro- Raman spectrometer: MS- Micro stage; OL- Objective lens, DM – Dichroic mirror, SM- special mirror, NDF - Neutral density filter, PF – Plasma filter, M1– Movable mirror, EP – Eyepiece, BS – Movable beam splitter, M2 – Mirror, CAM – Camera, EF, Edge filter, FL- Focusing lens, OF- Optical fibre, MONO – Monochromator, CCD - Charge coupled device, PC – personal computer.

falls on to a dichroic mirror (DM)/special mirror(SM) at an angle of 45^o to the surface of the mirror. Here DM or SM are placed in the slots of a dichroic mirror cube holder. The SM is designed by us and fabricated by Acexon technologies, Singapore. This SM has an Ag coating of 2-3 mm diameter at the centre of a 25 x 35 (± 0.2) mm fused silica substrate of 1.1 mm thickness. This reflected light beam is then directed onto the sample via an infinity corrected microscope objective lens (OL). The typical objective used for most of the experiments was infinity corrected 50X magnification objectives with numerical aperture (NA) and working distance (WD) of 0.45 and 17 mm, respectively. Using the revolving nosepiece which can host 6 objective lenses, one can choose the required objective for the experimental requirement (depth of focus, working distance, scattering efficiency). For instance, a long WD objective (NIKON L Plan 20X, 0.33 NA, WD 24 mm) has been used while doing high pressure Raman experiments using some of the high pressure cells.

The sample and laser spot can be viewed through the eye piece by bringing the movable mirror (M1) into the light path. A camera (CAM) can be used to capture the pictures by engaging the movable beam splitter (BS). Mirror M2 directs the beam to the camera. One can also fix the camera to the eye piece to capture the pictures. Since the BS splits the beam in 55:45 ratios, it is possible to record a spectrum as well as take a picture simultaneously. This option will be very useful while aligning the laser light. The reflected and Rayleigh elastically scattered light from the sample together with the inelastically scattered Raman signals are collected by the objective lens and directed onto a edge filter (EF) (LP03-532RS-25, Semrock) which rejects most of the Rayleigh light. The collected light is then focused onto the optical fiber (OF) (200 μm multimode single core optical fiber) with band pass of 400-1000 nm) using an objective lens (NIKON L Plan 20X, 0.33 NA, WD 24 mm), as shown in Fig. 2.1. The other end of the fiber is f-number matched to the entrance mirror and slit combination of the monochromator (MONO) of focal length 550 mm (Jobin-Yovn, Triax 550, Instruments SA, Inc., NJ, USA) attached with a liquid nitrogen cooled CCD (spectrum one) detector.

The monochromator includes gratings: holographic 1800 grooves/mm, blazed reflection type 1200 grooves/mm (500 nm blaze) and 900 grooves/mm (450 nm blaze). This allows flexibility in the choice of the gratings for optimum resolution and desired spectral range. The on-axis triple granting turret, allows the TRIAX to maintain on-axis grating rotation during scanning, keeping a constant f-number and image quality. The light was focused on to the monochromator through a slit of variable width and dispersed by the motorized diffraction grating onto the CCD via a shutter. The CCD needs to be cooled using liquid nitrogen to reduce the dark counts and to improve the signal-noise ratio. The CCD consists of rectangular two dimensional array (1024 x 128) pixels. A personal computer running the Labspec software programme controls the data acquisition aspects of the spectrometer.

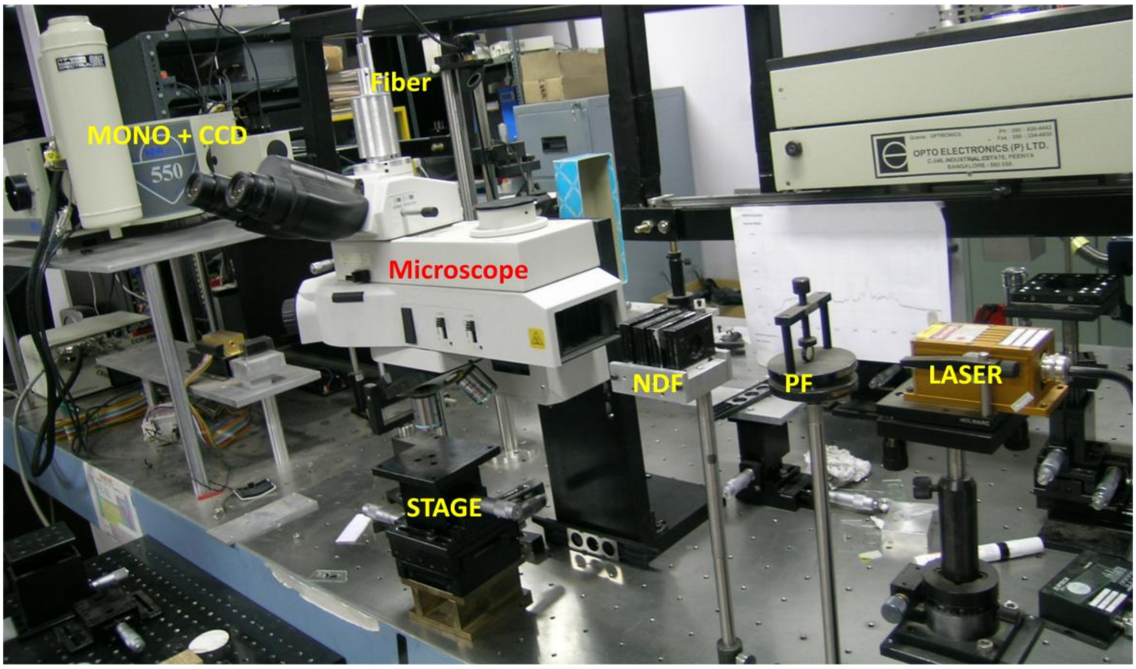

Figure 2.2: Photograph of the Fabricated Raman spectrometer.

Using the software the user chooses the desired grating and can also set the slit width, spectral range for the spectrum (determined by the angle of the diffraction grating), the exposure time of the CCD (controlled by the shutter) and the pixels used on the CCD for data collection. The user can also perform tasks like peak fitting, smoothening the spectra and background subtraction etc. using the software. In this thesis, we have used the holographic grating with 1800 grooves/mm and the input slit of 200 μm. This provides us a resolution of ~ 2 cm^{-1}.

As mentioned in the beginning, this particular microscope doesn’t include any sample stage. So the area under the objective lens is absolutely free for use of different types of experimental setup. Micrometer stages (MS) are used to place samples under the microscope and focus the light onto the sample. These stages provide us the flexibility to place temperature controllers and diamond anvil cells (DAC) on it to perform Raman measurements at different thermodynamic conditions. Fig. 2.2 shows the picture of the actual micro-Raman set up used for the present thesis work.

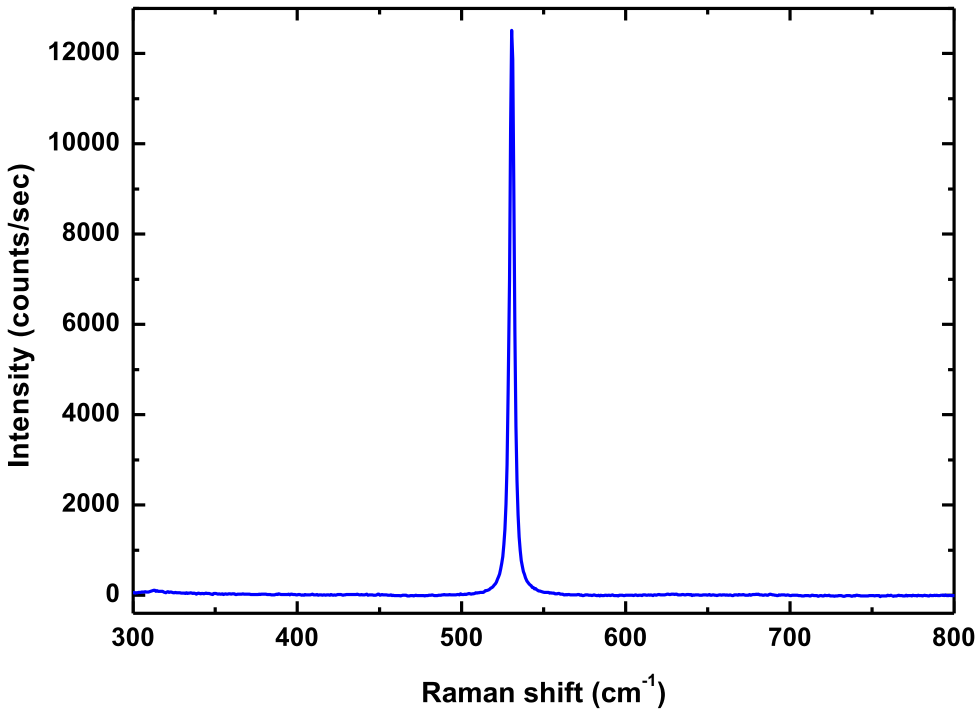

Figure 2.3: Raman spectra of silicon (100).

Fig. 2.3 shows the room temperature first-order Raman spectra[4] of crystalline silicon at ~ 521 cm^{-1} recorded using the fabricated Raman microscope. The corresponding excitation energy (2.33 eV) used in our Raman measurements is always greater than the band-gap energy of silicon (1.1 eV) so the laser light is strongly absorbed in the top layer of a silicon wafer. The spectra was collected using a 50X (NA = 0.80) objective lens. The input slit width was 200 μm and the holographic grating of 1800 grooves/mm was used. The laser power at the sample was 12 mW. As it can be seen, a very high throughput (~12,000 counts/second) is achieved with a scan time of 1 min. We use this silicon signal as a reference for aligning the spectrometer optics whenever required. The same silicon wafer will always be used for the purpose of quick calibration check. We also use emission lines[5] from Neon calibration lamp (Oriel instruments, Newport co.) recorded by CCD for the exact spectral calibration.

This spectrometer has some disadvantages. The use of edge filters (EF) does not permit the recording of the anti-stokes part of the Raman spectrum. Furthermore, Rayleigh cut off frequency in these edge filters is large (>100 cm^{-1}). So observing very low frequency modes is sometimes a problem. This problem can be surmounted by using a notch filter. The use of dichroic mirror gives better throughput, but larger Rayleigh background at very low Raman shifts.

2.2 High pressure techniques:

External pressure is a thermodynamic parameter which can be applied onto the materials for tuning their properties. This has been discussed in Chapter 1. Here, we discuss the pressure generation and related techniques. The principle of pressure generation is based on the basic definition of pressure:

$$P = \frac{F}{A} \tag{2.1}$$

where P is the pressure generated and F is the force exerted on the area A. This relation implies large pressures can be achieved by applies force on small area. This has been used in generating Mbar pressures in an opposing anvil device where the affected area between the flat surfaces of the anvils is of the order of a few tens of microns. Increasing the applied force may exceed the compressive strength of the anvils to withstand the stress and would lead to failure of the anvils. Therefore, to achieve hydrostatic pressure of higher magnitude, anvils with smaller facets are required. This is the secret for the success of the diamond anvil cell. [6-8]

2.2.1 Diamond anvil cell:

Diamond anvil cell (DAC) is the most widely known high pressure research equipment among all known anvil materials used so far. This is because diamond is recognised as the hardest and least compressible material has the important property of being transparent to the most of the electromagnetic radiations, including γ-ray, X-ray, visible light and most of the infrared and ultra-violet region. These radiations are used as a probe for measuring wide range of properties of the materials *in-situ* at high pressures. The DAC thus provided the first opportunity for high-pressure researchers to observe visually the effects of pressure, and it allowed convenient access for many kinds of experimental techniques, notably x-ray, gamma-ray (Mossbauer spectroscopy), Raman spectroscopy and other optical spectroscopies.[9,10] Fig.2.4 shows a schematic diagram of a diamond anvil cell mechanism. As shown here, sample is placed between polished culets of two diamonds inside a sample chamber provided by a metal gasket. In this configuration, extremely large pressures can be achieved by applying a very little force on the culets. The different designs of DAC arise from the differences in the mechanisms of generating force and for the anvil alignment and can be classified into five major types of DACs.[11-15]

1. Mao-Bell cell
2. Bassett cell
3. NBS cell
4. Merrill-Bassett cell
5. Syassen-Holzapfel cell or Membrane cell

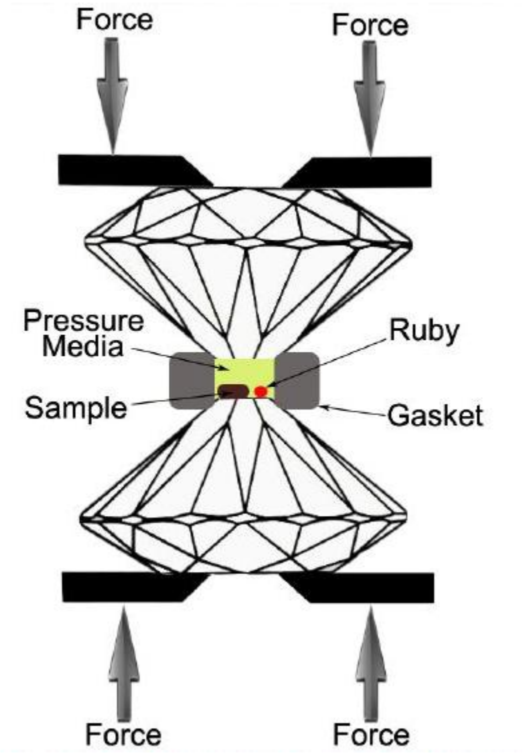

Figure 2.4: Schematic of diamond anvil mechanism.

In the present work, we have used a Membrane diamond anvil cell (MDAC) from BETSA, France for our pressure dependent Raman and x-ray diffraction experiments.

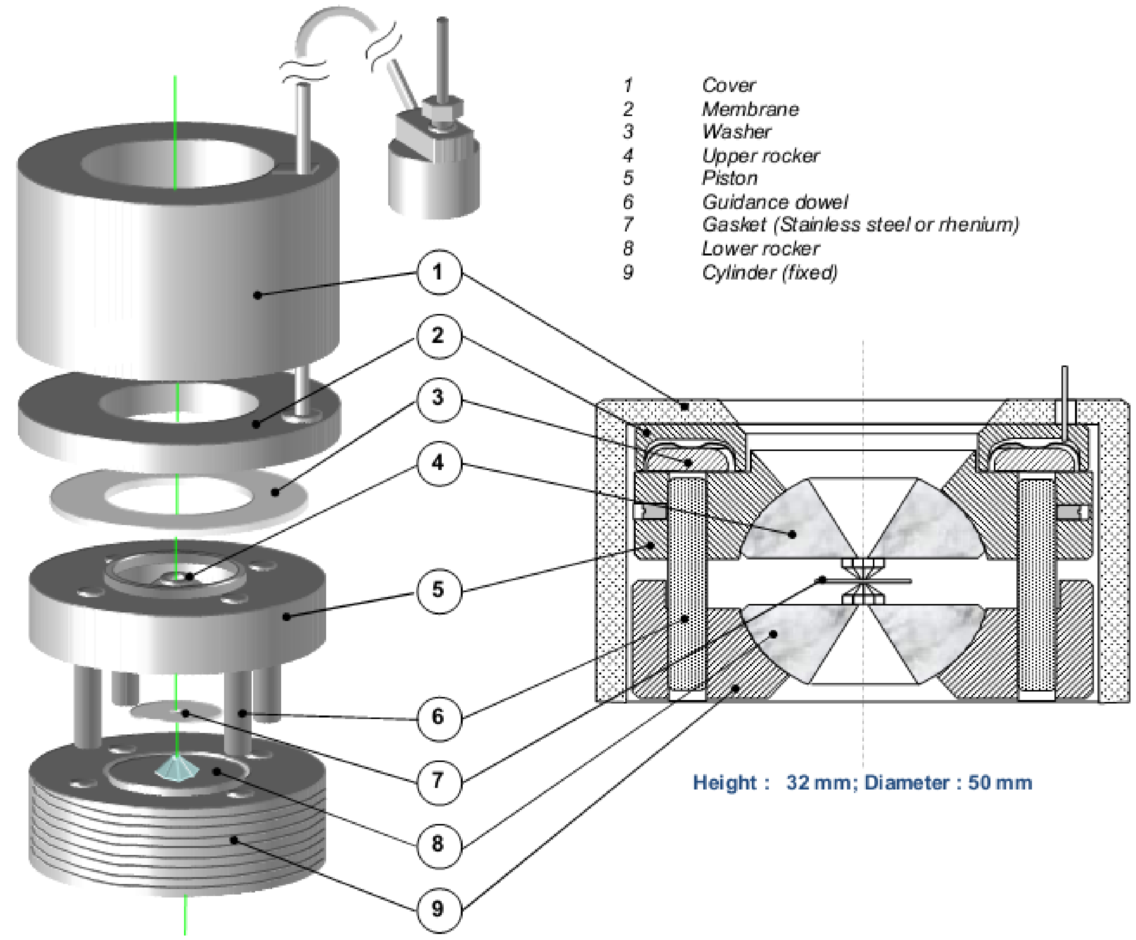

Figure 2.5: Schematic diagram of membrane diamond anvil cell (MDAC). Picture adopted from the website *www.betsa.fr*.

2.2.2 Membrane diamond anvil cell (MDAC):

Fig.2.5 shows the schematic of the MDAC used in this thesis. The main components are, a) stainless steel gas membrane (diaphragm), to push the piston against the cylinder when gas is filled in it, b) diamonds glued to the upper and lower rockers (backing plates), c) guidance dowel to hold and align the piston inside the cylinder. In some designs the guidance dowel is replaced with a guide screw and notch. The present MDAC used for our studies has similar guide screw-notch arrangement which facilitates to lock piston over cylinder in only one way. The actual MDAC used for the present thesis is shown in Fig. 2.6a. This cell can easily be fit under our Raman microscope for the pressure dependent Raman experiments as shown in Fig 2.6b. A pneumatic drive system (PDS) which consists of a helium gas cylinder (up to 200 bar capacity) is connected to the MDAC to control the pressure (see Fig. 2.6c). When the gas membrane is filled with the helium gas, it bulges and pushes the piston against the cylinder and thereby generates the pressure inside the cell.

Figure 2.6: Photograph of the a) MDAC b) MDAC under Raman microscope c) MDAC connected to pneumatic drive system (PDS).

The main factors that determine the maximum pressure generated in a high pressure cell depend on the type of anvils, the hardness of the material which the cell body and backing plates are made from, gasket material to confine the sample, alignment of the anvils and pressure transmitting medium. Each of these factors is discussed below.

2.2.3 Diamond:

The first and foremost step for fabricating an anvil cell is selecting the appropriate diamond. The four important things to be noted are cut, color, clarity and carat (generally known as 4Cs). The diamonds used in the DAC are from brilliantly-cut gem quality diamonds. The diamonds are broadly classified into two types, type I diamonds contains nitrogen impurities and type II diamonds are relatively pure and rare in occurrence. Depending on the type of impurity these are further classified in Type Ia, Type Ib, Type IIa and Type IIb. Depending on the state of the nitrogen impurity whether it appears as a pair or singlet decides the diamond Type Ia or Type Ib respectively. Type IIa is purest diamond and Type IIb is semiconducting due to boron impurities. For Raman and photoluminescence experiments, Type IIa is ideal. But Type Ia diamonds with low luminescence are widely used due to their easy availability and low cost. The normal size of the diamonds used in the DAC is 1/8 to 1/2 carat (1 carat = 200 mg). In general, diamonds with larger culet sizes are limited for lower pressure usage. An approximate formula to calculate the maximum attainable pressure (P_{max}) using a diamond anvil with culet diameter d is given by[15]

$$P_{max} = \frac{12.5}{(d\ (mm))^2} \tag{2.2}$$

The diameter of the table of the diamonds in high pressure experiments determines the stress applied to the backing plates and thus the maximum attainable pressure. The culet size should be much smaller than the table of the diamond to attain very high pressures.

2.2.4 Backing plates:

After the diamonds, the material supporting the diamond (backing plate) is the most important factor for limiting the maximum useful pressure. If the stress in the backing plates exceeds the plastic deformation, then the anvil alignment can be destroyed, resulting in the breakage of the diamonds. In general, tungsten carbide and boron materials are usually used for mounting the diamond for the high pressure experiments. Tapered holes are created on the flat metallic surfaces of the backing plates. The culet of the diamond is centred on the tapered hole of the backing plate. These holes are for the access of the optical and x-ray radiation behind the diamonds which are also the deciding factor for the maximum pressure limit. The hole diameter should always be greater than the culet size for the viewing of the culet while aligning the anvils. They should not have a diameter greater than about one-third of the diameter of the diamond table. These holes are usually cut with a cone angle. Larger the cone angles,[14] however, weakens the backing plates to withstand higher stresses.

2.2.5 Diamond alignment:

The most important and critical part of the DAC experiments is aligning the diamond culets. The diamond culets must be aligned laterally as well as parallel (culet surface) to avoid the gasket deformation and breakage of the anvils during loading. Different DACs will have different alignment mechanisms depending on the design of the cell. For aligning the anvils in our present MDAC, we use the following steps. Initially, the piston is inserted into the cylinder carefully and seeing through the microscope, the culets of both the diamonds are matched along X and Y directions by adjusting the three set screws located on the piston wall. The parallelism of the culet surfaces is attained by adjusting the screws on top of the cylinder. For this purpose, light fringe technique (Newton’s ring) is used. When the diamonds not perfectly parallel, we observe the interference fringe pattern in the culet area, when piston is inserted into the cylinder. By rotating the screws on the cylinder one can reduce the number of fringes inside the culet area and perfect alignment is attained in the zero-fringe condition. After the alignment, all the screws should be in the fully tightened condition. It should be noted that alignment of the anvils has to be checked after every pressure cycle.

2.2.6 Gasket preparation:

The introduction of the gasket between the diamonds has two important reasons: 1) it supports the diamond culets (diamonds cannot handle stresses in all directions) and 2) to create a sample chamber where in hydrostatic medium can be filled along with the sample for the hydrostatic pressure conditions. The gasket is pre-indented, prior to use, inside the DAC. Indentation work hardens the gasket material between the diamonds and is useful for achieving high pressures. Also, the gasket material which flows around the diamond during indentation holds the diamonds and protects the diamond edges from breakages. Usually, the gasket material is made of a hard material like hardened stainless steel (T301), inconel, tungsten, rhenium, and copper-beryllium alloy. After pre-indentation, hole will be drilled at the centre of the indented area. The success of reaching high pressures depends on centring of the hole. The size of the hole should be order of ~ 1/3 rd of culet size.[16] There is an equal and opposite force acting inwards between gasket material and the surface of the culet. This is the indication of the stability of the gasket. If the thickness of the gasket is sufficiently small, the destabilizing outward force is smaller than inward stabilizing force, as a result shrinkage of the gasket hole happens. On the other hand, if the thickness of the gasket is too large, consequently, the outward destabilizing force will be larger than the inward stabilizing force, and hence causes the elongation of the gasket hole.[16,17] It is very crucial to watch the gasket hole each time the pressure is changed. If there is an asymmetric elongation of the gasket, the experiment should be terminated. We have used stainless steel gaskets (T301) of initial thickness 250 μm which are work hardened (pre-indented) to a thickness of 60 μm. We have drilled 140 μm holes inside the gaskets using micro drill equipment, with the aid of micro solid carbide drill bit.

2.2.7 Pressure medium:

To achieve hydrostatic pressure[18] conditions on the sample inside DAC, sample has to be immersed in a medium. Various fluids have been reported to be good hydrostatic media.[18-20] silicone oil ~ 2 GPa, isopropyl alcohol ~ 4 GPa, H_2O ~ 5 GPa, 1:1 pentane to iso-pentane ~ 7 GPa, methanol ~ 8 GPa, 4: 1 methanol to ethanol ~ 10 GPa, 16:3:1 methanol to ethanol to water ~ 14.5 GPa are some of the liquid media which can be used. These liquids solidify above those indicated pressures and become quasi-hydrostatic. There are some solid media like sodium chloride ~ 7 GPa, silver iodide ~ 7 GPa which can also be used. Noble gases like He ~ 70 GPa and Ne ~ 16 GPa can be used for hydro static conditions for very high pressures, above the indicated pressure these noble gases become liquid and still maintain hydrostaticity. For the present experiments, we have used 4:1 ethanol to methanol and silicone oil as pressure transmitting media.

2.2.8 Pressure measurement:

In the static high pressure work using diamond anvils, ruby fluorescence method is widely used pressure calibration technique.[21] Ruby (5% Cr^{3+}- doped Al_2O_3) is well suited for pressure sensor in high pressure work because of its strong, sharp R-emission lines. Fluorescence from ruby crystal is known to exhibit pressure dependence.[22] The R-line luminescence spectrum consists of two sharp lines (R_1, R_2) which originate due to the crystal field splitting of d-orbitals of Cr^{3+} ion surrounded by the oxygen atoms (in the Aluminium site) in an octahedral geometry. These lines occur at ~ 694.2 nm (R1) and

692.7 nm (R2). The wavelength shift of R1 line is mainly used for pressure calibration under static high pressure.[23] Under hydrostatic conditions the separation between R1 and R2 remains unchanged. This can be expressed as:[24]

$$P(Gpa) = \frac{1904}{B}\left[\left(1+\frac{\Delta\lambda}{\lambda_0}\right)^B - 1\right] \qquad (2.3)$$

where $\Delta\lambda = \lambda_P - \lambda_0$, is the difference in the wavelength at pressure P and at ambient pressure. B= 7.665 and 5 for quasi-hydrostatic and non-hydrostatic conditions respectively. In this thesis ruby fluorescence method has been used for *in-situ* pressure determination, in the case of Raman experiments. In X-ray experiments, one can use the Equation of State (EoS) of various elements like *Au*, *W*, *Re*, *Cu*, *Pt* etc. These metal powders (2 to 3 micron sizes) of these elements, especially *Au* are used for in-situ pressure measurement on synchrotron experiments.

2.3 Temperature dependent experiments:

For temperature dependent Raman scattering studies, we have used a cryostage (Linkam THMS 600, Linkam Scientific, UK) equipped with a temperature-controller (Linkam TMS 94) and liquid nitrogen pumping module (LNP 94). The temperature was controlled with an accuracy of ± 0.1 K. The external control unit (Linkam TMS 94) maintains the set temperature and can also perform ramping up and down of the temperatures at user specified rates. We have used a ramp rate of 10^{o}/min.

2.4 Synchrotron x-ray diffraction:

X-ray diffraction is a valuable technique for characterizing the structural aspects of the material. It can be performed when the samples are inside DAC using either laboratory x-ray source or synchrotron. Since in a synchrotron, x-rays with very high energy (up to 100 keV) can be produced with very high flux compared to the laboratory sources. Which means that the wavelength is much shorter than laboratory x-rays, using the famous Planck's law: $\lambda = \frac{hc}{\varepsilon}$, where λ is the wavelength of the radiation, ε is the photon energy, c is the speed of light and h is the Planck's constant. When wavelength is shorter, it allows for the same conical section a much wider 2theta range, simply due to Bragg's law. Modern synchrotron x-ray sources can provide very narrow beam-sizes resulting high spatial resolution and monochromatic radiation. In the next subsection we will see salient features of the synchrotron radiation.

2.4.1 Synchrotron radiation:

In synchrotrons, radiation is generated from charged particles travelling at relativistic velocities in applied magnetic fields which force them to travel along curved paths. In general, radiation is produced in storage rings where electrons or positrons are kept circulating at constant energy $\gamma = \varepsilon_e/mc^2$. Here the electron energy is in the units of the rest mass energy. The charged particle moving in a circular path experiences a constant acceleration and radiates continuously throughout its entire orbit.

However, the radiation from a relativistic charged particle moving in a circular orbit is compressed into tightly collimated cones of radiation with cone angle inversely proportional to γ as shown in Fig. 2.7a. This radiation consists of a range of wavelengths. In these storage rings the synchrotron radiation is produced either in the bending magnets needed to keep the electrons in a closed orbit, or in insertion devices such as undulators (Fig. 2.7b) or wigglers (Fig. 2.7 c) situated in the straight sections of the storage ring.[25] In the insertion devices, an alternating magnetic field forces the electrons to flow oscillating paths rather than moving in a straight line. In a wiggler the amplitude of the oscillations is rather large, and the radiation from different wigglers adds incoherently. Whereas, in undulator, the small-amplitude oscillations from the passage of a single electron produce a coherent addition of the radiation from each oscillation. The difference in the performance of these two devices is mainly due to the difference in the electron maximum oscillations in the horizontal plane as shown in Fig.2.7b and c. In practice, the brightness of the radiation is determined using a quantity called Brilliance which is expressed as the number of photons emitted per second per unit solid angle. It is clear that larger the quantity γ, smaller the cone angle and brighter the radiation.

In general, in storage rings, electrons are stored in bunches. For certain applications, one may choose to have a single bunch. Although the radiation from single electron is coherent, the radiation from a bunch of electrons is incoherent. To avoid this, the charged particles can be ordered spatially into smaller micro-bunches with a separation equal to the desired wavelength (for instance x-ray wavelength), then the radiation from one-micro bunch would be in phase with all other micro bunches. Based on this concept free- electron lasers have been produced which will have very high brilliance compared to conventional undulators.

(a) Bending magnet

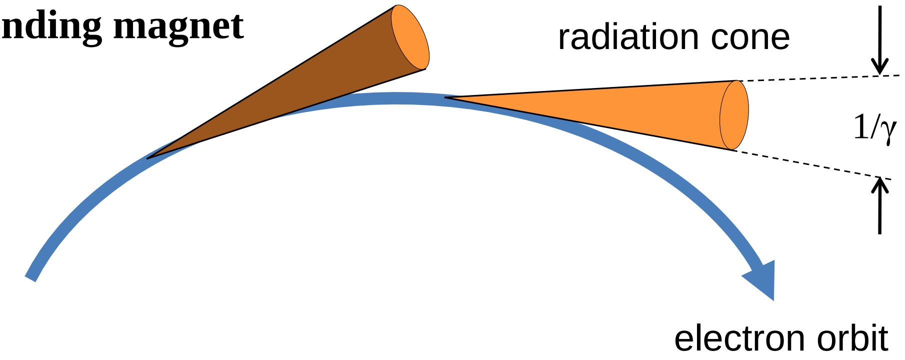

(b) Undulator

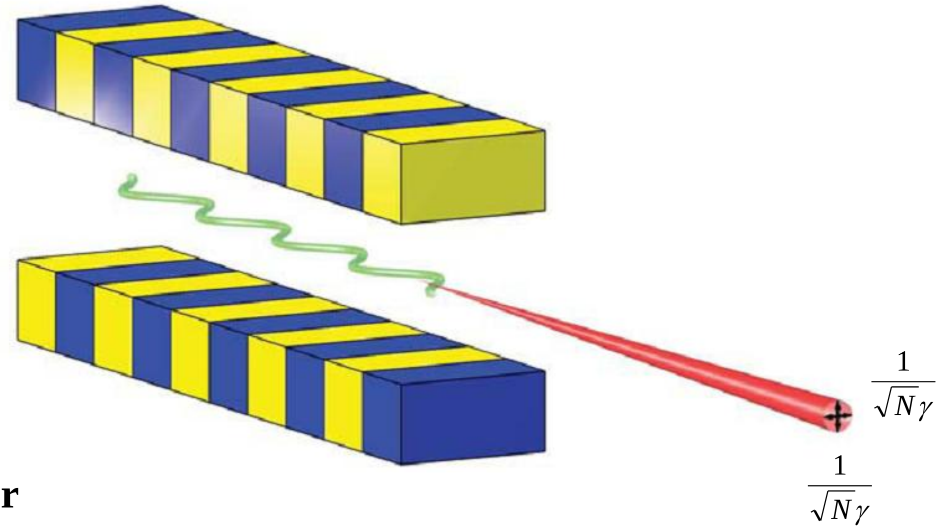

(c) Wiggler

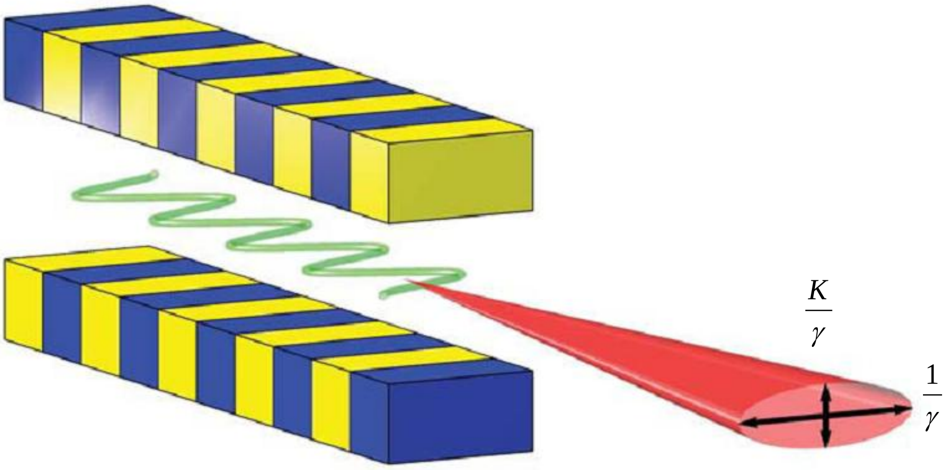

Figure 2.7: Radiation from a) electron moving in a circular path due to bending magnet b) undulator c) wiggler. Here K is around 20 and N is around 50. (schematic is adopted from Ref. 25).

2.4.2 A typical beamline:

The outline of a typical beamline is shown in Fig. 2.8a. The x-ray radiation coming from the wiggler/undulator will be focused on to the entrance slit using horizontal and vertical mirrors. These mirror surfaces can be planar, spherical, cylindrical or toroidal and are coated with different materials like gold, SiO_2, or carbon to optimize the reflection. The diverged light beam from the slit falls onto the grating which monochromatizes the radiation. For soft x-rays, holographic gratings are used, but for hard x-rays, Si(111) surface is used. Here, the lattice spacing of Si (111) plane serves the purpose of grating groove. The monochromatic x-ray beam from the gratings will be focused on the exit slit and from there the beam is focused on to the sample by a pair of mirrors. The diffracted light from the sample is detected by the photo detectors. The sample can be replaced with a DAC as shown in Fig. 2.8b for pressure dependent x-ray

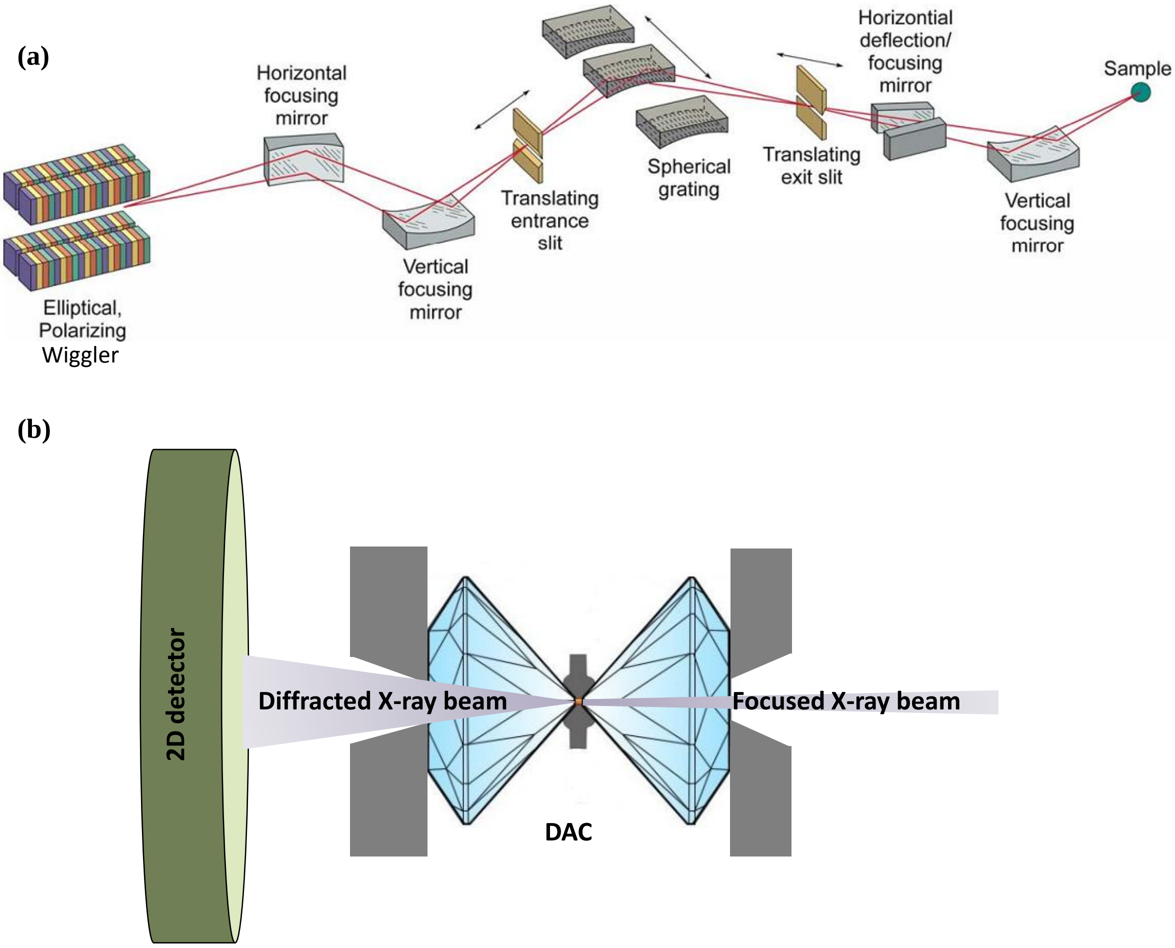

Figure 2.8: a) Schematic diagram of a typical beamline. b) Schematic diagram depicting the high pressure cell, x-ray beam and image plate detector.

diffractions experiments. An image plate (2D detector) is used for detecting the diffracted x-rays from the sample. It is mandatory, that when performing angle dispersive x-ray studies in high pressure, the sample should be ground to a very fine powder such that there is no preferred orientation in the sample. On then we see very uniform concentric circular rings.

In the results presented in Chapter 6, we have performed high pressure powder diffraction experiments at XRD1 beamline at Elettra synchrotron, Trieste. The energy of the x- rays used was 20 keV (wavelength ~ 0.7 Å) and the beam current was ~ 309 mA.

2.5 Bibliography:

1. J. Coates, *Appl. Spect. Rev.* 33, 267 (1998).
2. G. Kavitha, S. R. C. Vivek, A. Govindaraj, and C. Narayana, *Proc. Indian Acad. Sci.Chem. Sci.* 115, 689 (2003).
3. G. V. P. Kumar and C. Narayana, *Curren. Sci.* 93, 778 (2007).
4. J. H. Parker, D. W. Feldman, and M. Ashkin, *Phys. Rev.* 155, 712 (1967).
5. S. B. Kim, R. M. Hammaker, and W. G. Fateley, *Appl. Spect.* 40, 412 (1986).
6. C. E. Weir, E. R. Lippincott, A. Van Valkenburg, and E. N. Bunting, *J. Res. Natl. Bur. Stand.* 63 A, 55 (1959).
7. W. A. Bassett, *High Pres. Res.*, 29, CP5 (2009).
8. J. C. Jamieson, A. W. Lawson, and N. D. Nachtrieb, *Rev. Sci. Instrum.*, 30, 1016 (1959).
9. A. Jayaraman, *Rev. Mod. Phys.* 55, 65 (1983).
10. A. Jayaraman and S. K. Sharma, *Curren. Sci.*, 74, 308 (1998).
    W. A. Bassett, T. Takahash, and P. W. Stook, *Rev. Sci. Instrum.*, 38, 37 (1967).
11. G. Huber, K. Syassen, and W. B. Holzapfel, *Phys. Rev. B*, 15, 5123 (1977).
12. H. K. Mao and P. M. Bell, *Carnegie Inst. Washington Yearbook* 77, 904 (1975).
13. G. J. Piermarini and S. Block, *Rev. Sci. Instrum.*, 46, 973 (1975).
14. L. Merrill and W. A. Bassett, *Rev. Sci. Instrum.*,45, 290 (1974).
15. D. J. Dunstan and I. L. Spain, *J. Phys. E: Sci. Instrum.* 22, 913 (1989).
16. D. J. Dunstan, *Rev. Sci. Instrum.*, 60, 3789 (1989).
17. I. L.Spain, and D. J. Dunstan, *J. Phys. E: Sci. Instrum.*, 22, 923 (1989).
18. S. J. You, L. C. Chen, and C. Q. Jin, *Chinese Phys. Lett.*, 26, (2009).
19. J. H. Weaver, J. L. Martins, T. Komeda, Y. Chen, T. R. Ohno, G. H. Kroll, N. Troullier, R. E. Haufler, and R. E. Smalley, *Phys. Rev. Lett.* 66, 1741 (1991).

20. G. J. Piermarini, S. Block and J. D. Barrnett, *J. Appl. Phys.*, 44, 5377 (1973).
21. J. D. Barnett, S. Block, and G. J. Piermarini, *Rev. Sci. Instrum.*, 44, 1 (1973).
22. R. A. Forman, G. J. Piermarini, J. Dean Barnett, and S. Block, *Science* 176, 284 (1972).
23. K. Syassen, *High Pres. Res.*, 28, 75 (2008).
24. H. K. Mao, P. M. Bell, J. W. Shaner, and D. J. Steinberg, *J. Appl. Phys.*,49, 3276 (1978).
25. J. A. Nielsen, and D. McMorrow, Elements of modern x-ray physics, *John Wiley and Sons, UK.* (2011).

Chapter 3

Influence of Lattice Distortion on Curie Temperature and Spin-Phonon Coupling in $LaCo_{0.5}Mn_{0.5}O_3$

The author's main contribution in this chapter is to perform the Raman measurements on $LaCo_{0.5}Mn_{0.5}O_3$ *at ambient as well as at lower temperatures and analyzing the data. Mr. Viswanathan, Dr. Kaustuv Manna from Indian Institute of Sciences, Bangalore, have synthesised the samples and have performed magnetic and structural characterizations. The Neutron diffraction studies were done by Dr. Yusuf's group, BARC, Mumbai.*

3.1 Introduction:

B-site doped perovskites $AB'_{1-x}B''_xO_3$ (A and B are metal cations) have drawn considerable attention recently due to their multifunctional properties.[1-3] Especially, the rare earth based double perovskites $LaB'_{0.5}B''_{0.5}O_3$ (B', B"= Mn, Co, Ni) have been studied extensively as they exhibit a combination of ferromagnetic insulating and magneto dielectric behaviour that potentially suit spintronics applications.[4-7] $LaMn_{1-x}Co_xO_3$ is a B-site doped compound in which the structural disorder and the B-site ordering have been investigated in detail.[8-10] The parent compounds, $LaMnO_3$ and $LaCoO_3$, are orthorhombic A-type antiferromagnetic and rhombohedral diamagnetic insulators respectively. But the doping transforms the system to a ferromagnet regardless of crystal structure. For $x < 0.5$, the system stabilizes in orthorhombic and for $x > 0.6$, it stabilizes in rhombohedral. It was proposed[11-12] initially that Mn^{3+}-Mn^{4+} double exchange could be responsible for ferromagnetism, later it was attributed that to Mn^{4+}- Co^{2+} or Mn^{3+}- Co^{3+} superexchange interactions.[13] The 50% doped system $LaMn_{0.5}Co_{0.5}O_3$ (LMCO) possesses two ferromagnetic transitions ($T_c \approx 143$ & 225 K) depending on preparation conditions. The high T_c phase (HT_C) is stabilized if the sample is synthesized below 800 °C, whereas the low T_c phase (LT_C) is stabilized if the sample is synthesized above 1300 °C. Based on our finding in this chapter, the neutron diffraction studies were carried out. The neutron diffraction studies suggested that the low T_c phase, which was found to be orthorhombic phase through x-ray diffraction studies, was indeed monoclinic structure with the space group $P2_1/n$ with a long range Mn/Co ordering.[14]

Similar to B-site doped manganites, suitable A-site doping can also induce ferromagnetism in manganites. The impact of the internal pressure spanned by the A-site ion on the electronically active band formed by the overlap between *d* orbitals of B-site transition metals and *p* orbitals of oxygen, have direct control on the overlapping of orbitals, where the internal pressure is initiated by the A-site ions of different sizes.[15] Based on the earlier studies suggested by this explanation, A-site substituted $LaMnO_3$ which are ferromagnetic, showed different T_c, for different dopants having appropriate concentrations.[16] Although the reasons behind the changes in T_c for A-site doped manganites have been proposed, the factors responsible for two distinct T_c for B-site (Co) doped manganites have not been clearly understood.

Based on this facet, the first part of this chapter presents the Raman studies on polycrystalline LMCO samples (LT_C & HT_C) in the quest for finding the plausible reasons for the occurrence of two ferromagnetic phases. Raman scattering is an extremely sensitive tool used to examine lattice distortions, spin-phonon coupling etc., and has been extensively used in manganite systems to get the insight into its physical properties. By examining the room temperature Raman spectra, we can conclude that these two phases having iso-structural crystal structure have a strong correlation between the T_c and their distinct inter cationic angle ($\theta_{TM-O-TM}$) and B-site ordering. In addition, the temperature dependent Raman scattering studies on both the phases suggests that there is strong spin-phonon coupling below T_c.

The second part of this chapter will discuss on magnetic anomalies induced by the lattice distortion in single crystals of LMCO. As-grown crystals possess huge lattice strain which was released by a post-growth annealing procedure. A comparative study of the structural distortions and magnetic properties of as-grown and annealed LMCO single crystals were made with the polycrystalline counterpart. From the temperature dependence of the Raman modes, we found that the two phase behaviour is observed even in single crystals which confirms that the two magnetic ground states in LMCO is inevitable irrespective of its crystallinity or conditions of synthesis.

3.2 Experimental details:

The polycrystalline low T_c (LT_C) and high T_c (HT_C) samples were prepared by solid state reaction of La_2O_3, MnO_2 and Co_3O_4 at 1370 ^oC and at 790 ^oC respectively [17]. The oxygen stoichiometry was examined for both the samples by iodometric titration and was experimentally verified to be nearly stoichiometric within the experimental limits. For single crystal growth, feed rod of polycrystalline LT_C sample has been used in four-mirror optical floating zone image furnace under 2 bar oxygen pressure with a growth velocity of 5 mm/h. High oxygen pressure and flow rate ensure O_2 stoichiometry. XRD has been taken using Bruker D8 Advance diffractometer with Cu Kα radiation. Neutron diffraction experiments on polycrystalline samples (LT_C & HT_C) were performed at room temperature by using the five linear position sensitive detectors based neutron powder diffractometer (λ = 1.2443 A^o) at Dhruva reactor, Bhabha Atomic Research Centre, India. The Raman scattering measurements were performed in back scattering geometry using a custom-built Raman spectrometer (as described in the experimental section in chapter 2) with a laser excitation of 532 nm using a frequency-doubled Nd-YAG laser. A laser power of 5 mW was used at the sample. Temperature dependent Raman measurements were carried out from 80 K to 300 ± 1 K using Linkam stage.

3.3 Results and discussion:

3.3.1 Polycrystalline LMCO:

The crystallographic details of the powder samples (LT_C & HT_C) obtained from neutron diffraction are listed in Table 3.1. Both the samples were found to be in single phase and indexed to monoclinic with the space group identified as $P2_1/n$. The AC susceptibility measurements revealed the T_c for LT_C and HT_C are 138K and 243K respectively. The room temperature unpolarized Raman spectra of both the samples are shown in Fig.3.1a. From the lattice dynamical calculations (LDC), LMCO with monoclinic and rhombohedral structures were predicted to have 24 and 8 Raman modes respectively.[18] It has been shown that LMCO has similar TM–O octahedral vibrations in comparison to $LaMnO_3$ (*Pbnm*) and octahedral fluoride complexes and their predominant peaks at 490 and 645 cm^{-1} were assigned to Antistretching (ω_A) and Stretching modes (ω_S) respectively[19]as depicted in Fig. 3.1b. LDC confirms that the peak at 697 cm^{-1} is assigned to stretching mode ("breathing"), while the ones at 490 cm^{-1} is of a mixed type

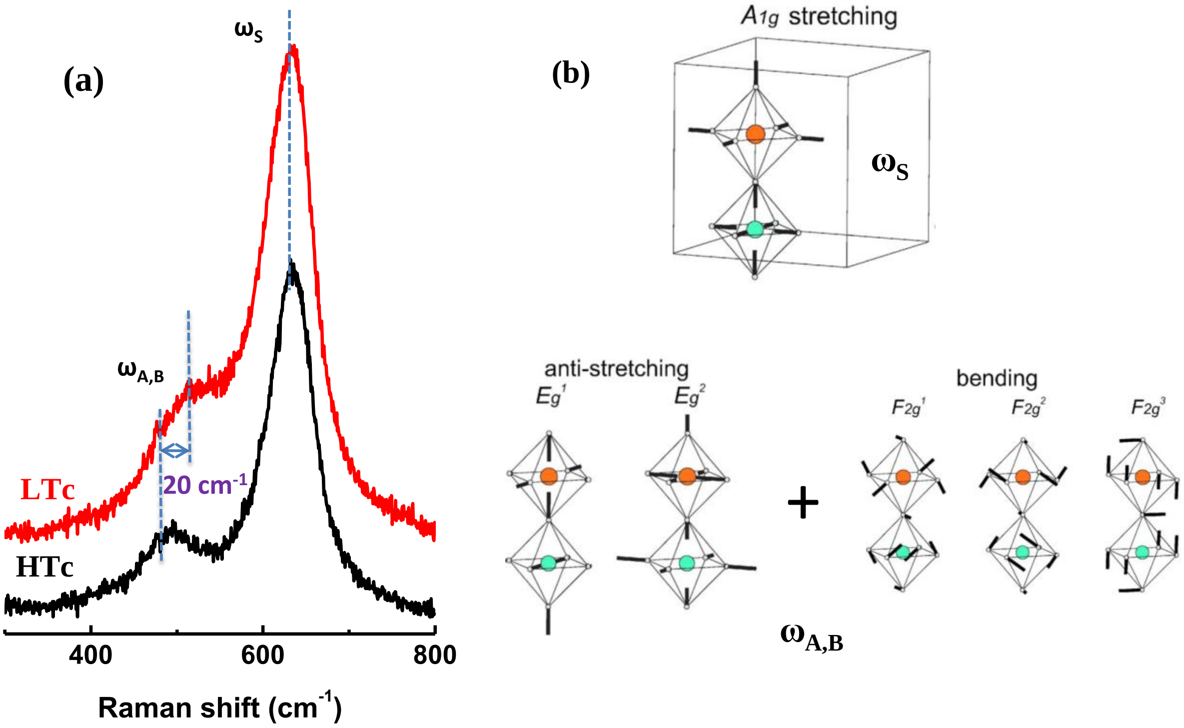

Figure 3.1: a) Raman spectra of LTc and HTc phases. b) Representation of various octahedral vibrations constituting the Raman modes.

($\omega_{A,B}$ i.e. antistretching and bending). Although LDC suggests that ω_S ($P2_1/n$) ~ 697 cm^{-1}, experimentally it was verified to be 645 cm^{-1}.[18] There are other low frequency modes (octahedral rotational mode) predicted by LDC, which are too weak in intensity to be observed in experiments.

Table 3.1: Lattice parameters of polycrystalline LMCO obtained from neutron diffraction [17]

Sample	**Space Group**	***a*** **(Å)**	***b*** **(Å)**	***c*** **(Å)**	**Angle (*θ* in degree)**
LTc	$P2_1/n$	5.5311(2)	5.4818(1)	7.7791(1)	α = γ= 90; β = 89.911(5)
HTc	$P2_1/n$	5.5104(1)	5.5162(1)	7.8063(2)	α = γ= 90; β = 89.352(3)

Sample	**Angle (θ in degree)**	**Bond Length (Å), d_{TM-O}**	
	O1-TM-O1 = 180.0(1)	TM-O1 = 2.000(3)	
	O2-TM-O2 = 180.0(2)	TM-O2 = 1.935(4)	
LTc	O3-TM-O2 = 180.0(2)	TM-O3 = 1.930(5)	
			$<d_{La-O}>$ = 2.6462(4)
	Co-O1-Mn = 160.6(3)	TM-O1 = 1.940(3)	t = 0.9473
	Co-O2-Mn = 165.3(6)	TM-O2 = 1.991(1)	
	Co-O3-Mn = 155.2(6)	TM-O3 = 2.055(3)	
HTc	O1-TM-O1 = 180.0(1)	TM-O1 = 1.901(3)	
	O2-TM-O2 = 180.0(2)	TM-O2 = 1.940(7)	
	O3-TM-O2 = 180.0(2)	TM-O3 = 1.960(7)	
			$<d_{La-O}>$ = 2.6521(3)
	Co-O1-Mn = 159.4(5)	TM-O1 = 2.066(3)	t = 0.9470
	Co-O2-Mn = 161.0(7)	TM-O2 = 2.012(7)	
	Co-O3-Mn = 159.8(7)	TM-O3 = 2.002(7)	

By looking at the spectra shown in Fig.3.1a, it is clear that the frequency of ω_S occurs at the same frequency in both the systems, while ω_{AB} (LT$_C$) > ω_{AB} (HT$_C$) ($\Delta\omega_{A,B}$ ~ 25 cm^{-1}). It is known from the literature [19] that the frequency of the octahedral breathing mode ω_A depends entirely on $\langle d_{TM-O}\rangle$ and $\theta_{O\text{-}TM\text{-}O}$, whereas, the frequency of ω_{AB} depends on $\langle d_{La-O}\rangle$ and $\theta_{TM-O-TM}$. Thus, one can predict that $\langle d_{La-O}\rangle$ and $\theta_{TM-O-TM}$ differ from LT$_C$ to HT$_C$ while $\langle d_{TM-O}\rangle$ and $\theta_{O\text{-}TM\text{-}O}$ are same. This scenario is validated by comparing the structures of LTcM and HTcM, where $\Delta\theta_{TM-O-TM} \approx 1.2^{\circ}/4.3^{\circ}/4.3^{\circ}$ for three different atomic positions of oxygen atoms respectively for LTcM vis-a-vis HTcM (see Table 3.1).

In order to understand the change in T_c, we have used the analogy from A-site doped systems. In general, T_c depends on total angular moment (J), nearest number of neighbours (n) and exchange energy (J_{ex}) given by $T_c = [2nJ_{ex} J(J+1)]/3k_B$. Here J_{ex} is proportional to the square of the transfer integral t_{ij} which is found to control the double exchange interactions in manganites, [20] a direct outcome of $\theta_{TM-O-TM}$. In the case of LMCO both the phases have identical n. Hence we attribute that $\Delta\theta_{TM-O-TM}$ are responsible for $\Delta T_c \approx 105$ K. The difference in the octahedral tilts has actually been routed to the difference in the degree of B-site ordering found from neutron diffraction.[17]

It is to be noted that, the tolerance factor, $t = d_{A-O}/\sqrt{2}d_{B-O} = 1$ for cubic perovskites with $\theta_{TM-O-TM} = 180^o$, where d_{A-O} is the bond length of A-site atom and oxygen, whereas d_{B-O} corresponds to the bond length of B-site atom and oxygen. When $t < 1$, the BO_6 octahedra tilts to lower angles ($\theta_{TM-O-TM} = 180^o - \phi$) at the expense of θ_{O-TM-O}, initiating geometrical distortions due to mismatch of the A-site ions in A-site substituted manganites. In our case, this is due to the d_{B-O}. In the present case of B-site doping, the tilting of octahedra is observed when the average tolerance factor (t) is, $\langle t (LT_C)\rangle = 0.9473$; $\langle t (HT_C)\rangle = 0.9470$. In the case of the manganese oxides, the MnO_6 octahedra when rotated along [111] axis gives rise to a rhombohedral symmetry and while rotated along [110] axis results in an orthorhombic symmetry. Such rotations reduce the $\theta_{Mn-O-Mn}$ from ideal 180^o to $(180^o - \phi)$, for $\phi(R\text{-}3C) < \phi(Pbnm/Pnma)$,[15] where ϕ is the tilt angle of the octahedra. The octahedra are tilted in such a way that $\langle d_{La-O}\rangle$ gets optimal bond length affecting the spring constant of the vibrating system. In our case, $\langle d_{La-O}\rangle$ = 2.646 Å and 2.652 Å for LTc and HTc respectively (as shown in the Table 3.1). In general, the tilt angle of the octahedra and $\langle d_{La-O}\rangle$, controls the rotational and bending modes respectively. When compared to HTc, $\langle d_{La-O}\rangle$ being shorter for LTc explains the higher frequency of vibrations of the bending mode. Although it is true that for higher values of ϕ (i.e more distortion), $\omega_{A,B}$ should be higher, which is not observed in our case, since both $\langle d_{La-O}\rangle$ and $\langle d_{TM-O}\rangle$ are higher for the HTc and thus reduces the bending frequency in comparison to LTc. Comparing the $\langle t\rangle$, $\omega_{A,B}$ and ϕ at 300 K are shown in Fig.3.2a. Similar Raman shift dependence on $\langle t\rangle$ was evaluated for A-site doped manganites, where $\langle t\rangle$ is dependent on A-site ion,[20] which is due to the internal pressure spanned by the A-site ion.[16] While such A-site doped manganites with $\langle t\rangle > 0.925$ had rhombohedral structure, our case of B-site (Co) doped $LaMnO_3$, retains $P2_1/n$ for higher values of ⟨t⟩ i.e. ⟨t⟩ = 0.9473/ 0.9470. The dependence of $\omega_{A,B}$ on temperature is plotted for LTc and HTc in Fig. 3.2b, which shows that $\omega_{A,B}$(LTc) > $\omega_{A,B}$(HTc) for the entire temperature range. In case of $\omega_{A,B}$(HTc), the initial hardening effect is due to ω_{latt} i.e d_{TM-O} as ϕ slightly varies and subsequently relaxes to an equilibrium position ensuring $\omega_{A,B}$ becomes almost invariable below a certain temperature. Such kind of initial hardening is found to be less featured in LTc.

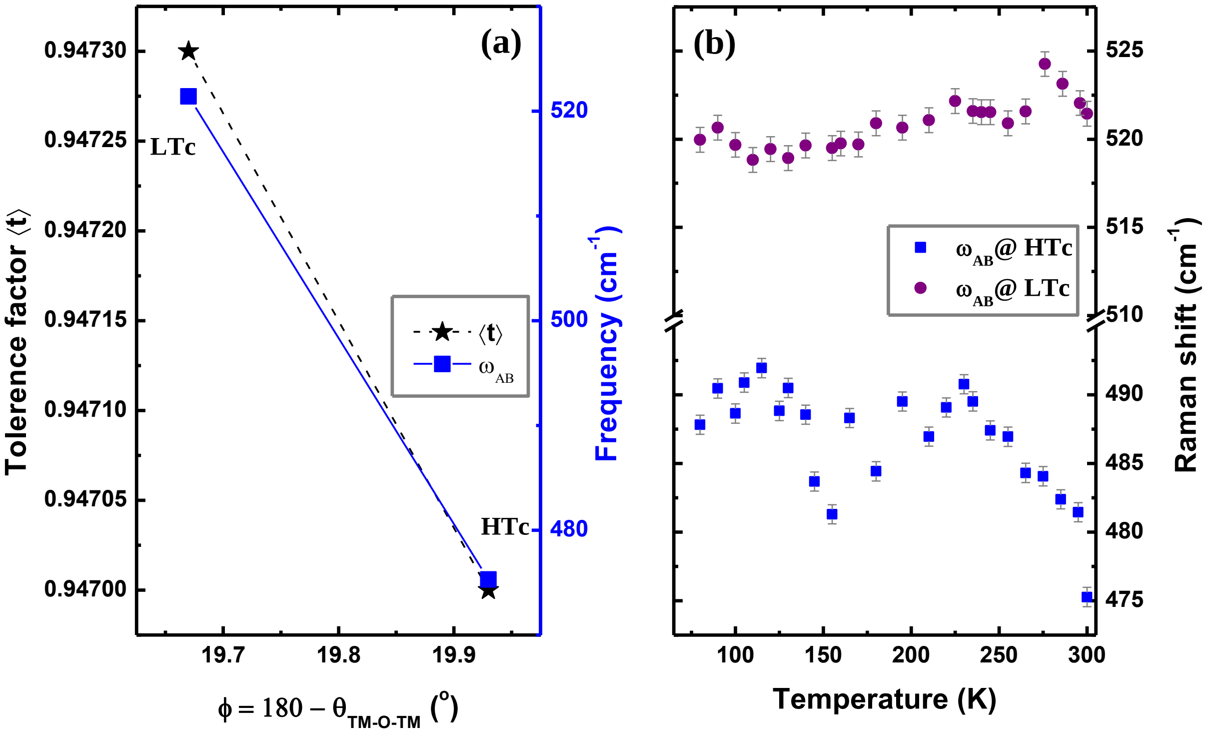

Figure 3.2: a) Dependence of ⟨t⟩, $\omega_{A,B}$ frequency as function of tilt angle 'ϕ'. b) Temperature dependence of $\omega_{A,B}$ frequency for LTc and HTc phases.

In order to understand both the phases individually, we have attempted to study the spin-phonon coupling for both LTc and HTc. Normally, in a magnetic material, the change in phonon frequency with temperature (Δω) has contributions from different sources such as $\Delta\omega_{latt}$ (change due to the variation of lattice parameters), $\Delta\omega_{anh}$ (anharmonicity), $\Delta\omega_{ren}$ (phonon renormalization due to electron-phonon coupling) and $\Delta\omega_{s\text{-}ph}$ (change due to spin-phonon coupling).[21] In both the cases of LTc and HTc, ω_S deviates from the regular dependence [22, 23] of $\omega_{anh}(T) = \omega_o - C(1+(2/e^{(\hbar\omega o/KT)}))$ for $T < T_c$, clearly indicating the nature of spin-phonon coupling as shown in Fig. 3.3a. In case of LTc, ω_S increases (hardens) as the temperature is lowered. This hardening is due to anharmonicity (ω_{anh}). Such kind of anharmonic nature is observed with mild deviation around 230 K, which is a clear signature of $\Delta\omega_{s\text{-}ph}$ of the residual HTc phase as inferred from χ'^{-1}.[17] Such effects are also observed from the linewidth of ω_s, (shown in Fig. 3.3b) which is related to phonon lifetime where there is a change in slope around 230 K due to

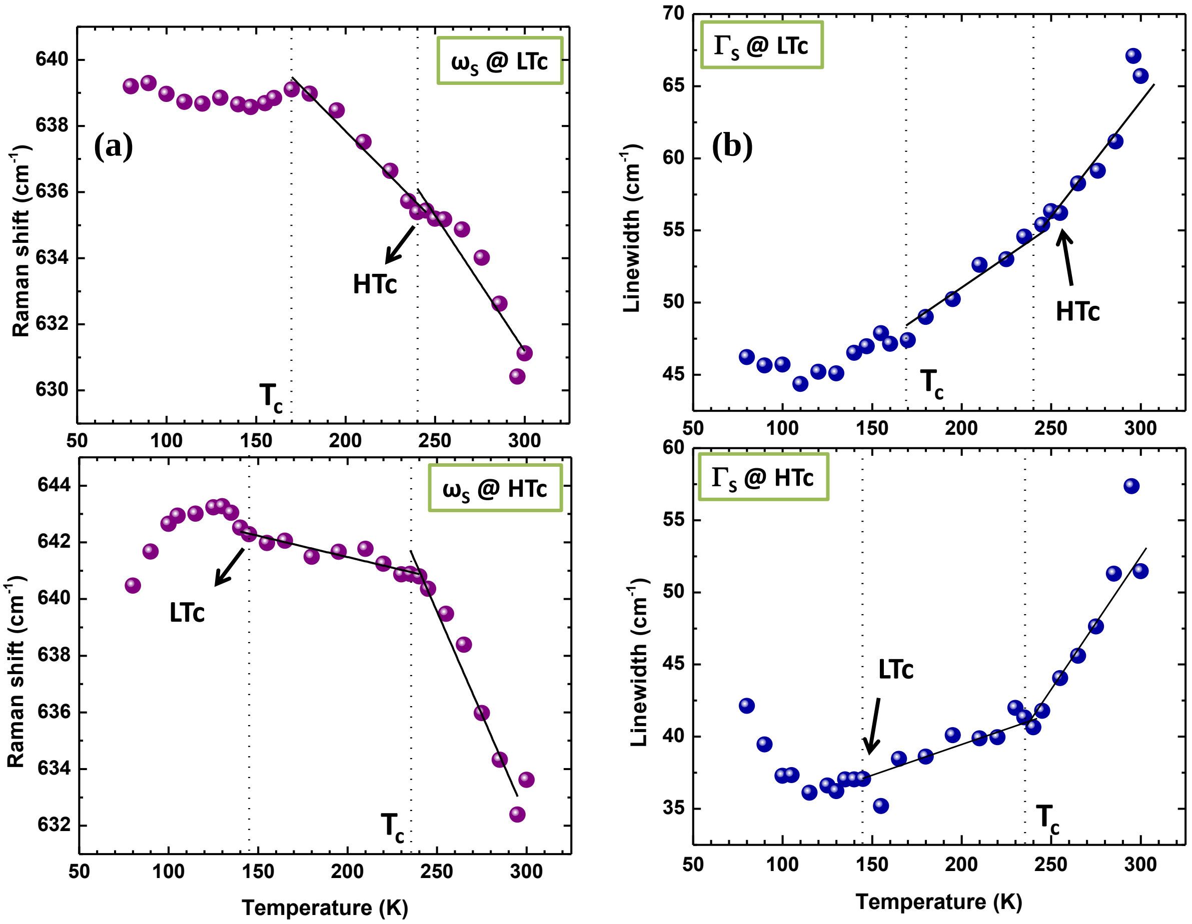

Figure 3.3: a) temperature dependence of ω_S frequency in LTc and HTc phases. b) corresponding temperature dependence of linewidth.

$\Delta\omega_{s\text{-}ph}$ (HTc). Below 230K, the behaviour of ω_S is driven by LTc phase. Interestingly, around 175 K we observe an anomalous behaviour in ω_S. This is due to two competing factors namely, strong spin-phonon coupling of HTc and approaching transformation in LTc. Hence this softening of ω_S below 175 K is the increasing influence of HTc phase. Below 125 K the LTc develops a strong spin-phonon coupling shown by the linewidth (see Fig. 3.3b).

In the case of HTc, anharmonic nature is observed till the temperature is lowered up to 235K (~ T_c of HTc phase). Below 235 K, the behaviour of ω_S is anomalous. It shows two distinct changes around 235 K and 125 K. Incidentally, this temperature corresponds with T_c of HTc and LTc respectively. It is interesting to note that Raman scattering shows evidence of the presence of LTc in the HTc phase, not observed by other methods. In order to explain this anomalous behaviour we have looked at the linewidth of ω_S, which is related to phonon lifetime. Fig. 3.3b shows anomalous behaviour in phonon lifetime around 235 K and 135 K. Upon decreasing temperature, one expects the linewidth to decrease. This deviation from the expected suggests phonon lifetime increase below T_c. This is due to a strong spin-phonon coupling. The presence of LTc is the reason for the dual effect. These observations are clear indications of the residual presence of one phase in the other. Residual phase can be detected from its $\Delta\omega_{s\text{-}ph}$ which could be observed from inelastic scattering, as it is a local probing technique unlike magnetic methods.

3.3.2 Single crystal LMCO:

In order to understand why the system did not trap any one of the magnetic phases, irrespective of the sample preparation technique, single crystals of LMCO are grown.

Table 3.2: Lattice parameters of single crystal LMCO obtained from XRD.

Sample	Space Group	*a* (Å)	*b* (Å)	*c* (Å)	Angle (θ in degree)
AG	*Pbnm*	5.5376(2)	5.5140(3)	7.8071(3)	$\alpha = \beta = \gamma = 90^0$
AN	*Pbnm*	5.5315(1)	5.5060(2)	7.7913(4)	$\alpha = \beta = \gamma = 90^0$

Sample	Angle (θ in degree)	Bond Length (Å), $d_{TM\text{-}O}$	
AG	O1-TM-O1 = 179.98(1)	TM-O1 = 1.929(4)	
	O2-TM-O2 = 180.00(0)	TM-O2 = 1.979(7)	$\langle d_{La\text{-}O}\rangle = 2.7781(10)$
	O2-TM-O2 = 179.98(1)	TM-O2 = 2.062(4)	t = 0.9872
	TM-O1-TM = 161.06(2)		
	TM-O2-TM = 156.46(1)		
AN	O1-TM-O1 = 179.98(1)	TM-O1 = 1.985(5)	
	O2-TM-O2 = 180.00(0)	TM-O2 = 1.961(3)	$\langle d_{La\text{-}O}\rangle = 2.7775(8)$
	O2-TM-O2 = 179.97(1)	TM-O2 = 2.043(3)	t = 0.9838
	TM-O1-TM = 157.74(1)		
	TM-O2-TM = 154.18(1)		

Since the crystal is grown from melt, one expects the best compositional homogeneity. However, it is noticed that the crystal possesses a huge lattice strain whose origin and nature is studied in detail here. A post-growth annealing procedure is executed to release this strain. The as grown crystal (AG) is crushed and the Rietveld refinement carried out on the powder XRD shows that the sample is crystallized into an orthorhombic *Pbnm* structure. The corresponding structural parameters are summarized in Table 3.2. The magnetic measurements on AG samples shows T_c ~149K which is higher compared to that of polycrystalline sample which could be due to the lattice strain induced during the synthesis. The AG sample has been annealed at 1450 ^oC for 50 hours to release the strain and the annealed (AN) sample shows T_c ~143K which is close to the T_c of the polycrystalline sample.

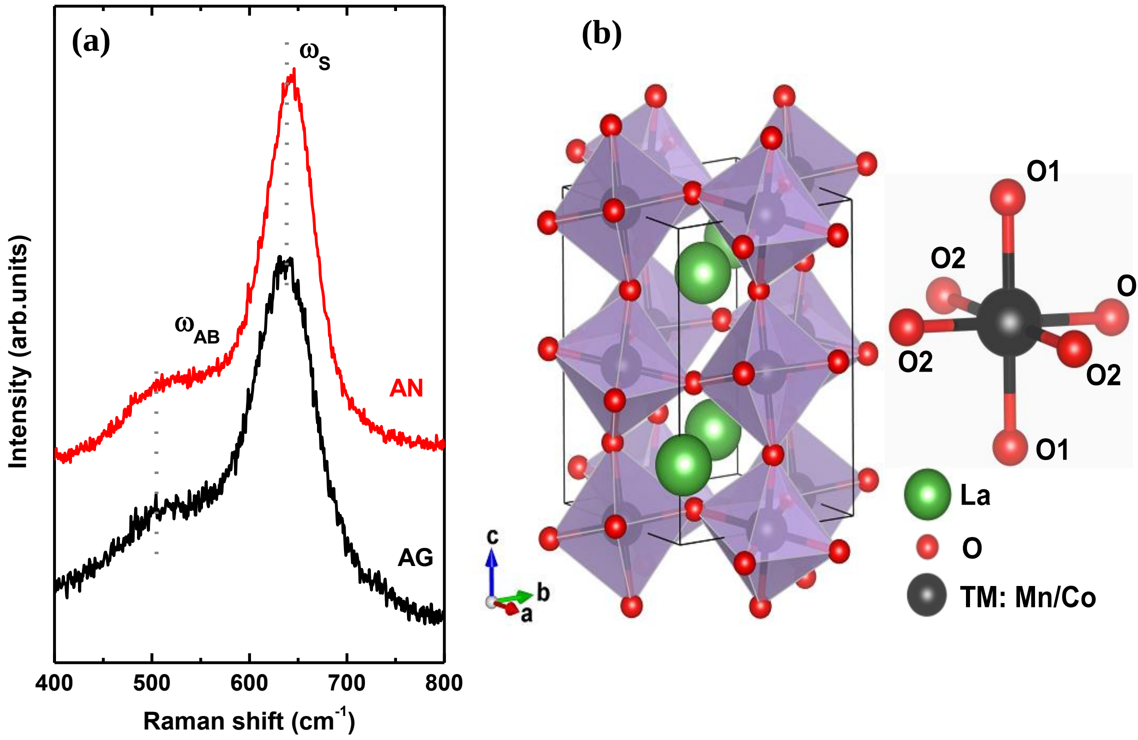

Figure 3.4: a) Raman spectra of as-grown (AG) and annealed (AN) single crystals of LMCO. b) Schematic representing the structure of *Pbnm* structure.

We used a Raman scattering study to explore the origin and the nature of the induced strain further, considering its adaptability to orthorhombic rare-earth manganites. Analyzing the Raman phonon modes can give an insight into the magnetic behavior of these systems. Fig. 3.4a shows the Raman spectra of both AG and AN samples. Intense peaks are found at 650 cm^{-1} in both samples, with pronounced humps at 510 cm^{-1}. These are assigned to the stretching (ω_S), mixed type ($\omega_{A,B}$; antistretching and bending). It was earlier reported[14] that the phonon modes in the LMCO Raman spectra were due to the TMO_6 octahedral vibration, which is very similar to that in orthorhombic $LaMnO_3$. The value of $\omega_{A,B}$ depends predominantly on the octahedral tilt angle $\phi = 180 - \theta_{TM\text{-}O\text{-}TM}$; the higher the ϕ, the greater the $\omega_{A,B}$. The value of ϕ being large in *Pbnm* as compared to *R*-3*C* and $P2_1/n$, justifies the fact that $\omega_{A,B}$ is higher in *Pbnm.* Also, the predicted value of $\omega_{A,B}$ is around 490 cm^{-1} in *R*-3*C* and $P2_1/n$.[24] To visualize the lattice strain effects on the Raman modes, we have performed a 2D Raman mapping (not shown here as it is a part of the thesis of Dr. Kaustuv Manna, department of physics, Indian Institute of Sciences (IISc), Bangalore) of frequency of ω_S in 200×200 μm^2 area on the AG and AN sample surfaces. We found that peak position of ω_S is not same throughout the surface on AG. The ω_S frequency is maximum (~650 cm^{-1}) in some regions (AG1) whereas in the nearby territory (AG2), a lower value (~630 cm^{-1}) is seen. Since the location of the phonon mode of ω_S is influenced by the distortion within the TM-O octahedra, the octahedral deformation varies in different regions. It is inferred that the high frequency region (AG1) possesses compressive octahedral deformation with a lower $<d_{TM\text{-}O}>$. This, leads to the tensile octahedral distortion of nearby low frequency region (AG2) with stretched $<d_{TM\text{-}O}>$. However, the peak position of ω_S is more or less uniform throughout the surface of AN suggesting annealing of AG releases most of the strain.

It is necessary to correlate the present Raman spectroscopic observation with the structural parameters (shown in Table 3.2) obtained from Rietveld refinement analysis. It is evident from Table-2 that $<d_{TM\text{-}O}$ (AG)> = 0.9968 $<d_{TM\text{-}O}$ (AN)>, which is consistent with the compressive nature of the octahedral distortion in AG. The post-growth annealing process causes tilting of the oxygen octahedra by $\Delta\theta_{TM\text{-}O\text{-}TM} \approx 2.8^o$. This is also reflected in the tolerance factor of AN, *t*(AN) = 0.9838, whereas *t*(AG) = 0.9872. The octahedral tilting causes a reduction of J_{ex} in the AN sample and lowers the T_c. We are already aware that the octahedral tilt angle $\theta_{TM\text{-}O\text{-}TM}$, and the $<d_{La\text{-}O}>$ together govern the bending mode frequency. In the AG and AN samples, the $<d_{La\text{-}O}>$ is found to be same, whereas tilt angles are dissimilar ($\Delta\theta_{TM\text{-}O\text{-}TM} \approx 2.8^o$). This would suggest a higher value of the $\omega_{A,B}$ mode in the case of AN. However, the values of $\omega_{A,B}$ was observed to be the same. This is significant and can be understood from the overriding influence of $<d_{TM\text{-}O}$ (AN)> in compensating for the effect of octahedral tilting on the bending mode.

In order to understand the effect of lattice distortions in more detail and explore the possibility of spin-phonon coupling, temperature dependent Raman scattering was examined for both AG as well as AN samples. The temperature variations of the stretching mode (ω_S) frequency for both the samples, is plotted in Fig. 3.5a. In general, magnetic insulator like LMCO, it is postulated that the dominant contribution comes from $\Delta\omega_{anh}$ and $\Delta\omega_{s\text{-}ph}$. The behavior of ω_S in the AG1 region is distinctly different from that of the AG2 region as seen in Fig. 3.5a. The frequency of ω_S increases with decreasing temperature till 241 K in the AG2 region following normal anharmonic behavior.[22-23] In contrast, ω_S frequency decreases with a lowering of temperature in AG1. Strain relaxation in the compressed region (AG1) induced by the contraction in the tensile region (AG2) is the likely origin for such behavior. In both the cases, ω_S deviates from the regular anharmonic behavior below 240 K (~ T_{C1}) and 150 K (~ T_{C2}). Correspondingly, there is an increase in linewidth [see Fig. 3.5b] indicating a shorter lifetime of the phonon, and suggesting the existence of strong spin-phonon coupling in and around the ferromagnetic transition temperatures. Similar behavior is observed in polycrystalline LMCO also as

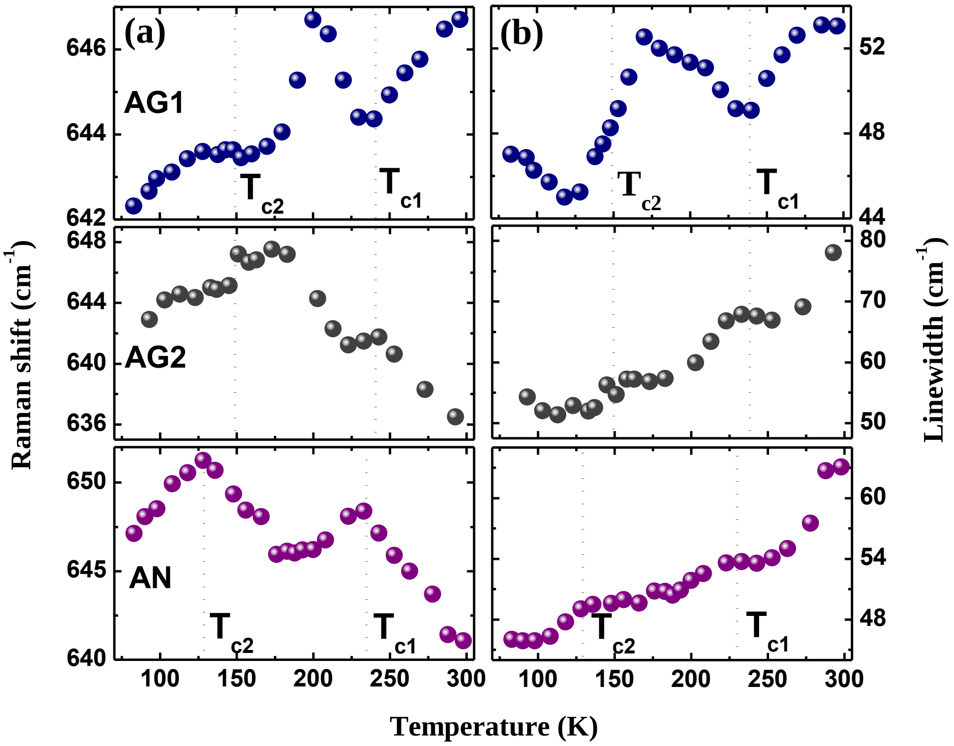

Figure 3.5: a) Temperature dependence of ω_S frequency in AG and AN single crystals. b) Corresponding temperature dependence of linewidth.

discussed earlier [see Fig. 3.2]. This goes on to substantiate that the presence of two magnetic ground states is inevitable in LMCO.

Interestingly, below T_{C1} ω_S hardens in AG1 and softens in the AG2 region. This relates to different magnetic exchange interactions involved in spin-phonon coupling (for example, magnetic interactions can be switched from antiferromagnetic to ferromagnetic in Fe, just by varying the separation between the Fe atoms).[25-27] At T ~ 200 K, we observe a change in trend in both AG1 and AG2. This is due to the crossover from one ground state to an upcoming second ground state. The behavior in both the regions is complementary and suggests a strong strain-coupled system. The same value of ω_S (~ 642 cm^{-1}) at 77 K in both regions, AG1 and AG2, confirms that the low temperature magnetic ground state has similar magnetic interactions throughout the AG sample. The behaviour of ω_S in the annealed crystal is comparable to that of the AG2 region of the as-grown crystal as well as that of the polycrystalline sample. This suggests that annealing leads to a strain-relaxation.

3.4 Conclusions:

LMCO with two different ferromagnetic transition temperatures have been studied by Raman scattering. The two ground states were observed in both the polycrystalline and the single crystalline samples. As grown crystals have a lot of strain built in due to these competing ground states. Annealing of the single crystal relaxes the strains and behaves exactly as the polycrystalline samples. The difference in the T_c for $LaMn_{0.5}Co_{0.5}O_3$ has been evaluated and it could be understood on the basis of the degree of distortion present in the two phases. The observed difference in T_c for the two phases is due to the lattice distortion influenced by the tilting of octahedra pertaining to the Mn/Co ordering directly affects the exchange energy. The lattice distortion effects were understood by the careful examination of the behaviour of ω_{AB} in both HTc and LTc samples which were related to the difference in T_c values.

3.5 Bibliography:

1. R. Ramesh, and N. A. Spladin, *Nature Mater.*, 6, 21 (2007).
2. W. Prellier, M. P. Singh, and P. Murugavel, *J. Phys.: Condens. Matter*, 17, R803 (2005).
3. W. Eerenstein, N. D. Mathur, and J. F. Scott, *Nature (London)*, 442, 759 (2006).

4. M. P. Singh, K. D. Truong, and P. Fournier, *Appl. Phys. Lett.*, 91, 042504 (2007).
5. R. I. Dass, J. Q. Yan, and J. B. Goodenough, *Phys. Rev. B*, 67, 014401 (2003).
6. P. Padhan, H. Z. Guo, P. LeClair, and A. Gupta, *Appl. Phys. Lett.*, 92, 022909 (2008).
7. M. Viswanathan, and P. S. Anil Kumar, *Phys. Rev. B*, 80, 012410 (2009).
8. A. P. Umesh, V. B. Sapre, S. V. Moharil and K. R. Priolkar, *J. Phys.: Condens. Matter*, 21, 235405 (2009).
9. V. P. Gnezdilov, A. V. Yeremenko, Yu. G. Pashkevich, P. Lemmens, G. Güntherodt, S. V. Shiryaev, G. L. Bychkov, and S. N. Barilo, *Low Temp. Phys.*, 29, 963 (2003).
10. C. Autret, J. H ejtmanek, K. Knızek, M Marysko, Z Jirak, M Dlouha, and S. Vratislav, *J. Phys.: Condens. Matter*, 17, 1601 (2005).
11. C. Zener, *Phys. Rev.*, 82, 403 (1951).
12. P. G. deGennes, *Phys. Rev.*, 118, 141 (1960).
13. J. B. Goodenough, A. Wold, R. J. Arnott, and N. Menyuk, *Phys. Rev.*, 124, 373 (1961).
14. C. L. Bull, D. Gleeson, and K. S. Knight, *J. Phys.: Condens. Matter*. 15, 4927 (2003).
15. J. B. Goodenough and J. M. Longo, *Landolt-Börnstein Tabellen* (Springer, Berlin, 1970), Vol. III/4a.
16. H. Y. Hwang, S-W. Cheong, P. G. Radaelli, M. Marezio, and B. Batlogg, *Phys. Rev. Lett.* 75, 914 (1995).
17. M. Viswanathan, P. S. Anil Kumar, V. S. Bhadram, C. Narayana, A. K. Bera, and S. M. Yusuf, *J. Phys.: Condens. Matter.*, 22, 346006 (2010).
18. M. N. Iliev, M. V. Abrashev, A. P. Litvinchuk, V. G. Hadjiev, H. Guo, and A. Gupta, *Phys. Rev. B*, 75, 104118 (2007).
19. C. L. Bull and P. F. McMillan., *J. Solid State Chem.*, 177, 2323 (2004).
20. V. A. Amelitchev, B. Güttler, O. G. Yu, A. R. Kaul, A. A. Bosak, and G. A. Yu, *Phys. Rev. B* 63, 104430 (2001).
21. E. Granado, N. O. Moreno, A. Garcıa, J. A. Sanjurjo, C. Rettori, I. Torriani, S. B. Oseroff, J. J. Neumeier, K. J. McClellan, S. W. Cheong, and Y. Tokura, *Phys. Rev. B*, 58, 11435 (1998).
22. I. P. Ipatova, A. A. Maradudin, and R. F. Wallis *Phys. Rev.*, 155, 882 (1967).

23. J. Laverdiére, S. Jandl, A. A. Mukhin, V. Y. Ivanov, V. G. Ivanov, and M. N. Iliev, *Phys. Rev. B*, 73, 214301 (2006).
24. M. Balkanski, R. F. Wallis, and E. Haro *Phys. Rev. B*, 28, 1928 (1983).
25. S. C. Abrahams, L. Guttman, and J. S. Kasper, *Phys. Rev.*, 127, 2052 (1962).
26. U. Gonser, C. J. Meechan, A. H. Muir, and H. Wiedersich, *J. Appl. Phys*,. 34, 2373 (1963).
27. A. Kubetzka, P. Ferriani, M. Bode, S. Heinze, G. Bihlmayer, K. von Bergmann, O. Pietzsch, S. Blugel, and R. Wiesendanger, *Phys. Rev. Lett.*, 94, 087204 (2005).

Chapter 4

Raman Scattering Studies on Spin-Phonon Coupling in $R\mathrm{CrO_3}$ (R-Y, Lu, Gd, Eu, Sm)

The author's main contribution in this chapter is to perform temperature dependent Raman experiments on $R\mathrm{CrO_3}$ *and to analyze the data. These samples were synthesized by Prof. Sundaresan's group, JNCASR.*

4.1 Introduction:

Magnetoelectric multiferroic materials with their coupled ferroelectric and ferromagnetic order parameters are promising for developing a new generation of both electrically and magnetically controlled multifunctional devices.[1-5] Multiferroic materials are broadly classified into two types; in type I multiferroics, the ferroelectricity and magnetism occur at high temperatures but with different temperature scale. However, the couplings between the two order parameters are rather weak. Type II multiferroics are generally centrosymmetric and magnetic, where the ferroelectricity is caused by certain types of magnetic ordering leading to electronic polarizability. In the well-known example of $TbMnO_3$, the manganese moments order antiferromagnetically at $T_N = 41$ K and at 25 K it undergoes another magnetic transition below which a cycloidal spin structure breaks the inversion symmetry and thus induces ferroelectricity.[6] In case of $HoMnO_3$,[7] a collinear magnetic ordering with E-type magnetic structure gives rise to ferroelectricity. It has been shown recently that canted antiferromagnetic ordering with two non-equivalent spin pairs in the orthoferrite, $SmFeO_3$[8] induces ferroelectric polarization at the magnetic ordering temperature of iron. Rajeswaran *et al.*[9] have reported electric polar order at the magnetic ordering temperature of chromium in the isostructural orthochromites, $RCrO_3$ with magnetic R-ion, where the interactions between R^{3+} and Cr^{3+} ions have been suggested to be responsible for the switchable polarization. In such systems, the interplay between magnetic and electric order could be mediated through spin-lattice coupling. Thus, probing the local structure would provide a good understanding of the multiferroic behavior in this class of materials.

Raman spectroscopy is an ideal technique to study the local structural changes due to magnetic ordering effects and it has been used in the past to elucidate the physics of multiferroics.[10-12] Raman spectroscopy of rare-earth orthorhombic manganites, $RMnO_3$ (R = Pr, Nd, Sm, Eu, Gd, Tb, Dy, Ho, Y) have been studied extensively in the past. [13-18] In case of hexagonal $YMnO_3$ [19] and $LuMnO_3$,[20] ferroelectric to paraelectric phase transition is accompanied by tilting of MnO_5 polyhedra which is correlated with the changes in Raman modes related to rare-earth atom displacements. In the case of orthorhombic $TbMnO_3$, new Raman modes have been observed at the cycloidal spin ordering temperature suggesting their magnetoelectric origin. [21] Though orthorhombic manganites have been studied extensively in the past, very few reports of Raman studies exist in the case of orthochromites.

In this chapter, we report the temperature-dependent Raman studies of rare-earth orthochromites, $R\mathrm{CrO}_3$ with magnetic (Gd and Sm) and nonmagnetic (Y, Lu and Eu) *R*-ions to exemplify the role of rare-earth magnetism in inducing the ferroelectricity in these materials. We have chosen these rare-earth ions to account for the effect of both rare-earth ionic size and its magnetism on the spin-phonon coupling and ferroelectricity in $R\mathrm{CrO}_3$. Lu^{3+} and Y^{3+} are both nonmagnetic which have smaller and comparable ionic radii, whereas nonmagnetic Eu^{3+} has higher ionic radii and is comparable to the size of the magnetic Gd^{3+} and Sm^{3+} ions. Such careful selection is indeed a necessary prerequisite to demarcate the effects that can arise specifically due to either the magnetism of R^{3+} ion or the size of R^{3+} ion or both. Due to leakage effects and oxygen nonstoichiometry in LaCrO_3, La^{3+} has not been chosen in the present study even though it is nonmagnetic ion.

4.2 Experimental details:

Polycrystalline samples of $R\mathrm{CrO}_3$ (*R*=Y, Lu, Gd, Eu, Sm) were prepared by the solid state reaction of stoichiometric quantities of $R_2\mathrm{O}_3$ and $\mathrm{Cr}_2\mathrm{O}_3$ at 1673 K for 12 hours followed by several intermittent grinding and heating. Phase purity was confirmed by Rietveld refinement on the x-ray powder diffraction data collected with Bruker D8 Advance diffractometer. Raman spectroscopic measurements have been carried out in back scattering geometry using 532 nm excitation wavelength and a custom built spectrometer equipped with a SPEX TRIAX 550 monochromator and a liquid nitrogen cooled charge-coupled device (CCD; Spectrum One with CCD 3000 controller, ISA JobinYovn) as described in the experimental section in chapter 2 . Laser power at the sample was kept at ~6mW and typical spectral acquisition time is 1 min. Temperature dependent measurements were done using heating stage unit (Linkam THMS 600) equipped with a temperature-controller (Linkam TMS 94) with temperature accuracy of ±1K. Lorentzian functions were used to fit the spectral profile.

4.3 Results and discussion:

Fig. 4.1 shows the room temperature Raman spectra of $R\mathrm{CrO}_3$ (*R*=Y, Lu, Gd, Eu and Sm) in the spectral range 100-600 cm^{-1}. $R\mathrm{CrO}_3$ has an orthorhombic (*Pnma*) structure with 24 Raman active modes which are classified as $\Gamma_{\mathrm{Raman}} = 7A_g + 5B_{1g} + 7B_{2g} + 5B_{3g}$.[15] These modes are assigned by following the earlier Raman reports on orthorhombic $R\mathrm{MnO}_3$ and the recent room-temperature Raman study on $R\mathrm{CrO}_3$

systems.[14, 15, 22] The phonon modes below 250 cm^{-1} in YCrO$_3$ and below 200 cm^{-1} in all the other samples are related to lattice modes involving *R*-ion motion. Region above 200 cm^{-1} (250 cm^{-1} in the case of YCrO$_3$) consists of various modes involving vibrations of *R*

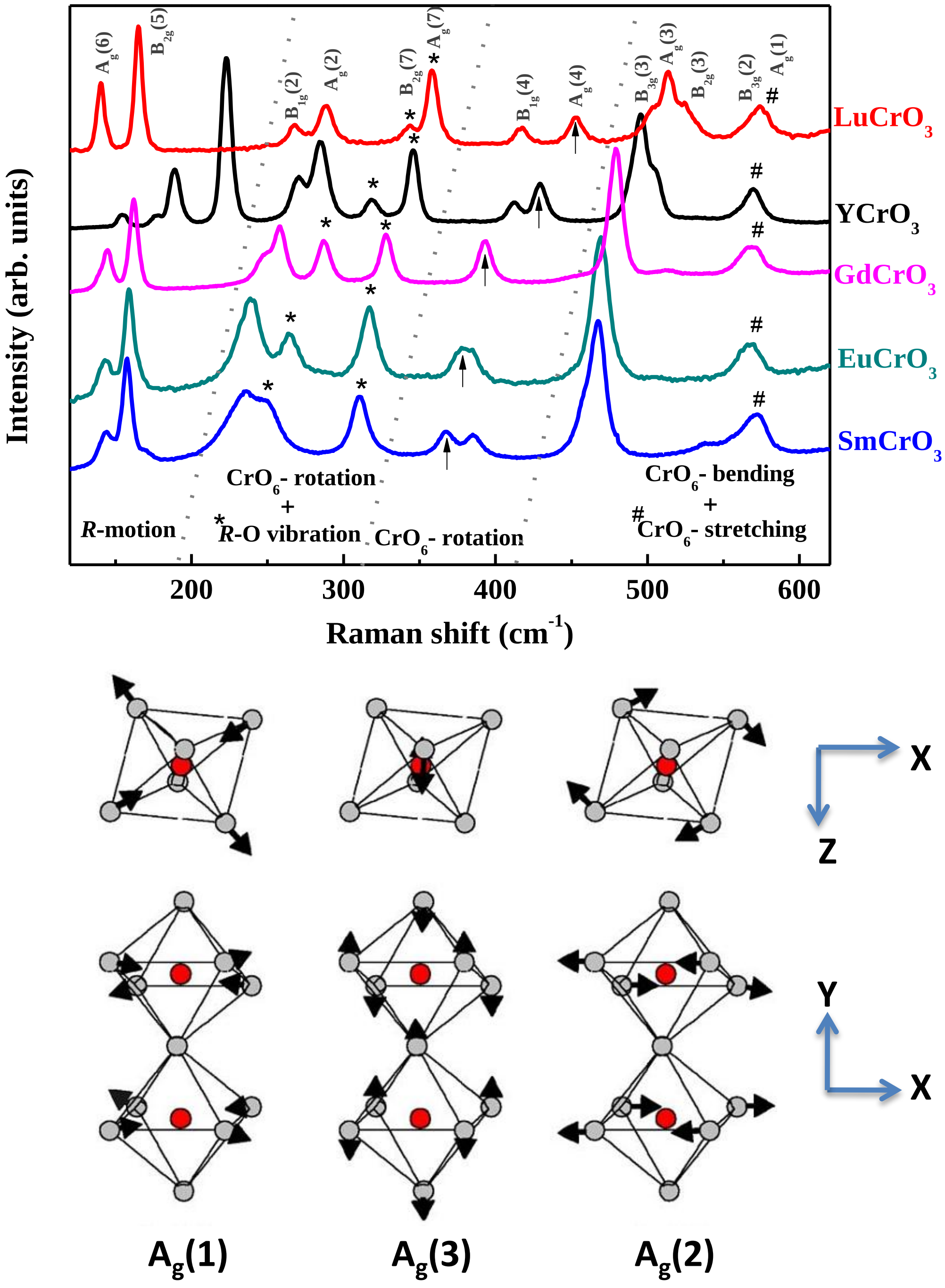

Figure 4.1: (Top) Unpolarized Raman spectra of *R*CrO$_3$ collected at 295 K. Mode assignment has been done based on Ref. [14, 15, 22]. (Bottom) Schematic representing the atomic motions of A$_g$(1), A$_g$(3) and A$_g$(2) modes (adopted from Ref. 14).

atom and oxygen. A$_g$(1) mode is related to the anti-symmetric stretching vibrations of CrO$_6$ octahedra (see the Fig. 4.1(bottom)). B$_{1g}$(2), A$_g$(2) are octahedral rotations around crystallographic y-axis and B$_{1g}$(4), A$_g$(4) are rotations around x-axis (P*bnm* setting). The doublet (A$_g$(7) and B$_{2g}$(7)) at around 300 cm^{-1} in YCrO$_3$, LuCrO$_3$, GdCrO$_3$, EuCrO$_3$ and a singlet (A$_g$(7)) in SmCrO$_3$ are related to *R*-O vibrations. B$_{3g}$(3) is bending mode of CrO$_6$ octahedra. Most of these phonon modes shift to low frequency with increase in ionic radii of *R*-ion ($r_Y > r_{Lu} > r_{Gd} > r_{Eu} > r_{Sm}$) as seen in the case of orthorhombic manganites. [14] A detailed spectral analysis of these systems has been reported recently.[22]

4.3.1 Temperature effects on anti-stretching mode:

The temperature effects on the anti-symmetric stretching mode A$_g$(1) frequency and corresponding line widths are plotted in Fig.4.2 in the temperature range 77-298K. As mentioned in Chapter 3, temperature dependent behavior of phonon mode of frequency ω(T) is given as[23]

$$\omega(T) = \omega(0) + \Delta\omega_{qh}(T) + \Delta\omega_{anh}(T) + \Delta\omega_{sp-lat}(T) + \Delta\omega_{el-ph}(T) \qquad (4.1)$$

where ω(0) is the frequency at zero K. The term $\Delta\omega_{qh}(T)$ includes the changes in phonon frequency due to the quasi-harmonic effect which corresponds to the change in the lattice volume. Whereas $\Delta\omega_{anh}(T)$ gives the intrinsic anharmonic contribution to the frequency. $\Delta\omega_{sp-lat}(T)$ represents the change in phonon frequency due to spin-lattice (spin-phonon) coupling which is caused by the phonon modulation of spin-exchange integral. Effects of electron-phonon coupling on phonon frequency is given by $\Delta\omega_{el-ph}(T)$ which can be neglected when the carrier concentration is low.

As seen in Fig.4. 2, phonon frequencies increase with decreasing temperature up to the transition temperature (T_N/T_N^{Cr}) in all the three systems which is attributed to the anharmonic effect. The dotted line in the Fig.4.2 is the fit to the experimental data above T_N^{Cr} with the equation,[24]

$$\omega_{anh} = \omega_0 - C(1 + 2/(e^{\hbar\omega/KT} - 1)) \qquad (4.2)$$

where ω$_0$ and C are adjustable parameters. It is clear from Fig.4.2 that A$_g$(1) phonon frequency deviates from the above relation below T_N^{Cr} in all the three systems, which could arise from the quasi-harmonic effects along with spin-phonon coupling. However, it is interesting to note the different behavior of phonons below T_N^{Cr} for different *R*-ions.

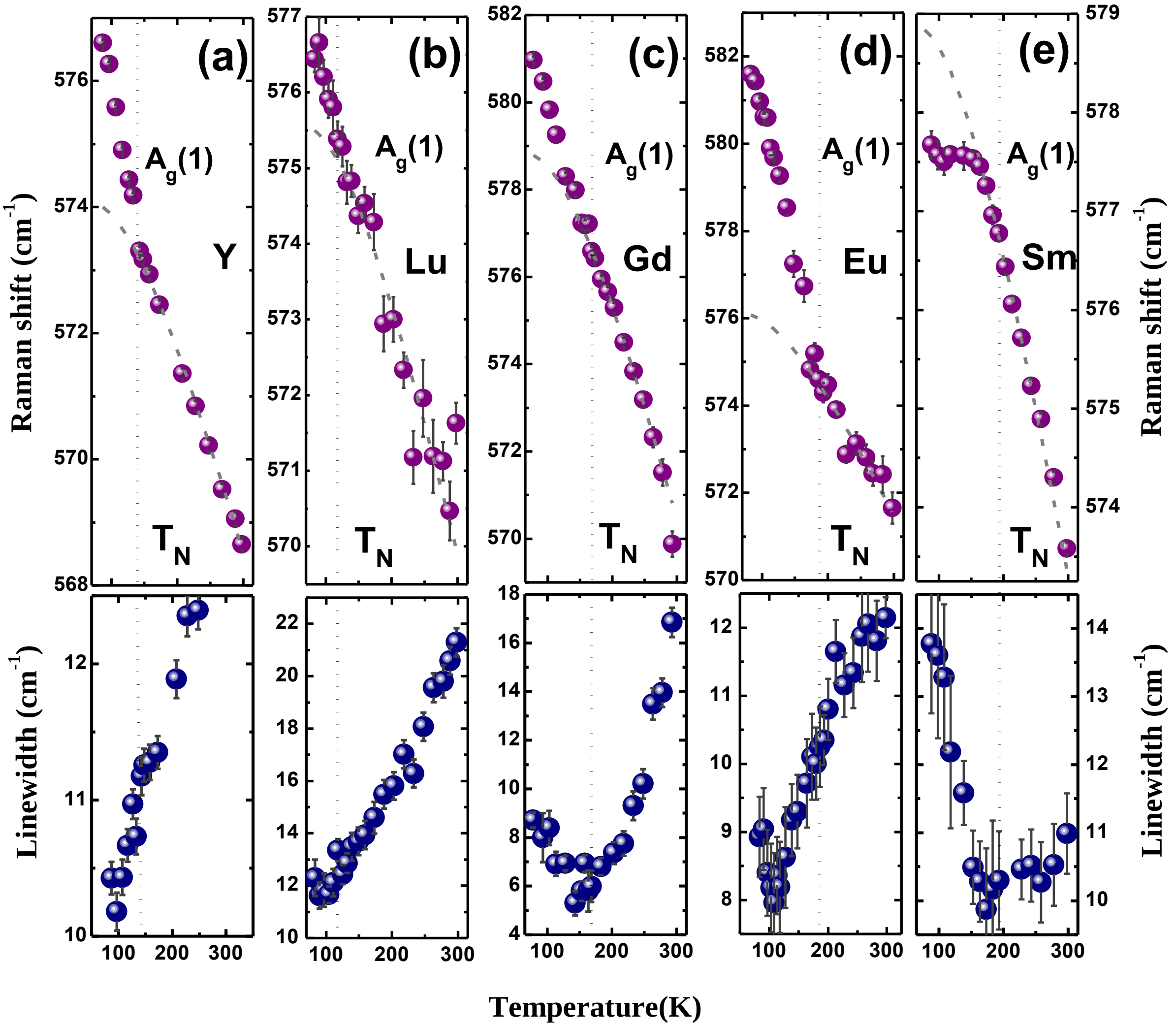

Figure 4.2: Temperature dependence of A$_g$(1) mode frequency and linewidth in a) YCrO$_3$ b) LuCrO$_3$ c) GdCrO$_3$ d) EuCrO$_3$ e) SmCrO$_3$.

An anomalous hardening of the A$_g$(1) mode is observed in all the samples except in SmCrO$_3$ wherein a softening is observed. The observed hardening of A$_g$(1) mode is consistent with the earlier observation where a reduction in unit cell volume is reported for YCrO$_3$ and is attributed to magnetostriction. [25] Though we are not aware of such studies in other samples, it is possible that a similar magnetostriction effect can occur in all these samples due to magnetic ordering of Cr^{3+} ions. The observation that the phonon mode below T_N^{Cr} softens in SmCrO$_3$ and hardens in *R*CrO$_3$ (*R*=Y, Lu, Gd, Eu) may be related to different magnetic interactions between magnetic R^{3+} and Cr^{3+} ions as reported earlier.[9]

To give more insight into the origin of anomalous behavior of A$_g$(1) mode frequency, we have plotted the temperature dependence of the corresponding linewidth in Fig. 4.2 (bottom panels). Since Raman linewidths are related to phonon lifetime which will not be effected by subtle lattice volume changes due to magnetostriction, it is better to study linewidths rather than phonon frequencies to observe the spin - phonon coupling. We observe that the line width increases below T_N^{Cr} in the case of magnetic *R*-ions (Gd, Sm), whereas there are no significant changes observed in the case of nonmagnetic *R*-ions (*Y*, *Lu* and *Eu*). Generally, the Raman linewidths are expected to decrease monotonously with temperature due to anharmonicity [25] as seen in the case of nonmagnetic *R*-ion (see Fig. 4.2).

In contrast, an anomalous increase in the linewidth below T_N^{Cr} is observed in magnetic *R*-ion which signifies there is a contribution from the effects that change the phonon lifetime. Generally, phonon lifetimes are effected by various processes such as, amorphization, spin-phonon coupling [26, 27] and electron-phonon coupling.[28] Since these materials are insulators and have not lost their crystallinity, we can unequivocally attribute the change in linewidth to spin-phonon coupling.

4.3.2 Temperature effects on octahedral rotational and bending modes:

Temperature dependence of in-phase and out-of-phase octahedral rotations about x-axis (A$_g$(4), B$_{1g}$(4)) is shown in left panel of Fig. 4.3. All the samples show softening in rotation about x-axis below T_N^{Cr} which may be predominantly due to the effect of magnetostriction. The behavior of out-of-phase bending mode, B$_{3g}$(3) as shown in right panel of Fig. 4.3 is similar to that observed for rotational modes about y-axis. It should be noticed that the A$_g$(4), B$_{1g}$(4) and B$_{3g}$(3) modes in SmCrO$_3$ exhibit an additional anomaly near 140 K which may be linked to the impending observed spin-reorientation transition occurring at much lower temperature (around 40 K).[9]

In contrast, an anomalous increase in the linewidth below T_N^{Cr} is observed in magnetic *R*-ion which signifies there is a contribution from the effects that change the phonon lifetime. Generally, phonon lifetimes are effected by various processes such as, amorphization, spin-phonon coupling [26, 27] and electron-phonon coupling.[28] Since these materials are insulators and have not lost their crystallinity, we can unequivocally attribute the change in linewidth to spin-phonon coupling.

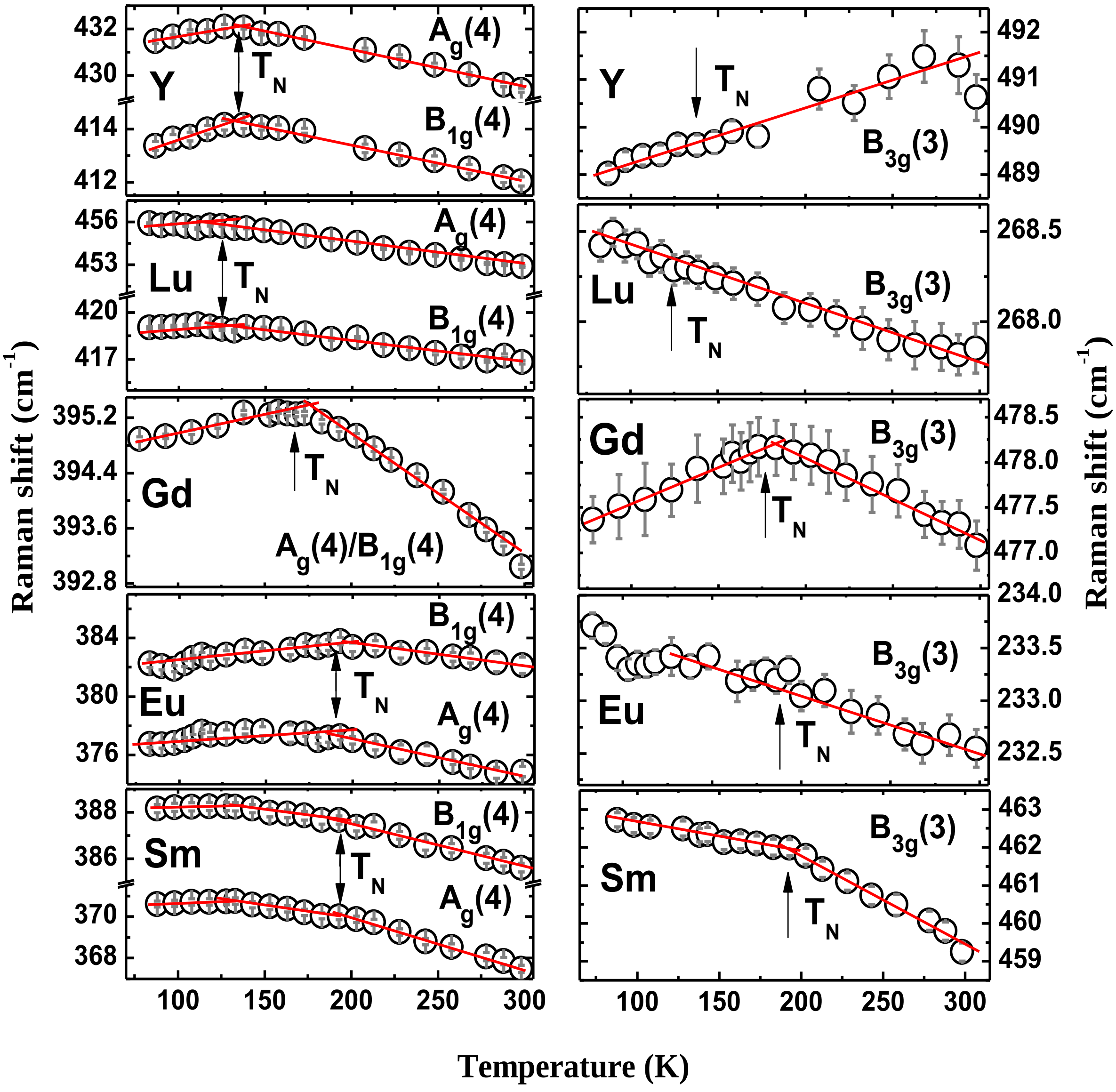

Figure 4.3: Frequency variation with respect to temperature of A$_g$(4), B$_{1g}$(4) and B$_{3g}$(3) modes.

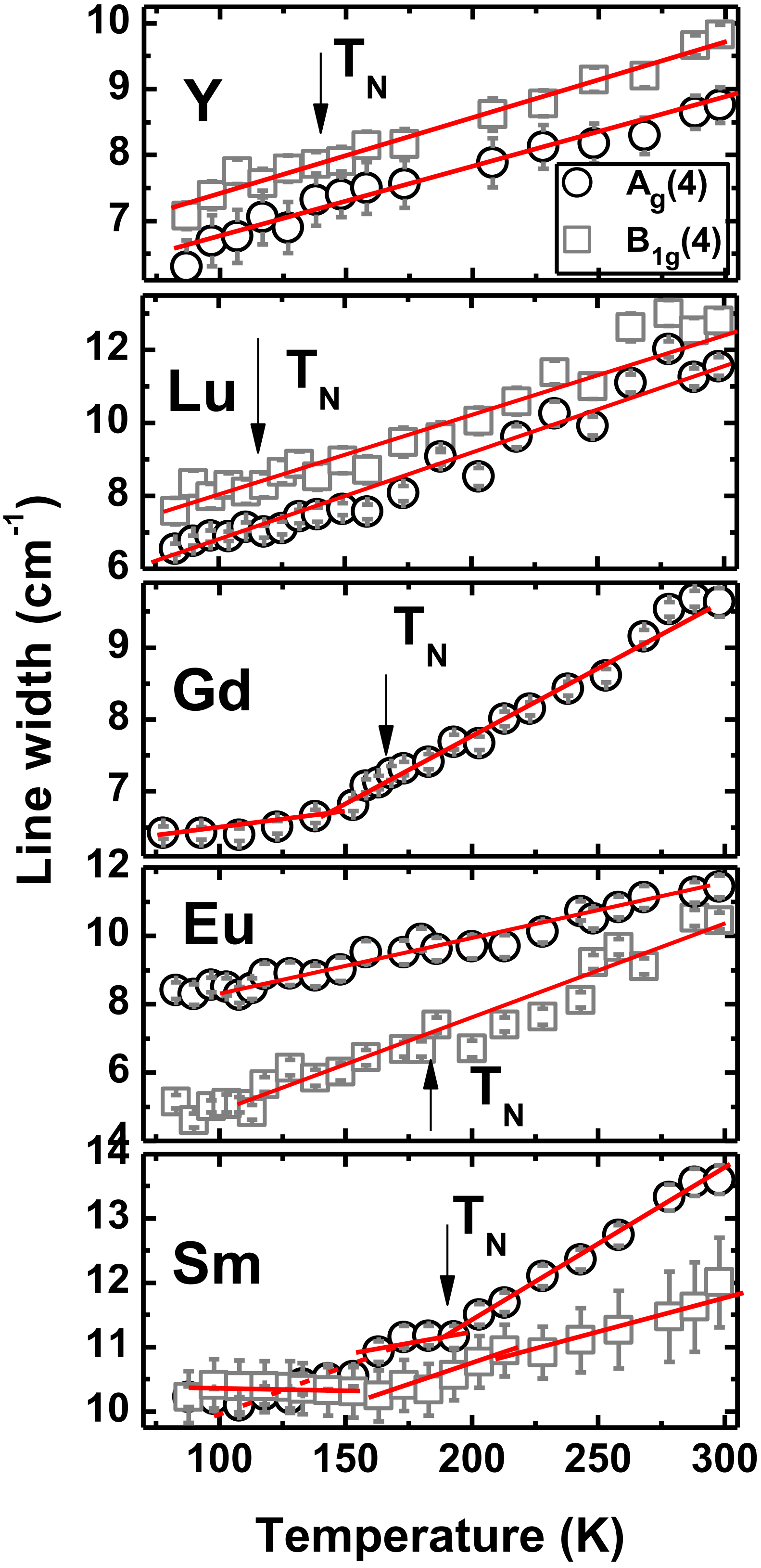

Figure 4.4: Variation of linewidth with temperature of A$_g$(4) and B$_{1g}$(4) modes.

4.3.3 Effect of temperature on *R*-O vibrations:

Temperature dependence of the A$_g$(7) and B$_{2g}$(7) mode frequencies and the corresponding line widths are shown in Fig.4.5. These are lattice modes involving *R*-O vibrations. We notice from the left panel that all the samples show phonon anomalies at T_N^{Cr} but this is relatively weak in *Y*, *Lu* and *Eu*. Such a small change in phonon frequency along with no change in phonon linewidth suggests that these may solely be due to magnetostriction. However, a strong softening of these modes along with the anomalies in

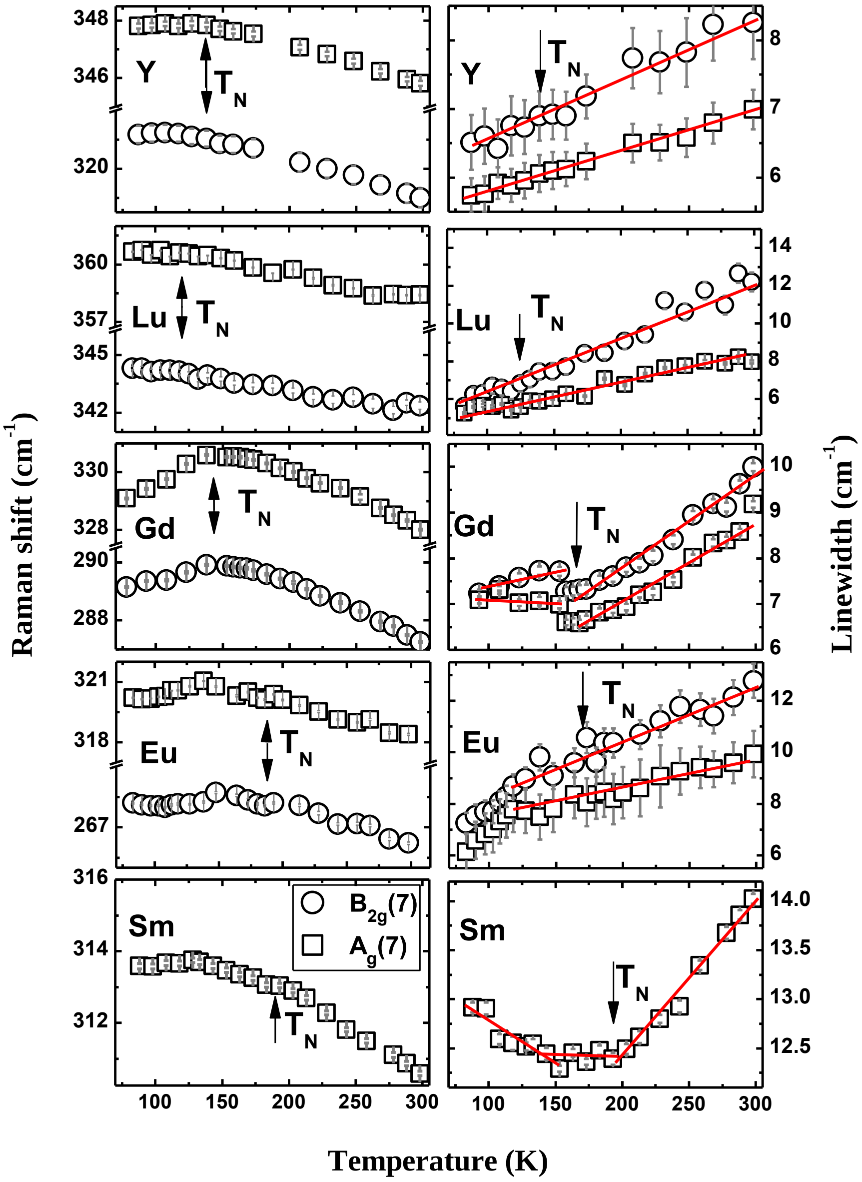

Figure 4.5: Temperature dependence of frequency and linewidth of A$_g$(7) and B$_{2g}$(7) modes.

their line width (right panel of Fig. 4.5) in *Gd* and *Sm* confirms yet again the presence of the spin-phonon coupling.

In general, we expect appearance of spin correlation effects on phonons whenever there is spin ordering present in the system. However, in the present case we observe spin-phonon coupling effects below T_N^{Cr} only in the case of magnetic *R*-ion which indicates the role of rare-earth magnetism in the appearance of spin-phonon coupling. It should be emphasized here that rare-earth spin ordering temperatures are much lower compared that of chromium, the paramagnetic state of rare-earth can influence the magnetic structure of *R*CrO$_3$ below T_N^{Cr} [29]. We suggest that these magnetic *R*-Cr interactions enhance the spin-phonon coupling in GdCrO$_3$ and SmCrO$_3$, which is otherwise very weak as in YCrO$_3$, LuCrO$_3$ and EuCrO$_3$.

4.3.4 Possible explanation for magneto dielectric effect:

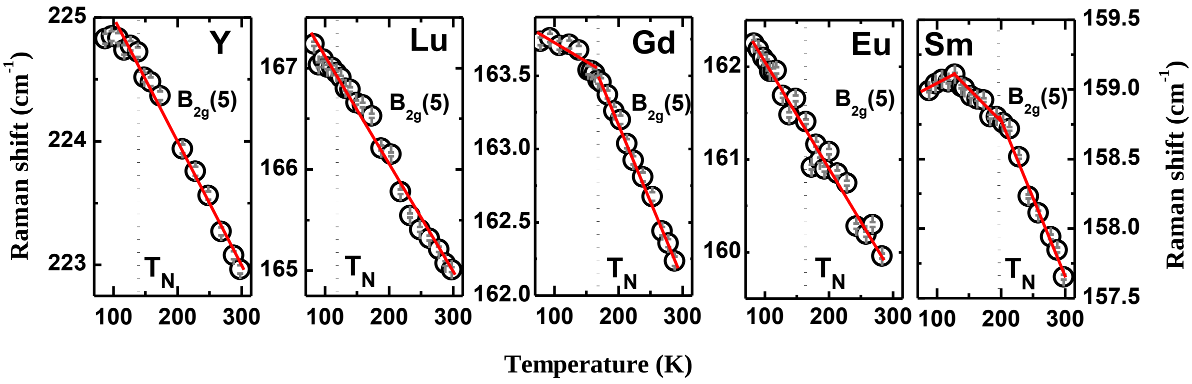

Figure 4.6: Variation of B$_{2g}$(5) mode frequency with temperature.

In Ref. 9, there are two possible mechanisms proposed for the ferroelectric polarization observed in *R*CrO$_3$. i) The magnetic *R*-Cr interactions can lead to ferroelectric polarization in presence of tiny local distortions in the lattice. ii) The external poling field (~2 kV/cm) which is used to measure the polarization can also produce small distortions around *R*-ions which can result in ferroelectric polarization triggered by *R*-Cr interactions. To validate the above predictions, we have looked at magnetic ordering effects on lattice mode B$_{2g}$(5) which involve the *R*-ion motion (see Fig. 4.6). We found a relatively strong softening of this mode below T_N^{Cr} in *Gd* and *Sm* which is absent in the case of *Y*, *Lu*, *Eu*. The softening of the mode indicates weakening of *R*-O bond suggesting a possible displacement of *R*-ion from its position. To probe the poling field effects on the lattice modes, we have collected Raman spectrum of GdCrO$_3$ as a function of the electric-field (~2 kV/cm) at 77 K (see Fig. 4.7, especially (b)). We have plotted the field dependence of lattice modes in Fig. 4.7a. We found no change in these mode frequencies and profiles in presence of field (see Fig. 4.7c). This rules out the possibility of field induced polar order.

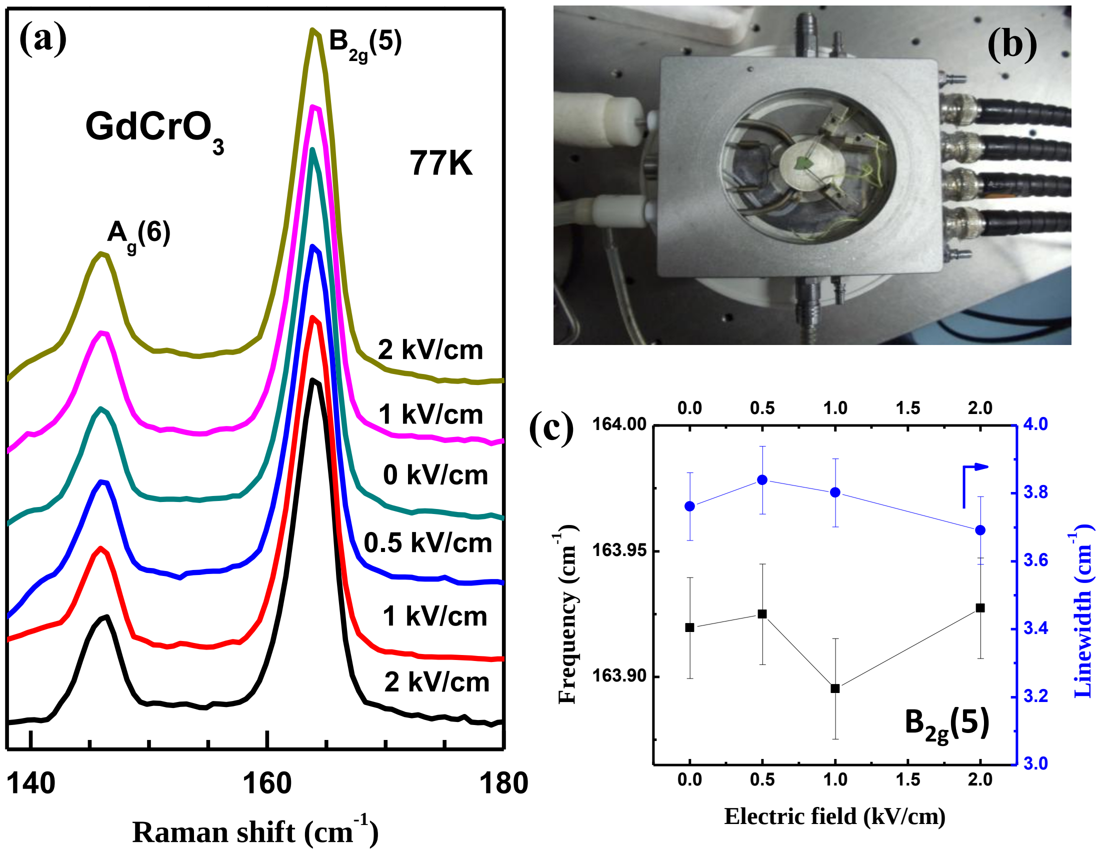

Figure 4.7: a) Electric field dependence of lattice modes $A_g(6)$, $B_{2g}(5)$ in GdCrO$_3$. b) Picture depicting the sample inside cryo-stage with electrical contacts. c) Electric field dependence of $B_{2g}(5)$ mode parameters.

In the past, efforts were made to understand the correlation between spin-phonon coupling and magnetoelectric effect in various manganites, ferrites and nickelates.[10, 30-32] A theoretical model has been proposed by considering the spin-phonon coupling and *Mn* spin frustration to explain the origin and nature of the multiferroic phases in RMnO$_3$.[33] It is also suggested that a frustrated intra and inter-plane Mn-Mn, R-Mn interactions arise in

*R*MnO$_3$ below *Mn* ordering temperature which would favour the displacement of *Mn* to minimize the frustration. This displacement of *Mn* as proved by neutron diffraction studies would lead to ferroelectricity in *R*MnO$_3$.[34] In the present *R*CrO$_3$ case, the situation might be similar except that there is a strong spin-phonon coupling, here, due to the magnetic *R*-Cr interactions which may displace the magnetic R^{3+} resulting in ferroelectric polarization.[9, 35] A detailed neutron diffraction studies and first-principle calculations would help in understanding these systems better.

4.4 Conclusions:

In conclusion, the present Raman results clearly demonstrate spin-phonon coupling in rare-earth orthochromites *R*CrO$_3$ with magnetic *R*-ion. We observe along with phonon frequency changes, decrease in phonon lifetimes both in modes involving CrO$_6$ octahedra as well as magnetic R^{3+} ion. This clearly suggests a spin-phonon coupling mediated magnetic interactions between R^{3+} and Cr^{3+} ions, leading to a local distortion of R^{3+} ion in the unit cell. These interactions along with the softening of magnetic *R*-ion modes suggest that the origin of ferroelectric polarization in rare-earth orthochromites may be related to the displacement of *R*-ion.

4.5 Bibliography:

1. W. Eerenstein, N. D. Mathur, and J. F. Scott, *Nature*, 442, 759(2006).
2. D. Khomskii, *Physics*, 2, 20 (2009).
3. C. N. R. Rao, and C. R. Serrao, *J. Mater. Chem.*, 17, 493(2007).
4. M. Fiebig, T. Lottermoser, D. A. Frohlich, V. Goltsev, and R. V. Pisarev, *Nature*, 419, 818 (2002).
5. T. Arima, A. Tokunaga, T. Goto, H. Kimura, Y.Noda and Y. Tokura *Phys. Rev. Lett.*, 96, 097202 (2006).
6. T. Kimura, *Annu. Rev. Mater. Res.*, 37, 387 (2007).
7. Z. J. Huang, Y. Cao, Y. Y. Sun, Y. Y. Xue and C. W. Chu, *Phys. Rev. B*, 56, 2623 (1997).
8. J. H. Lee, Y. K. Jeong, J. H. Park, M. A. Oak, H. M. Jang, J. Y. Son and J. F. Scott, *Phys. Rev. Lett.*107, 117201(2011).
9. B. Rajeswaran , D. I. Khomskii , A. Sundaresan, and C. N. R. Rao, *Phys. Rev. B*, 86, 214409 (2012).
10. W. S. Ferreira *et.al.*, *Phys. Rev. B*, 79, 054303 (2009).

11. B. Mihailova, M. M. Gospodinov, B. Güttler, F. Yen, A. P. Litvinchuk, and M. N. Iliev, *Phys.Rev. B*, 71, 172301 (2005).
12. P. Mandal, V. S. Bhadram, Y. Sundarayya, C. Narayana, A. Sundaresan and C. N. R. Rao, *Phys. Rev. Lett.*, 107, 137202 (2011).
13. M. N. Iliev, M. V. Abrashev, H. G. Lee, V. N. Popov, Y. Y. Sun, C. Thomsen, R. L. Meng, and C. W. Chu, *Phys. Rev. B*, 57, 2872 (1998)
14. M. N. Iliev, M. V. Abrashev, J. Laverdiére, S. Jandl, M. M. Gospodinov, Y. Q. Wang, and Y. Y. Sun, *Phys. Rev. B*, 73, 064302 (2006).
15. J. Laverdiere, S. Jandl, A. A. Mukhin, V. Y. Ivanov, V. G. Ivanov, and M. N. Iliev, *Phys.Rev. B*, 73, 214301 (2006).
16. L. Martin-Carron, A. de Andres, M. J. Martinez-Lope, M. T. Casais, and J. A. Alonso, *Phys. Rev. B*, 66, 174303 (2002).
17. P. Kumar, S. Saha, D. V. S. Muthu, J. R. Sahu, A. K. Sood, and C. N. R. Rao, *J. Phys.:Condens. Matter*, 22, 115403 (2011).
18. E. Granado, et al., *Phys. Rev. B*, 58, 11435 (1998).
19. H. Fukumura, S. Matsui, H. Harima, K. Kisoda, T. Takahashi, Yoshimura.T, and and NFujimura, *J. Phys.: Condens. Matter*, 19, 365239 (2007).
20. A. Ghosh, J. R. Sahu, S. V. Bhat, and C. N. R. Rao, *Solid State Sciences*, 11, 1639 (2009).
21. P. Rovillain, M. Cazayous, Y. Gallais, A. Sacuto, M. A. Measson, and H. Sakata, *Phys.Rev. B*, 81, 054428 (2010).
22. M. C. Weber, J. Kreisel, P. A. Thomas, M. Newton, K. Sardar, and R. I. Walton, *Phys. Rev. B*, 85, 054303 (2012).
23. E. Granado, A. Garcia, J. A. Sanjurjo, C. Rettori, I. Torriani, F. Prado, R. D. Sanchez, A. Caneiro, and S. B. Oseroff, *Phys. Rev. B*, 60, 11879 (1999).
24. M. Balkanski, R. F. Wallis, and E. Haro, *Phys. Rev. B*, 28, 1928 (1983).
25. M. Udagawa, K. Kohn, N. Koshizuka, T. Tsushima, and K. Tsushima, *Solid State Commun.*, 16, 779 (1975).
26. R. Gupta, G.V. Pai, A. K. Sood, T. V. Ramakrishnan, and C. N. R. Rao, *Euro. Phys. Lett.*, 58, 778 (2002).
27. D. J. Lockwood and M. G. Cottam, *J. Appl. Phys.*, 64, 5876 (1988).
28. P. B. Allen, *Phys. Rev. B*, 6, 2577(1972).
29. T. Yamaguchi, K. Tsushima, *Phys. Rev. B*. 8, 5187 (1973).

30. A. J. Moreira and A. Almeida, *Ferroelectrics - Physical Effects*, edited by Mickaël Lallart., (In Tech) 2011, pp. 303-328.
31. P. Kumar *et al*., *Phys. Rev. B*, 85, 134449 (2012).
32. C. Girardot., J. Kreisel, S. Pignard, N. Caillault and F. Weiss, *Phys. Rev. B*, 78, 104101(2008).
33. M. Mochizuki, N. Furukawa and N. Nagaosa, *Phys. Rev. B*, 84, 144409 (2011).
34. X. Fabregès, S. Petit, I. Mirebeau, S. Pailhès, L. Pinsard, A. Forget, M. T. Fernandez-Diaz and F. Porcher, *Phys. Rev. Lett*., 103, 067204 (2009).
35. N. Shamir, H. Shaked and S. Shtrikman, *Phys. Rev. B*, 24, 6642 (1981).

Chapter 5

Effect of Pressure on the Octahedral Distortions in *R*CrO_3: A Raman Scattering study

The author's main contribution in this chapter is to perform high pressure Raman measurements on RCrO_3 *and analyzing the data. These samples were provided by Prof. Sundaresan's group at JNCASR.*

5.1 Introduction:

As mentioned in Chapter 1 and seen in Chapter 3, the physical properties of perovskites are sensitive to the structure and BO$_6$ octahedral tilting distortions. This can be controlled by external pressure, temperature and variations in A and B cation size.[1,2] Among perovskites, rare-earth based compounds (RMO$_3$; M is transition metal) have attracted lots of attention recently due to their multifunctional properties which have fascinating device applications.[3-5] Especially, RMnO$_3$ exhibit multiferroicity depending on the size of the rare-earth ion. For example, YMnO$_3$ which crystallizes in hexagonal ($P6_3cm$) symmetry exhibits geometric ordering driven multiferroicity[6] whereas, magnetic ordering driven multiferroicity is observed in orthorhombic (*Pbnm*), e.g. TbMnO$_3$.[7] Interestingly, external pressure can modify the octahedral distortions and can turn the hexagonal manganites into orthorhombic ones.[8] In other words, pressure as a parameter can alter the multiferroic properties of these systems.

Rare-earth orthochromites RCrO$_3$ (*R*-rare earth) which are isostructural to orthorhombic manganites have a wide variety of applications in catalysis,[9] fuel cells,[10] etc. As discussed in Chapter 4, these materials were found to be multi-ferroic below the Néel temperature of Cr^{3+} (T_N^{Cr}) only when rare-earth is magnetic ion (i.e Gd, Sm) due to the exchange interactions between the magnetic R^{3+} ions and the ordered Cr^{3+} sublattice mediated through a spin-phonon coupling.[11,12] Moreover, the spin configuration in RCrO$_3$ can also play a crucial role in inducing ferroelectricity.[11] It is thus logical to study the structural changes in RCrO$_3$ either by doping (chemical pressure) or by applying hydrostatic pressure. External pressure could indeed be considered as a fine tuning of the chemical substitution, hence would give information for both the doping as well as the volume effects.

In the past, many studies[13-17] have been aimed at understanding the pressure behaviour of orthorhombic perovskites and a general rule has also been proposed.[15] It predicts that the octahedral tilting distortions decrease with pressure in the case of trivalent (3:3 group) perovskites (e.g. GdAlO$_3$). A comparative study [17] of pressure evolution of octahedral distortions in YMO$_3$ (M=Al, Cr, Ti) negates this generalization and suggests the importance of size of B-cation radii for predicting the pressure induced structural changes in orthorhombic ABO$_3$ perovskites. In the same report, it is shown that the structure of YCrO$_3$ becomes more distorted at higher pressures. On the contrary, a recent report [18] on LaCrO$_3$ suggests that it undergoes structural transformation to a higher symmetry phase (rhombohedral, $R\bar{3}c$) at around 5 GPa indicating the importance of R-ion radii in understanding the high pressure behaviour of RCrO$_3$. However, there are no studies reported on the role of R-ion radii in the pressure dependent orthorhombic distortion despite its obvious relation with the degree of octahedral tilts.[16]

As shown in Fig. 5.1, the T_N^{Cr} of these systems increases with increase in R-ion size which is expected as the octahedral tilts (for instance, tilt angle 'θ') reduce with increase in R-ion radii which effects the exchange interactions. The highest T_N^{Cr} possible here, is around 280K (for LaCrO$_3$) which is still below the room temperature. So, it is important to further reduce the distortions to bring the T_N^{Cr} to room temperature and above for device applications. Thus, our present pressure dependent studies are important and significant. In our study, we have used pressure dependent Raman mode behaviour of various orthochromites (RCrO$_3$) up to 20 GPa. Raman scattering is very sensitive to the structural distortions and is a unique tool for pressure dependent structural studies on

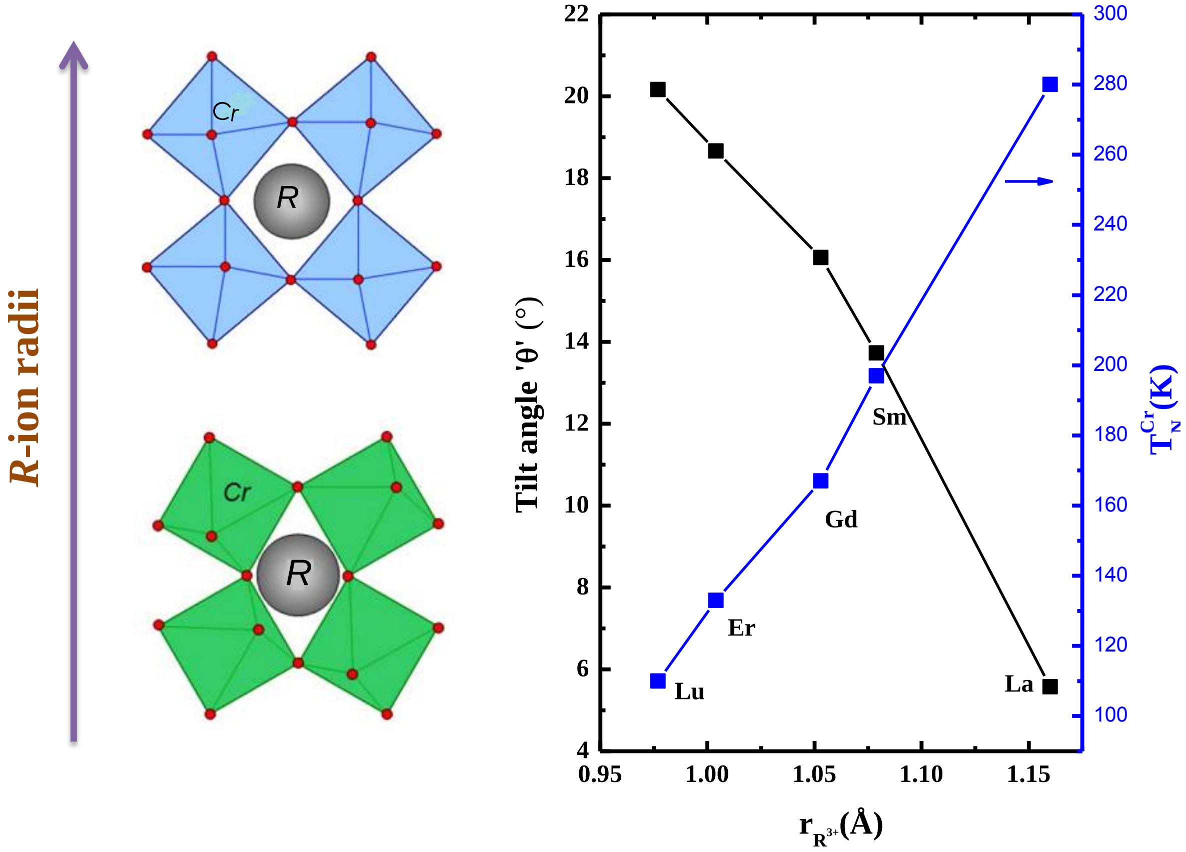

Figure 5.1: R-ion size dependence of tilt angle 'θ' and Néel temperature T_N^{Cr} of RCrO$_3$. 'θ' and T_N^{Cr} values are taken from Ref. 22 and Ref. 11,18 respectively.

perovskites. We have carefully selected the compounds; LuCrO$_3$, TbCrO$_3$, GdCrO$_3$, EuCrO$_3$ and SmCrO$_3$ for our present Raman studies. The selection, here, is entirely based on the rare earth ion size (r_R^{3+}: Lu^{3+} < Tb^{3+} < Gd^{3+} < Eu^{3+} < Sm^{3+}). It should be note that many more rare-earth chromates could be added to the list, unfortunately, due to the non availability of these samples, we choose these without any disadvantage in tackling the problem at hand.

5.2 Experimental details:

Powder samples of all the rare-earth chromites studied here were prepared using solid state method. The details of the sample synthesis are given in Ref.11. The pellets of these powder samples were crushed and pieces of required size were selected for high pressure studies. A membrane type high pressure diamond anvil cell (DAC) from BETSA, France has been used for the high pressure experiments. The diamond culet size is 400 microns. Methanol, ethanol (4:1) mixture has been used as a pressure transmitting medium and for *in situ* pressure measurements a ruby chip has been loaded along with sample inside DAC. Unpolarized Raman spectra were recorded in the back scattering geometry using a custom-built Raman spectrometer equipped with a laser with excitation wavelength 532 nm and laser power of ~5 mW at the sample. The Raman spectra were deconvoluted using multiple Lorentzian functions with a proper background correction. For details, one can refer to the Chapter 2.

5.3 Results and discussion:

Rare-earth orthochromites (*R*CrO$_3$) crystallize in orthorhombically distorted perovskites structure with space group *Pnma*. These orthochromites possesses two structural distortions namely i) rotation (tilts) of the CrO$_6$ octahedra around [010] and [101] which can be quantified by the tilt angles "φ" and "θ" respectively[19] and ii) rare-earth ion (R^{3+}) displacement. These two distortions together govern the symmetry lowering from an ideal cubic perovskites type ($Pm\bar{3}m$) to orthorhombic type (*Pnma*) and activate zone-centre Raman modes.[20] Group theory suggests 24 Raman active modes for orthorhombic *Pnma* with four formula units in the unit cell:[21]

$$7A_g+5B_{1g}+7B_{2g}+5B_{3g} \tag{5.1}$$

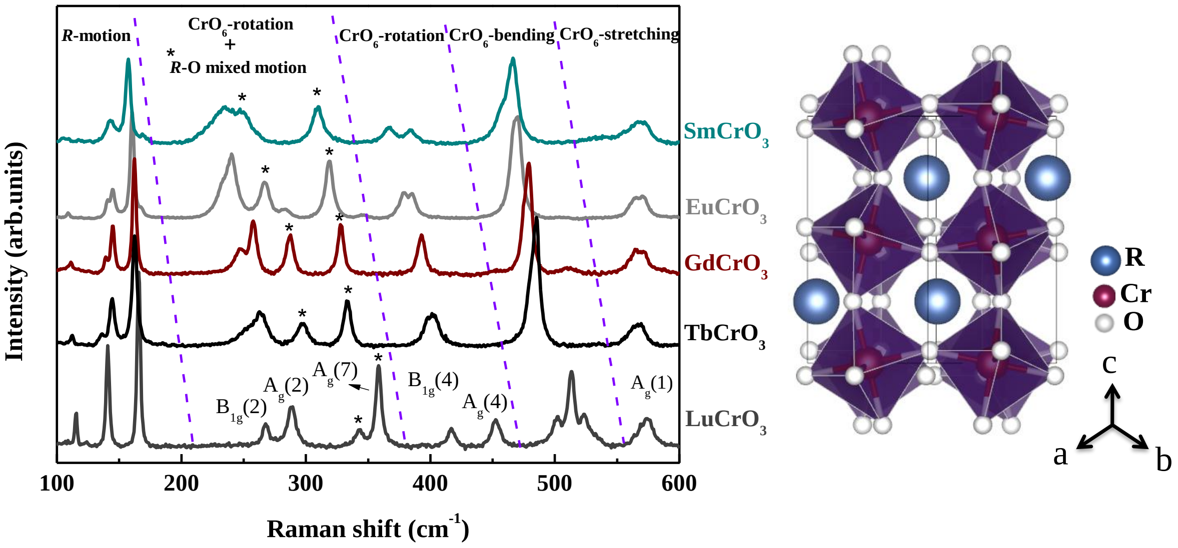

Figure 5.2: Unpolarized Raman spectra of $RCrO_3$ recorded at 300 K.

Unpolarized Raman spectra of $RCrO_3$ (R= Sm, Eu, Gd, Tb and Lu) is shown in Fig.5.2. Though group theory predicts 24 Raman active modes, we observe only around 11-15 modes. It is possible that certain modes may be too weak to be observed or may be at very low wavenumbers much below our experimental cut off. The detailed analysis of the mode assignment exists elsewhere;[12,22] for the sake of continuity we provide here a discussion on certain important modes useful for our discussion from the Fig.5.2. The sharp and intense modes below 200 cm^{-1} are related to R-ion vibrations and are expected to be less affected by the orthorhombic distortion. There are two pairs of CrO_6 octahedral rotational modes which are very sensitive to the orthorhombic distortion. Among them, $A_g(2)$ and $A_g(4)$ are considered as soft modes and the frequency of these modes vary linearly with tilt angles "φ" and "θ" respectively. The modes which are sandwiched between these pairs of rotational modes (between 250 and 400 cm^{-1}) are related to rare-earth and oxygen mixed vibrations in RO_{12} polyhedra. Modes related to bending and stretching of Cr-O bonds within the octahedra appear at the high frequency end of the spectra (see Fig.5.2). Particularly, anti-stretching vibration of the Cr-O bonds inside octahedra ($A_g(1)$) is important as its frequency is very sensitive to the changes in Cr-O bond lengths.

5.3.1 Pressure effects on octahedral rotational modes:

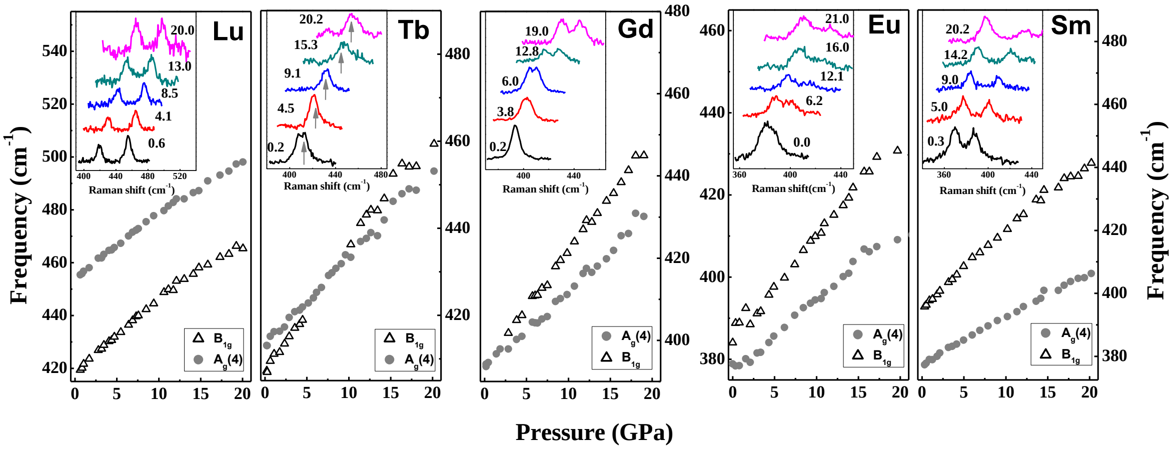

Figure 5.3: Pressure dependence of rotational modes (A$_g$(4), B$_{1g}$(4)) frequencies in *R*CrO$_3$. Insets show the mode profiles at different pressures.

Pressure dependence of the rotational modes A$_g$(4) and B$_{1g}$(4) are plotted in Fig.5.3. As expected the frequencies of these modes increase with increase in pressure. It is necessary to look at the behaviour of A$_g$(4) mode frequency with pressure as it is related to the degree of distortion, since the mode frequency varies linearly with the tilt angle ‘θ’. Hence, the increase of this mode frequency with pressure indicates that the octahedral distortion is increasing with pressure.

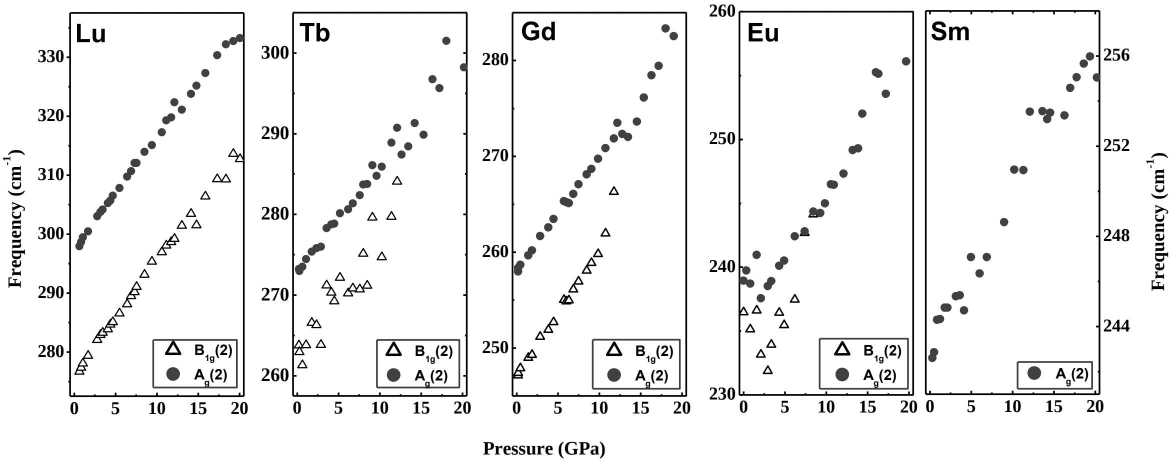

Figure 5.4: Pressure dependence of rotational modes (A$_g$(2), B$_{1g}$(2)) frequencies in *R*CrO$_3$. Insets show the mode profiles at different pressures.

The B$_{1g}$(4) mode can be used for the normalization of the pressure dependence, since it is not dependent on the distortion, in order to reveal the behaviour of soft mode

($A_g(4)$) with pressure. It is interesting to see that the separation between these modes is varying in different rare-earths and one can see a trend as the rare earth ion size (see Fig. 5.3). The separation remains almost constant in *Lu* up to 20 GPa. These modes merge at 5 GPa in *Tb* and a cross-over is seen beyond 10 GPa. The single mode in *Gd* splits into two and the separation of these two modes increases with pressure. Similarly, in the case of *Eu* and *Sm* also the separation increases with pressure. Furthermore, we have found similar changes in $A_g(2)$ mode behaviour with pressure as shown in Fig. 5.4. Here, $B_{1g}(2)$ mode is too weak to be deconvoluted in $SmCrO_3$ and also in $GdCrO_3$, $EuCrO_3$, $TbCrO_3$ at higher pressures.

To understand the behaviour of the rotational modes with pressure, we have calculated the rate of change in $A_g(4)$ and $A_g(2)$ soft mode frequencies with pressure ($\Delta A_g(4)$ and $\Delta A_g(2)$) for different RCrO$_3$. We found that $\Delta A_g(4)$ decreases with ionic radii rare-earth cation: $(2.21)_{Lu} > (2.04)_{Tb} > (1.93)_{Gd} > (1.81)_{Eu} > (1.45)_{Sm}$. Similarly, $\Delta A_g(2)$: $(1.85)_{Lu} > (1.28)_{Tb} > (1.18)_{Gd} > (0.99)_{Eu} > (0.68)_{Sm}$. The trend in $\Delta A_g(4)$, $\Delta A_g(2)$ with the size of *R*-ion, indicates that the rate of increase of distortion with pressure is reducing as we go to larger *R*-ions.

5.3.2 Pressure induced compressions at *R* and Cr-sites:

In order to understand the role of *R*-ion size for the observed behaviour of octahedral distortions in RCrO$_3$ at higher pressure, it is important to study the pressure induced compressions at CrO_6 and RO_{12} sites.[14] We made an attempt to compare the compressibility of CrO_6 and RO_{12} by considering the pressure dependence on the Raman modes $A_g(1)$ and $A_g(7)$. It is known that the compressions at A and B sites in orthorhombic ABO_3 are anisotropic due to the presence of longer and shorter bonds.[14,16] However, the frequencies of $A_g(1)$ and $A_g(7)$ modes depend on the average Cr-O and *R*-O bond lengths and would be sufficient for the qualitative comparison of CrO_6 and RO_{12} compressibility with pressure. The change in these mode frequencies with pressure (ω_p-ω_0) in $LuCrO_3$ and $SmCrO_3$ are shown in Fig. 5.5. The slopes of the linear fits to ω_p-ω_0 vs P for $A_g(1)$ is: $(4.2)_{Lu} < (5.30)_{Tb} < (5.32)_{Gd} < (5.69)_{Eu} < (5.72)_{Sm}$. Similarly, for $A_g(7)$: $(1.39)_{Lu} > (0.79)_{Tb} > (0.62)_{Gd} > (0.48)_{Eu} > (0.31)_{Sm}$. The trend in these slope values is related to the trend in the compression of the bonds at the respective sites. It clearly indicates that the compressibility of CrO_6 is increasing with increase in *R*-ion radii while

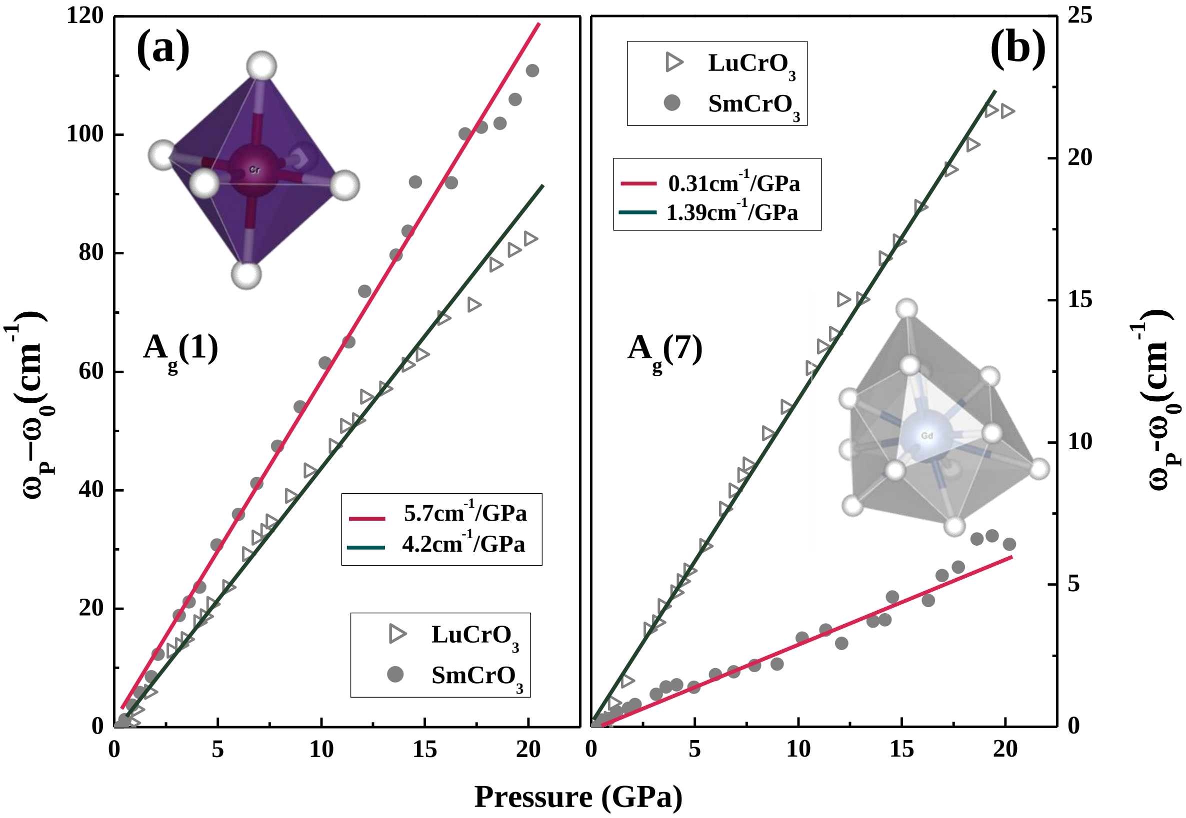

Figure 5.5: Variation in the Cr-O stretching (A$_g$(1)) and *R*-O vibration (A$_g$(7)) mode frequencies with pressure in LuCrO$_3$ and SmCrO$_3$. The solid lines are the linear fits to the data.

the compressibility of *R*O$_{12}$ is decreasing. The reduction in the compression of *R*O$_{12}$ from *Lu* to *Sm* is associated with the decrease in the change of mean bond distance <*R*-O> which is accompanied by the net increase in the change of mean <Cr-O> bond distance. This is one of the reasons for the decrease in degree of inter-octahedral tilting as seen from the trend in A$_g$(2) frequency with pressure.

5.3.3 Predictions:

To know exactly how the rate of change octahedral distortions depend on the *R*-ion radii (r_R^{3+}), we have plotted ΔA$_g$(4) and ΔA$_g$(2) as a function of the r_R^{3+} which is shown in Fig.5.6. A steep decrease in these values below *Gd* has been noticed. A smooth curve as guide to the eye passing through the data points intersects the x-axis around 1.10 Å, where ΔA$_g$(4) and ΔA$_g$(2) =0. We have not used any specific theory or function to fit the data, since we wnated to keep it empirical. This means, for the case of *R*CrO$_3$ with r_R^{3+} is close to the above value, we should not expect any pressure induced changes in the orthorhombic distortion. When r_R^{3+}>1.09 Å, the trend would reverse, namely, distortions decrease with pressure; the perovskites structure will move towards less distorted (more symmetric) phase. The pressure induced structural transition to rhombohedral symmetry observed[18] in LaCrO$_3$ strongly supports our prediction. Also, as mentioned before, in RCrO$_3$, the antiferromagnetic ordering temperature of Cr^{3+} (T_N^{Cr}) increases (100-280K) with increase in rare-earth size from *Lu* to *La* (see Fig 5.1). Since, T_N^{Cr} is a direct outcome of the magnetic exchange integral it would be interesting to see how the pressure induced changes in octahedral tilts can influence T_N^{Cr}. These inferences will be discussed in the next chapter (Chapter 6).

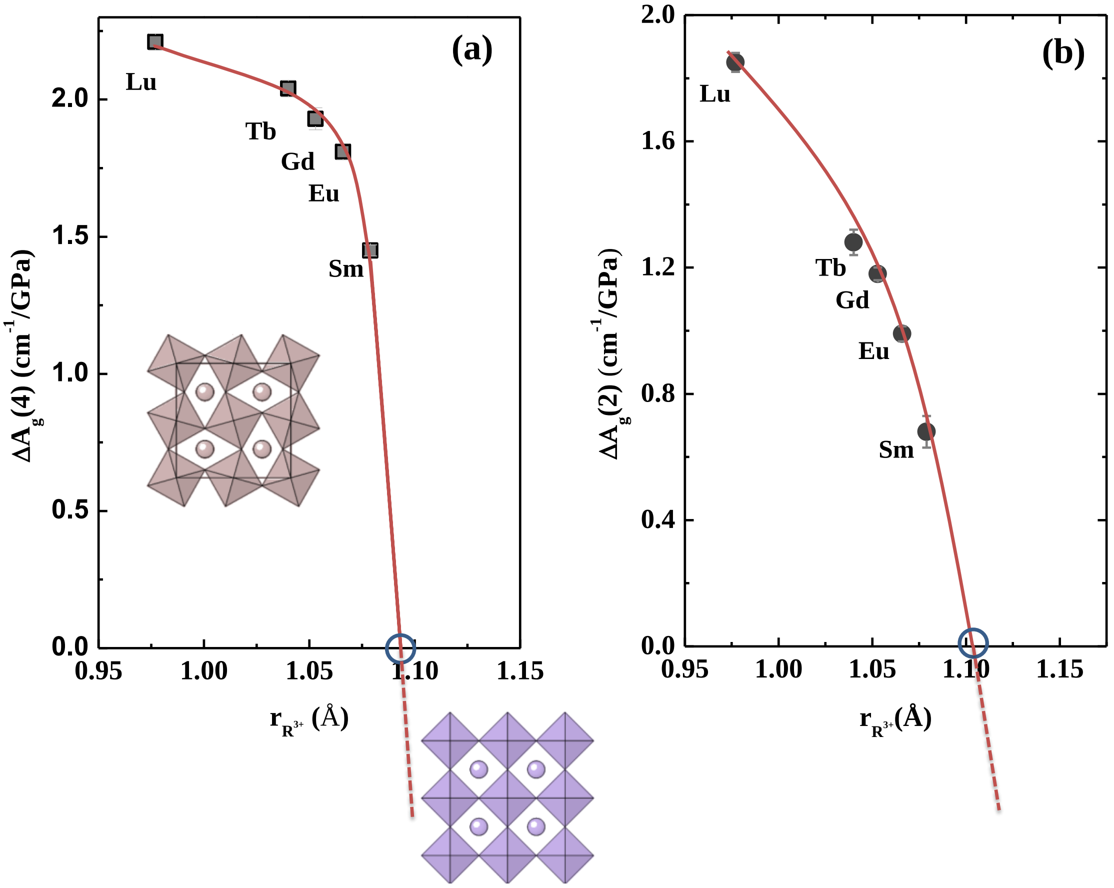

Figure 5.6: Plot of a) $\Delta A_g(4)$ b) $\Delta A_g(2)$ against ionic radii of *R*-ion. Red solid line is the smooth curve drawn through the data points. The red dotted lines are extrapolation of the solid lines. The points where the curves intersect the x-axis ($\Delta A_g(4) = \Delta A_g(2) = 0$) have been encircled.

5.4 Concluding remarks:

In conclusion, we have successfully demonstrated the rare-earth (*R*) size dependence of the pressure evolution of octahedral distortions in orthorhombic chromites

*R*CrO$_3$, for the first time, using Raman scattering. From the pressure dependence of the octahedral rotational modes we found that the octahedral distortions increase with pressure at a rate which reduces with the increase in *R*-ion radii. For a particular *R*-ion radius (~ 1.10 Å), rate of change in distortion will be zero and with increasing the *R*-ion radii further, distortions reduce with pressure. Thus, we could explain why LaCrO$_3$ undergoes a structural transition to a less distorted (more symmetric) phase at higher pressures. A schematic representation of our conclusions is shown Fig.5.7.

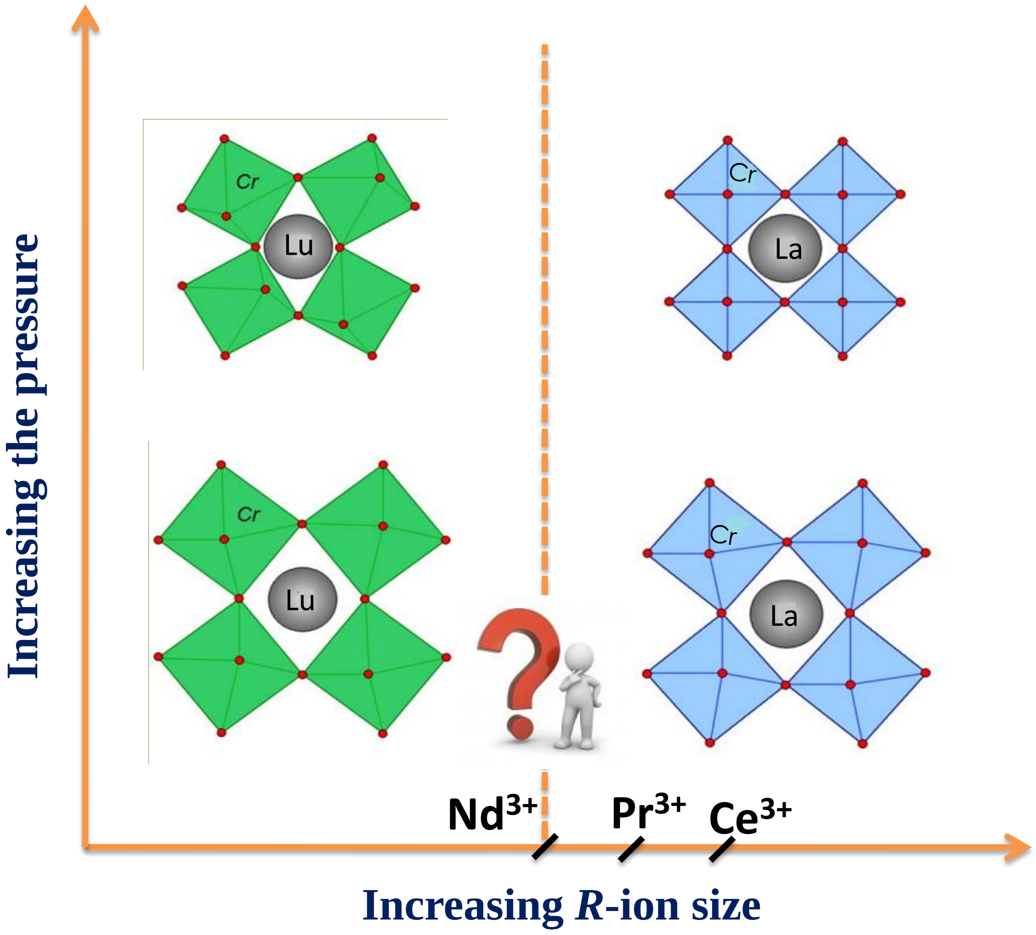

Figure 5.7: Schematic representing the pressure effects on *R*CrO$_3$. The dotted line is corresponding to the critical rare-earth size (Nd^{3+}) above and below which changes in the distortions with pressure will have opposite trend.

Pressure induced changes in distortions in perovskites can be related to octahedral tilt angles at room pressure which decrease linearly with increase in *R*-ion radii.[22] When the distortion is high at room pressure (as in small R-ion case), R-ion is less confined in RO$_{12}$ and with pressure RO$_{12}$ compresses significantly leading to a more distorted structure. Conversely, when the distortion is low at room pressure (as in larger R-ion), R-ion will be strongly confined inside RO$_{12}$ and at higher pressure RO$_{12}$ will be less compressible leading to a less distorted structure. These effects were clearly demonstrated by the pressure dependence of $A_g(1)$ and $A_g(7)$ modes (shown in Fig.5.5).

5.5 Bibliography:

1. M. W. Lufaso and P. M. Woodward, *Acta Cryst. B*, 57, 725. (2001).
2. I. A. Kornev, L. Bellaiche, P. Bouvier, P.-E. Janolin, B. Dkhil, and J. Kreisel, *Phys. Rev. Lett.*, 95, 196804 (2005).
3. M. L. Medarde, *J. Phys. Condens. Matter.*, 9, 1679 (1997).
4. L. T. Tsymbala, Ya. B. Bazaliy, V. N. Derkachenkob, V. I. Kamenev, G. N. Kakazei, F. J. Palomares and P. E. Wigen, *J. Appl. Phys.*, 101, 123919 (2007).
5. T. Goto, T. Kimura, G. Lawes, A. P. Ramirez, and Y. Tokura, *Phys. Rev. Lett.* 92, 257201 (2004).
6. B. B. V. Aken , T. T. M. Palstra, A. Filippetti and N. A. Spaldin, Nature Materials, 3, 164 (2004).
7. T. Kimura, T. Goto, H. Shintani, K. Ishizaka, T. Arima and Y. Tokura, *Nature*, 426, 55 (2003).
8. J. S. Zhou, J. B. Goodenough, J. M. Gallardo-Amores, E. Moran, M. A. Alario-Franco, and R. Caudillo, *Phys. Rev. B*, 74, 014422 (2006)
9. N. Russo *et al*, *Ind. Eng. Chem. Res.*, 46, 4226 (2007).
10. J. Beckers and G. Rothenberg, *Chem. Phys. Chem.*, 6, 223 (2005).
11. B. Rajeswaran, D. I. Khomskii, A. Sundaresan and C. N. R. Rao, *Phys. Rev. B*, 86, 214409 (2012).
12. V. S. Bhadram, B. Rajeswaran, A. Sundaresan and C. Narayana, Euro. Phys. Lett. 101, 17008 (2013).
13. J. Zhao, N. L. Ross and R. J. Angel, *Acta Crystallogr. B*, 60, 263 (2004).
14. N. L. Ross, J. Zhao and R. J. Angel, *J. Solid. Stat. chem.*, 177, 3768 (2004).
15. R. J. Angel, J. Zhao, and N. L. Ross, *Phys. Rev. Lett.*, 95, 025503 (2005).
16. J. Zhao, N. L. Ross and R. J. Angel, *J. Phys. Condens. Matter*, 16, 8763 (2004).
17. M. Ardit, G. Cruciani, M. Dondi, M. Merlini and P. Bouvier, *Phys. Rev. B*, 82, 064109 (2010).

18. J.-S. Zhou, J. A. Alonso,A. Muonz, M. T. Fernández-Díaz, and J. B. Goodenough, *Phys. Rev. Lett.*, 106, 057201 (2011).
19. Y. Zhao, D. Weidner, J. B. Parise and D. E. Cox, *Phys. Earth. Planet. Inter.*, 76, 1 (1993).
20. M. N. Iliev, A. P. Litvinchuk, V. G. Hadjiev, Y. Q. Wang,J. Cmaidalka, R. L. Meng, Y. Y. Sun, N. Kolev, and M. V. Abrashev, *Phys. Rev. B*, 74 , 214301 (2006).
21. M. N. Iliev, M. V. Abrashev, H. G. Lee, V. N. Popov, Y. Y. Sun, C. Thomsen, R. L. Meng, and C. W. Chu, *Phys. Rev. B*, 57 , 2872 (1998).
22. M. C. Weber, J. Kreisel, P. A. Thomas, M. Newton, K. Sardar and R. I. Walton, *Phys. Rev. B*, 85 , 054303 (2012).

Chapter 6

Structural Aspects of RCrO$_3$ (R= Gd, Eu, Sm) as a Function of Pressure

The author's contribution in this chapter is to perform high pressure x-ray diffraction experiments and to analyze the data. Samples have been synthesized by Prof. Sundaresan's group at JNCASR. Profile matching of the x-ray diffraction patterns was carried out by Dr. Diptikanta Swain, JNCASR.

6.1 Introduction:

In the previous chapter, we have discussed the pressure induced changes in the octahedral bond lengths and tilt angles in RCrO$_3$ (R= Lu, Tb, Gd, Eu, Sm) through Raman mode analysis. In this chapter, we are discussing the effect of pressure on the structural aspects of RCrO$_3$ probed by synchrotron powder x-ray diffraction (XRD). Since such experiments are best performed on a synchrotron source, especially to see subtle variations in the octohedral tilts etc, we have used ELETTRA high pressure beamline to do these experiments. Due to the limited availability of the beamtime we could perform measurements only on three systems namely, GdCrO$_3$, EuCrO$_3$ and SmCrO$_3$. We are in the process of doing others in the series, but from our learning from the Chapter 5, we believe that it is at present sufficient to look at these three perovskites for getting a general trend.

In the past, many studies[1-7] have been focussed on the structural changes in perovskites lattice due to external pressure, probed by synchrotron XRD. Particularly, in YTiO$_3$, distinct changes in the distortions of TiO$_6$ octahedra were observed around 10 GPa from the analysis of pressure dependence of changes in Ti-O bond lengths.[6] This was explained to be rooted by the spatial re-orientation of the occupied Ti orbitals. In another recent report[7] structural relaxation along YAlO$_3$-YCrO$_3$ join has been addressed by a combined synchrotron XRD and electron absorption spectroscopy (EAS). The structural relaxation around Cr^{3+} is found to be the lowest in perovskites compared to garnet, spinel and corundum structures. These reports exemplify the importance of XRD in understanding the structural aspects and their effect on the electronic properties of perovskites oxides.

To understand the pressure induced changes in the perovskite distortions, particularly the octahedral tilts, one can calculate the tilt angles directly from the lattice parameters.[8] The quantification of the distortions can also be done by measuring the cell distortion factor,[9] which estimates the cell distortion by comparing the lattice parameters with pseudo cubic cell parameters. Since, the compression mechanism in perovskites is largely related to pressure-induced distortions in the AO$_{12}$ and BO$_6$ which influences the tilt angles, it is critical that individual compressions at R and Cr-sites with respect to pressure to be addressed.

Furthermore, Cr^{3+}-O-Cr^{3+} exchange interactions are sensitive to the octahedral tilt angles[10] and thereby play a crucial role in the pressure induced changes in the magnetic transition temperature (T_N^{Cr}), which would regulate the magnetic properties of these materials. Although there are a good amount of work done in this line in the case of rare-earth nickelates ($RNiO_3$),[11] ferrites ($RFeO_3$),[12] and managnites ($RMnO_3$),[13] no such studies exist in the case of $RCrO_3$ to the best of our knowledge. Thus, the aim of the present studies is of two folds: i) to see the effect of rare-earth size on the pressure induced changes in the octahedral tilts ii) to be able to correlate these changes in the octahedral tilts to the magnetic properties of $RCrO_3$ in the temperature and pressure space.

6.2 Experimental details:

The pellets of these powder samples ($GdCrO_3$, $EuCrO_3$ and $SmCrO_3$) were crushed and pieces of required size were selected for high pressure studies. A membrane type high pressure diamond anvil cell (DAC) from BETSA, France has been used for the high pressure experiments. Silicone oil has been used inside DAC for hydrostatic conditions. Gold powder has been used for in-situ pressure measurements. Structural studies of the samples under pressure were done using XRD beamline (λ=0.7Å) at Elettra synchrotron, Trieste. The details of the experimental setup and procedure are available in Chapter 2. Diffraction patterns were recorded on image plate and the collected patterns were integrated using FIT2D [14] program to get intensity vs 2θ plots. As obtained patterns were profile matched to *Pbnm* setting using Le Bail fit in Fullprof programme.

6.3 Results and discussion:

Fig.6.1 shows the XRD plots of $GdCrO_3$, $EuCrO_3$ and $SmCrO_3$ at two different pressures, one at ambient and the other at higher pressure. The corresponding Le Bail fits have also been plotted which suggest a good agreement between the calculated and observed patterns. The corresponding lattice parameters are given in Table 6.1. The careful inspection of the plots in Fig. 6.1 shows a relative broadening of the peaks at higher pressure which is due to the quasi hydrostatic nature of the pressure transmitting medium (silicone oil) used in the experiments.

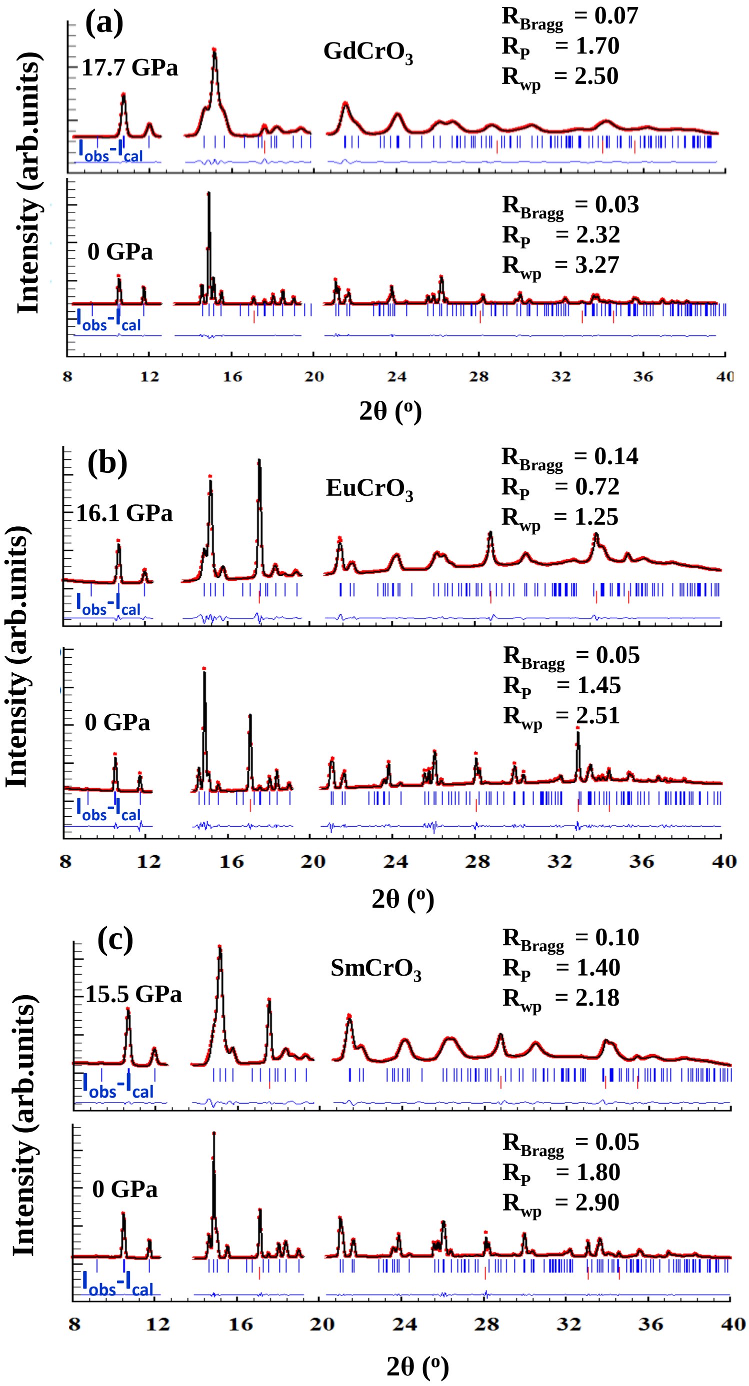

Figure 6.1: XRD pattern of a) GdCrO$_3$ b) EuCrO$_3$ c) SmCrO$_3$ at ambient as well as at higher pressures. The experimental data are indicated by red dots, the calculated pattern (using Le Bail fit) is the black solid line, where as the lower curve is the weighted difference between the observed and calculated pattern.

6.3.1 Pressure dependence of lattice parameters:

The pressure dependence of the unit cell volume as well as lattice parameters in $R\mathrm{CrO}_3$ is plotted in Fig. 6.2. There is no indication of any phase transition observed up to the respective highest pressures achieved. The volume reduction is about 6% in all the three systems studied. The P-V data was fitted with a 2nd order Birch-Murnagham equation of state (EOS), [15] where we have taken the first derivative of bulk modulus as 4:

$$P = \frac{3B_0}{2}\left[\left(\frac{V_0}{V}\right)^{\frac{7}{3}} - \left(\frac{V_0}{V}\right)^{\frac{5}{3}}\right] \tag{6.1}$$

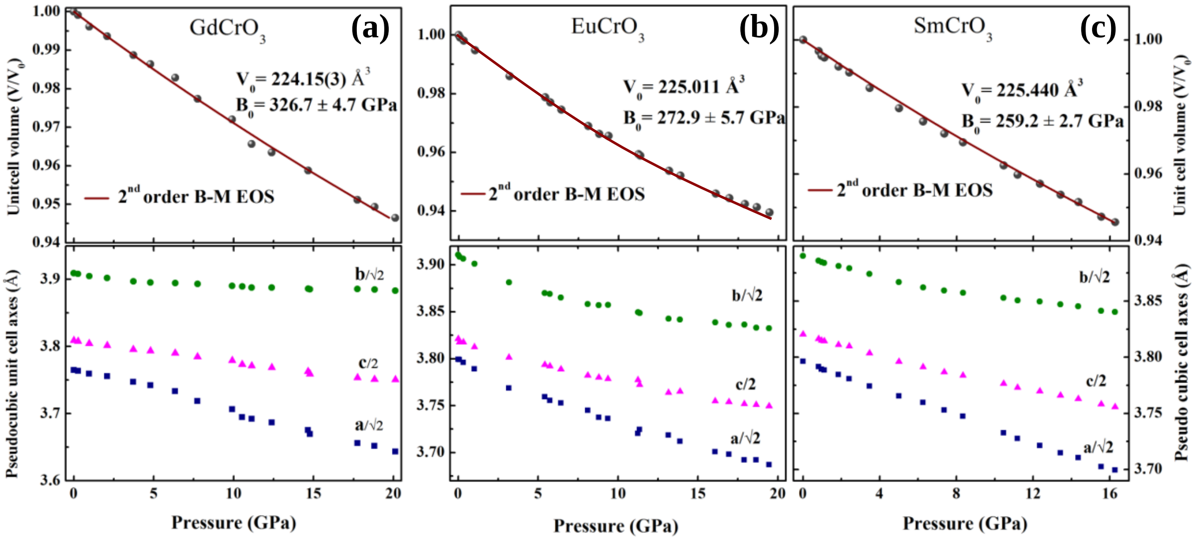

Figure 6.2: Pressure dependence of unitcell volume and lattice parameters of a) GdCrO_3 b) EuCrO_3 c) SmCrO_3.

The calculated volumes at ambient pressures are in close agreement with the ones obtained from other experiments. The volumetric bulk modulii (B_0) as obtained from the fits are 326.7±4.7 272.9±5.7 and 259.2±2.7 GPa for GdCrO_3, EuCrO_3 and SmCrO_3 respectively (shown in Table 6.1). The decrease in the bulk modulus with the increase in the rare-earth ionic radii ($r_{R^{3+}}$) can be assigned to the increase in the octahedral compressibility as known from our previous Raman analysis presented in Chapter 5. On the basis of the experimental results of anti-ferromagnetic transition metal oxides, Bloch[16] has put forward a phenomenological rule: $\frac{dT_N}{dP} = 3.3T_N\kappa$, where κ is the compressibility. In general, for perovskites structure, the magnetic transition temperature which depends upon the strength of the exchange interactions (*J*) is directly related to the octahedral tilt angles and bond length, and it is not related to its cell volume. Most of the magnetic perovskite oxides obey the Bloch's rule. Hence, using $\kappa = B_0^{-1}$ from our x-ray diffraction work, we have found out $\frac{dT_N}{dP}$ follows a trend, namely: $(1.561)_{Gd} < (2.543)_{Eu} < (2.691)_{Sm}$ °K/GPa.

Table 6.1: Lattice parameters (a, b and c) of *R*CrO$_3$ obtained from profile matching. Unit cell volume at ambient (V$_0$) and B$_0$ are obtained from the fit of the P-V data with equation of state (EOS) mentioned in the text.

Sample	**a (Å)**	**b (Å)**	**c (Å)**	**V$_0$(Å^3)**	**B$_0$ (GPa)**
GdCrO$_3$	5.3238(1)	5.5279(1)	7.6184(1)	224.170(4)	326.7 ± 4.7
EuCrO$_3$	5.3714(2)	5.5255(2)	7.6372(3)	225.502(8)	272.9 ± 5.7
SmCrO$_3$	5.3698(3)	5.5143(1)	7.6512(1)	226.463(6)	259.2 ± 2.7

Furthermore, to visualize the compressions along the cell axes, we have plotted ratio of the unit cell parameters as a function of pressure with the ambient unit cell values in Fig. 6.3. It is clear that the compressions are anisotropic along the cell axis in all the three systems (especially, b and c), but this anisotropy reduces as we go the larger rare-earth. This suggests that SmCrO$_3$ is less distorted compare to that of GdCrO$_3$ at higher pressures.

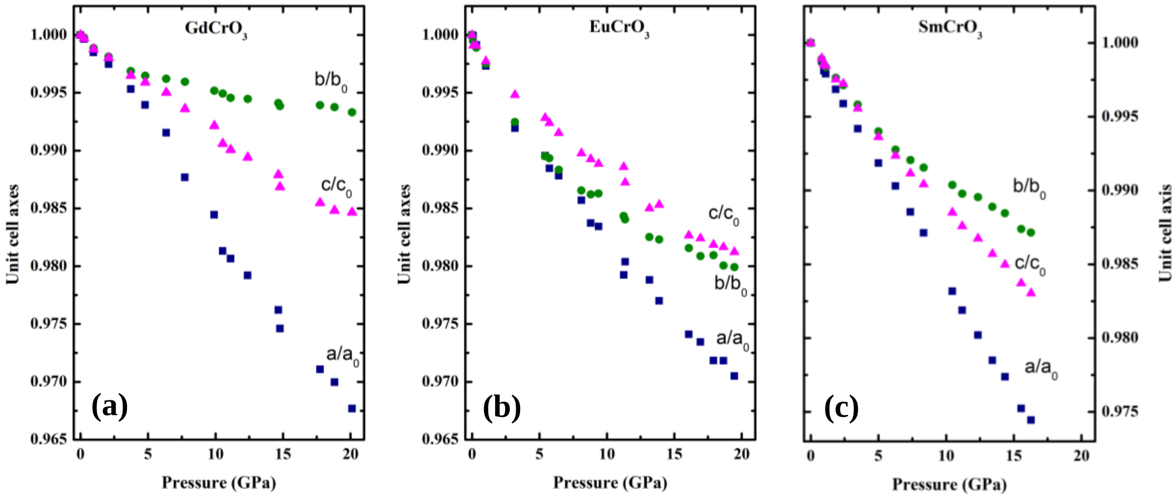

Figure 6.3: Pressure dependence of unit cell parameters of a) GdCrO$_3$ b) EuCrO$_3$ c) SmCrO$_3$ showing the anisotropy of compressions along *a*, *b*, *c*-axis.

6.3.2 Pressure effects on the octahedral tilt angles:

For a better comparison of the pressure effects on the $GdCrO_3$, $EuCrO_3$ and $SmCrO_3$, we have calculated the octahedral tilt angles "θ" and "φ" from the lattice parameters using the following known relations, [8]

$$\theta = \cos^{-1}\left({}^{a}/_{b}\right) \tag{6.2}$$

$$\varphi = \cos^{-1}\left({}^{\sqrt{2}a}/_{c}\right) \tag{6.3}$$

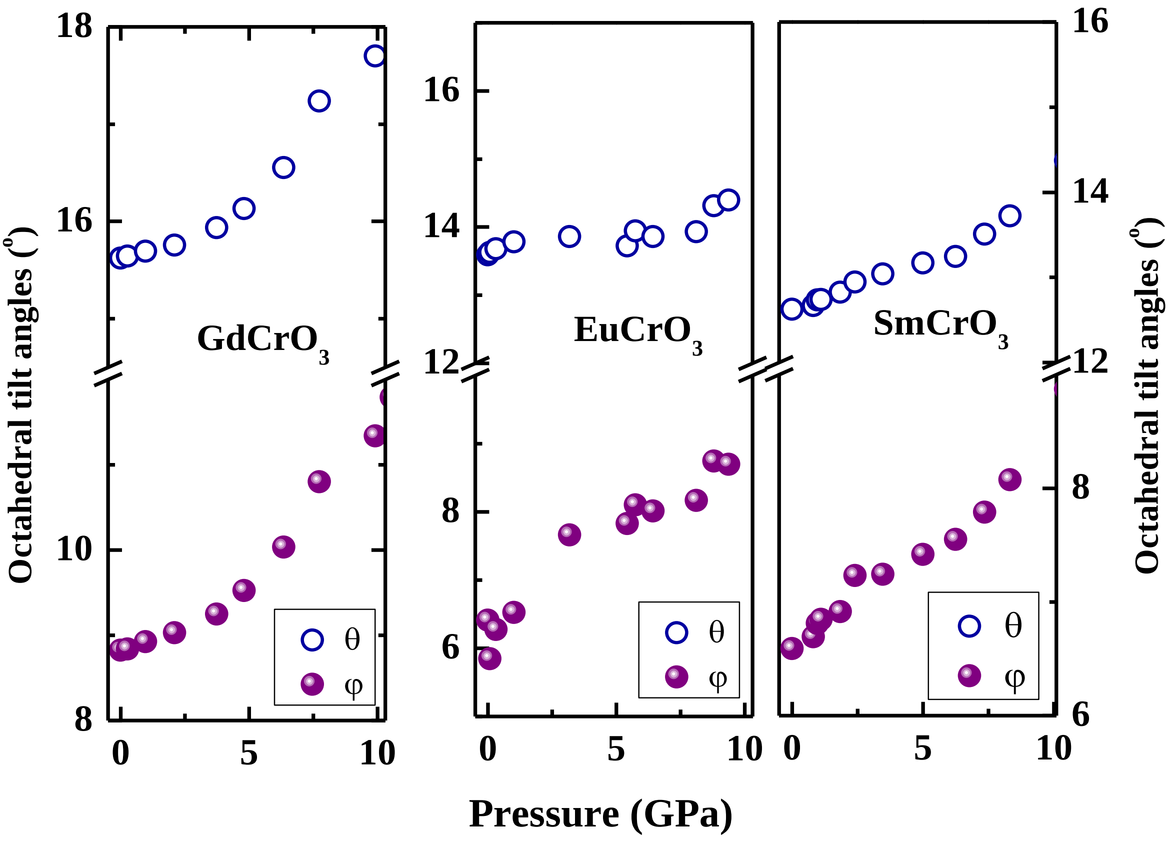

Figure 6.4: Pressure dependence of octahedral tilt angles 'θ', 'φ' calculated from the lattice parameters in $RCrO_3$ (R= Gd, Eu, Sm).

The above relations were obtained considering that the CrO_6 octahedra are regular throughout the perovskites lattice. The calculated tilt angles are plotted against pressure in Fig. 6.4. Tilt angles increase with pressure in all the three systems indicating the increase in octahedral distortion with pressure. But the rate of change in θ is 0.23° /GPa in $GdCrO_3$

and it is around 0.1 in EuCrO$_3$ and SmCrO$_3$. Similarly, the rate of change in tilt angle φ with pressure GdCrO$_3$ is 0.4^o/GPa and the same is around 0.2^o/GPa in EuCrO$_3$ and SmCrO$_3$. These values suggest that the rate of increase in distortion reducing as we move from GdCrO$_3$ to SmCrO$_3$.

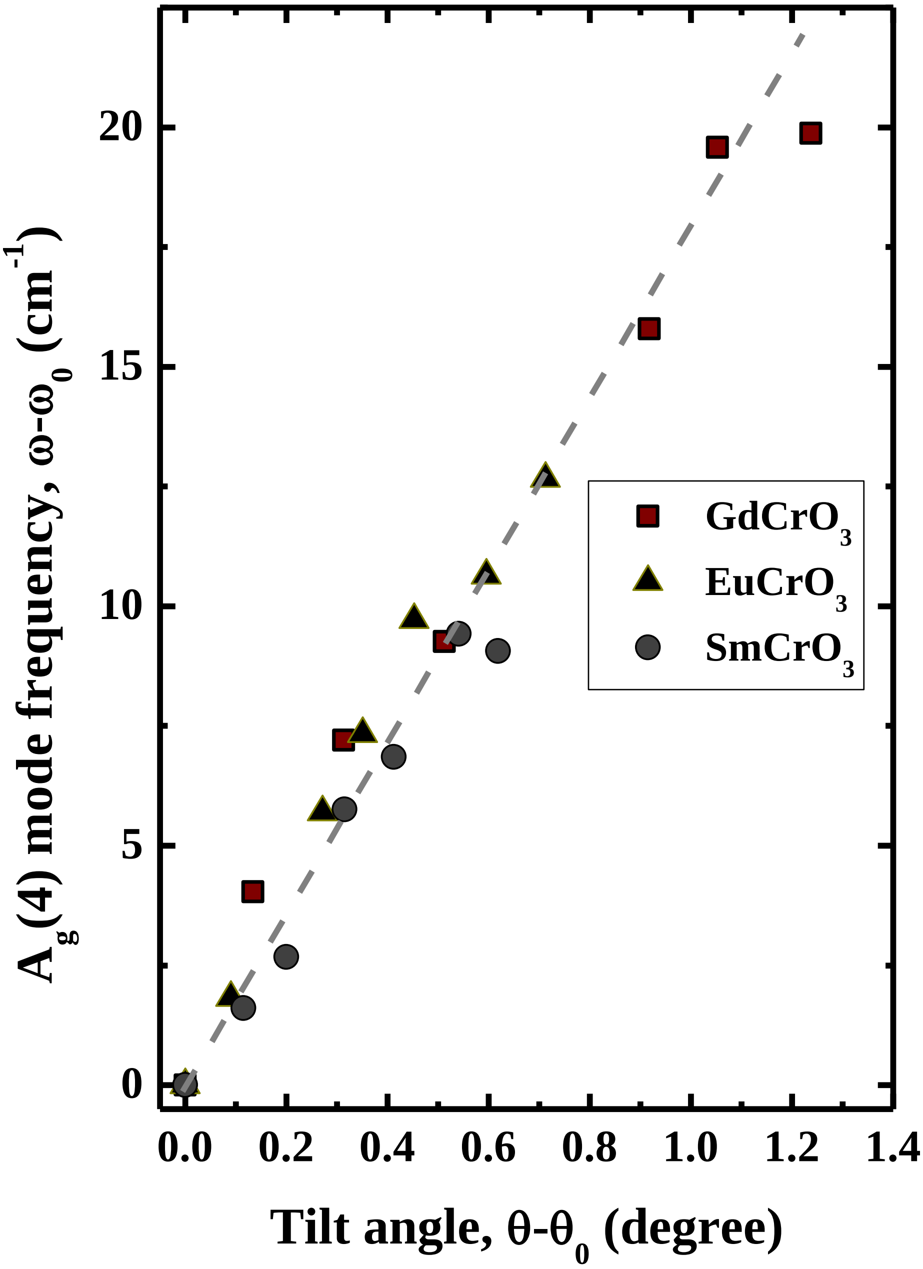

Figure 6.5: Plot of the change in A$_g$(4) mode frequency vs the change in tilt angle ‘θ’. Dotted line is the linear fit to the data. A$_g$(4) mode frequencies have been taken from the Raman data presented in Chapter 5.

The behaviour of octahedral tilts can be related to the corresponding soft mode frequencies. For instance, change in the soft mode $A_g(4)$ frequency vs tilt angle 'θ' with respect to pressure has been shown in Fig.6.5. It can be seen that soft mode frequency scales linearly with tilt angle with a slope of around 16.1 cm^{-1}/degree. This slope value is different from the one that is seen in $RCrO_3$[17] and $RMnO_3$[18] with respect to different *R*-ions suggesting that the effect of external pressure on soft mode behaviour is different from that induced by the chemical pressure due to cation substitution. Since pressure effects are far more fine tuned than the "chemical pressure" applied due to *R*-ion substitution, this experiment gives a much better handle on this value.

6.3.3 Compressibility at Cr-site:

Similarly, as in the case of the tilt angles, one can calculate the average Cr-O bond length $\langle Cr\text{-}O\rangle$ by neglecting the self distortion in the octahedra[9] using the following relation:

$$\langle Cr - O\rangle = \frac{bc}{4a} \tag{6.4}$$

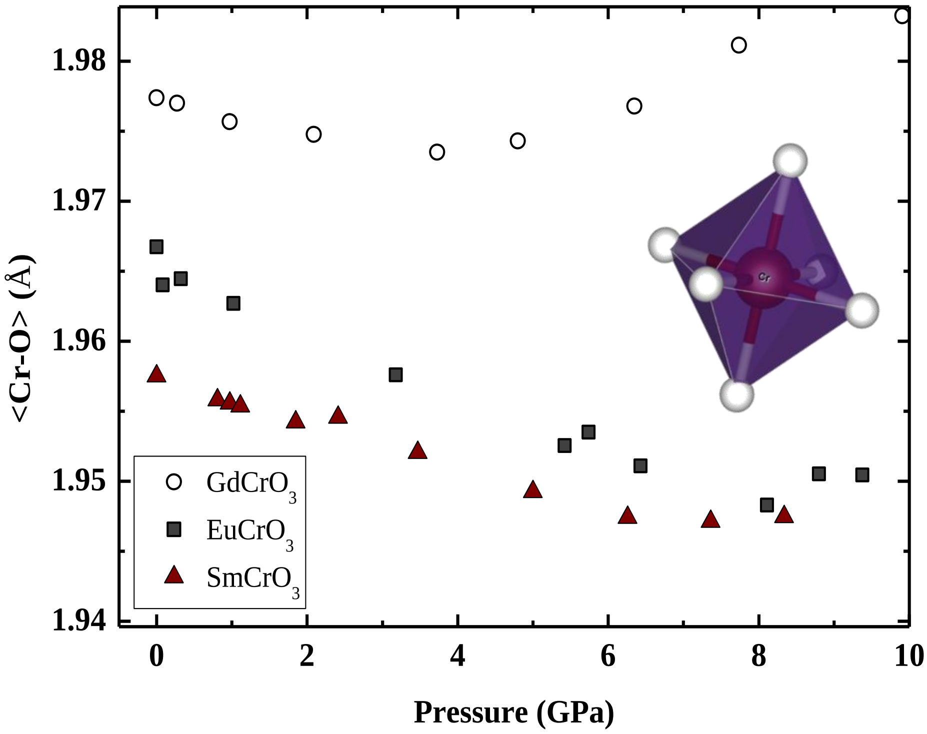

Figure 6.6: Average Cr-O bond length (⟨Cr-O⟩)vs pressure in $RCrO_3$ (*R*= Gd, Eu, Sm).

The calculated ⟨*Cr-O*⟩ values are plotted against pressure as shown in Fig. 6.6. In general, one expects that ⟨*Cr-O*⟩ reduces with pressure as is seen in the case of *Eu* and *Sm* but it is found to be more or less constant in case of *Gd* throughout the pressure range. This is a clear indication that CrO$_6$ octahedra are less compressible in GdCrO$_3$ compared to EuCrO$_3$ and SmCrO$_3$, which was observed from the Raman mode analysis discussed in the last chapter. In general, the compressions at *Cr* and *R* sites together determine the tilt angles. When the compressions at *R*-site are more than that of the Cr-site, tilts decrease with pressure and vice versa. The trend in the ⟨*Cr-O*⟩ shown in Fig.6.6 indicates that at a higher pressure, the tilts in EuCrO$_3$ and SmCrO$_3$ would be lesser than in GdCrO$_3$.

6.3.4 Pressure dependence on cell distortion factor:

To provide more concrete evidence for the above arguments we have calculated the cell distortion factor (d) which is a measure of the distortion in the prerovskite framework with respect to its pseudocubic counterpart. [10]

$$d = \frac{\left[\left(\frac{a}{\sqrt{2}}-a_p\right)^2+\left(\frac{b}{\sqrt{2}}-a_p\right)^2+\left(\frac{c}{2}-a_p\right)^2\right]}{3a_p^2\times10^4} \qquad (6.5)$$

where, $a_p = \frac{\left[\frac{a}{\sqrt{2}}+\frac{b}{\sqrt{2}}+\frac{c}{2}\right]}{3}$ is the pseudocubic subcell parameters. For an ideal cubic perovskites, $a_p = 0$. As given in Fig. 6.7, the variation of d/d$_0$ with pressure shows a linear increase with pressure indicating the increase in the cell distortion with pressure. It is evident from the slopes of the linear relationships, Δd that the rate of increase of distortion with pressure is different for different rare-earths. It is to be noted that Δd for the case of *Y* shows a lower value than our present *Gd*, *Eu* and *Sm* which could be related to the electronic configuration of Y^{3+} which is significantly different from the rare-earth ions. As seen in YBO$_3$ with B-ions having distinct electronic configuration, the electronic configuration of *R*-ion can strongly influence the compressions at *R*-site and in turn the octahedral distortions.

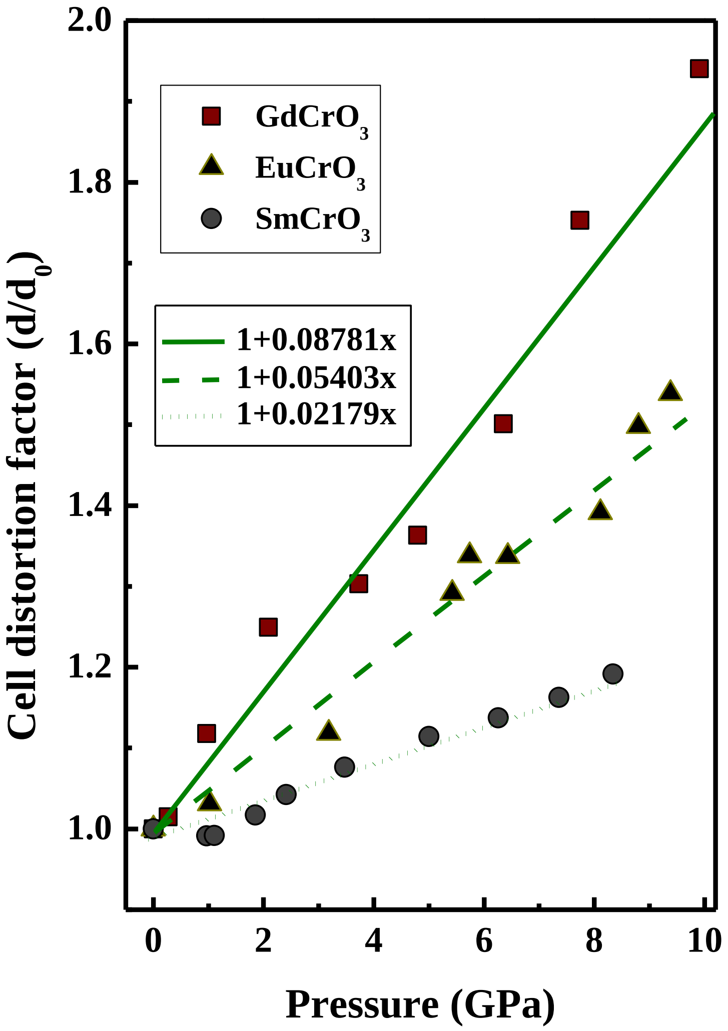

Figure 6.7: Cell distortion factor (d) vs pressure in $RCrO_3$ (R= Gd, Eu, Sm).

6.3.5 Predictions:

We have also plotted the slopes Δd with respect to the r_R^{3+} in Fig. 6.8. It is clear that these slope values decrease linearly with the increase in r_R^{3+}. From the linear curve fit to the data points, we found Δd=0 for $r_R^{3+} \approx 1.09$ Å which means, the distortion will not change with pressure for the corresponding chromite, beyond which there would be reversal of the trend. This critical value of critical r_R^{3+} is in close agreement with the one obtained from our Raman studies in Chapter 5. We can now predict that the Δd decreases and acquires a negative values for $RCrO_3$ with $r_R^{3+}>1.09$ Å (dotted line in Fig. 6.8) which means, for these chromites octahedral distortions reduce with pressure and lead to a more ordered structure. This is once again corroborated with the pressure induced structural transition to rhombohedral (*R-3c*) symmetry in $LaCrO_3$ reported earlier. [19]

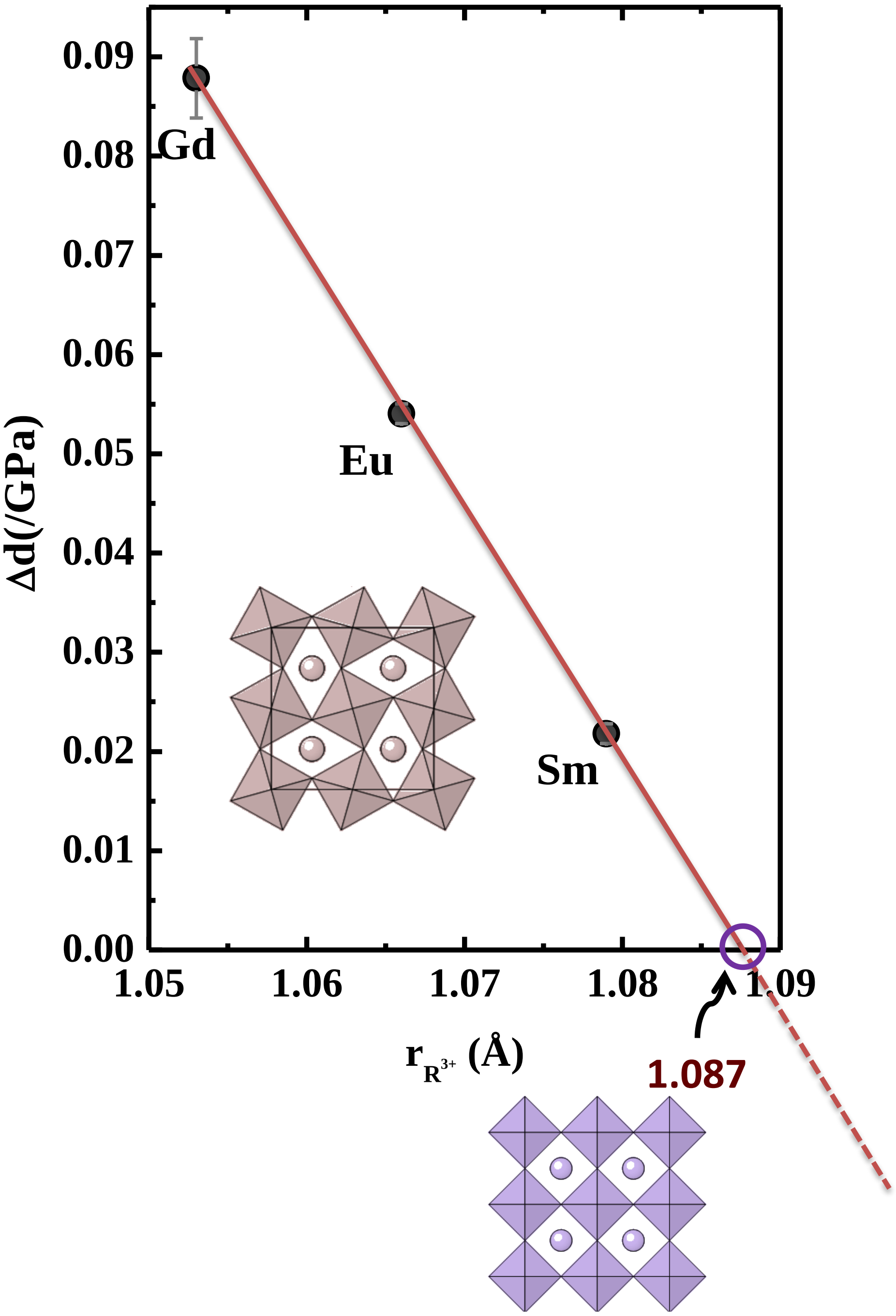

Figure 6.8: Variation of rate of change in cell distortion factor (Δd) with respect to pressure. Red solid line is the linear fit to the data points. Red dotted line is the extrapolation of this linear fit.

It is known that in anti-ferromagnetic *R*CrO$_3$, the relation between tilt angle and T_N^{Cr} is:[10]

$$T_N^{Cr} \propto {cos^4(\alpha)}/{l^7} \tag{6.6}$$

Here $\alpha = \frac{\theta+2\varphi}{2}$ and $l = \langle Cr - O \rangle$. Then the change in T_N^{Cr} with respect to pressure can be written as

$$\frac{dT_N^{Cr}}{dP} = -T_N\left[\frac{7}{l}\frac{dl}{dP} + \left(2\tan\left(\frac{\theta+2\varphi}{2}\right)\left(\frac{d\theta}{dP} + 2\frac{d\varphi}{dP}\right)\right)\right] \tag{6.7}$$

Unlike Bloch's rule, Eq. 6.7 shows explicitly, the contribution of the tilt angles to the quantity $\frac{dT_N^{Cr}}{dP}$. Due to octahedral compressions under pressure, $\frac{dl}{dP}$ is always a negative quantity. In addition, it is known from Bloch's rule that $\frac{dT_N^{Cr}}{dP}$ is always a positive quantity.

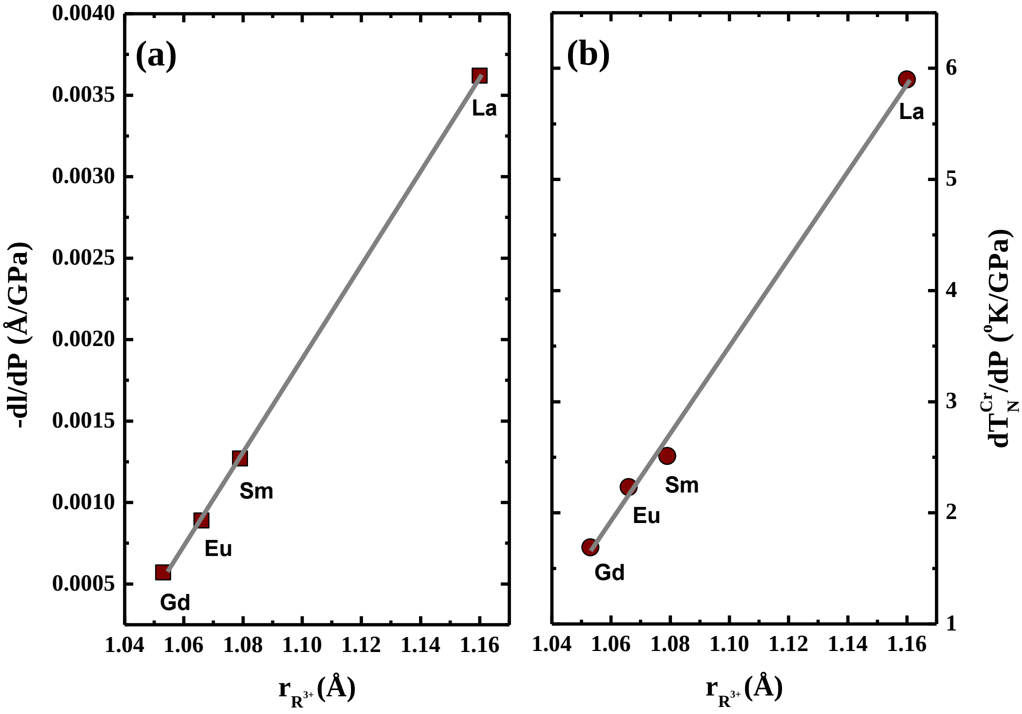

Figure 6.9: Rare-earth ionic radii dependent variation in (a) rate of change in <Cr-O> with pressure. (b) rate of change in T_N^{Cr} with pressure calculated using Bloch' rule. The quantities $\frac{dl}{dP}$ and $\frac{dT_N^{Cr}}{dP}$ of LaCrO$_3$ have been calculated from the structural information available in Ref. 19.

As seen from the Raman results in Chapter 5 (for instance, see Fig. 5.6, in Chapter 5) $\frac{d\theta}{dP}$ and $\frac{d\varphi}{dP}$ will possess a non-linear relation with r_R^{3+} below its critical value i.e. $r_R^{3+} \approx 1.09$ Å. Furthermore, it is expected that $\frac{d\theta}{dP}$ and $\frac{d\varphi}{dP}$ will change sign above $r_R^{3+} \approx 1.09$ Å. Thus, one can expect from Eq.6.7, that these changes in $\frac{d\theta}{dP}$ and $\frac{d\varphi}{dP}$ with r_R^{3+} would reflect in $\frac{dT_N^{Cr}}{dP}$. However, as shown in Fig. 6.9, $\frac{dT_N^{Cr}}{dP}$ scales linearly with r_R^{3+} similar as $\frac{dl}{dP}$. This clearly indicates that unlike the case of chemical pressure (change in *R*-ion radii) where change in T_N^{Cr} is mainly due to change in octahedral tilts,[10,20] in the case of external pressure, compressions at Cr-O play dominating role over octahedral tilts in pressure dependent change in T_N^{Cr}.

6.4 Concluding remarks:

In conclusion, the synchrotron x-ray diffraction results clearly suggest that the tilt distortions increase with pressure in *R*CrO$_3$ (*R*= Gd, Eu, Sm) but the rate of increase in these distortions reduce with increase in *R*-ion radii. From the behaviour of cell distortion factor with pressure in *R*CrO$_3$, we predict a critical r_R^{3+} above which distortion decrease with pressure in *R*CrO$_3$. These results strongly support the observations from the Raman mode analysis presented in Chapter 5. Furthermore, having the knowledge of the pressure dependent changes in tilt angles for different r_R^{3+}, we tried to understand the rare-earth size dependency of $\frac{dT_N^{Cr}}{dP}$ which involves an explicit relation between octahedral bond lengths (⟨Cr-O⟩), tilt angles and T_N^{Cr}. We found that ⟨Cr-O⟩ plays a dominant role over octahedral tilts in pressure dependent change in T_N^{Cr}. Also, the spin configuration at low temperatures in *R*CrO$_3$ strongly depends upon the magnetic R^{3+}-Cr^{3+} exchange interactions.[21] The latter is found to be responsible for the magneto-dielectric behaviour seen in *R*CrO$_3$ with magnetic R-ion.[22] We would expect that the increase in the octahedral distortions would enhance the *R*-Cr interactions and vice versa. In view of this, it would be interesting to investigate the pressure effect on the aforementioned properties as a function of R-ion radii and temperature.

6.5 Bibliography:

1. J. Zhao, N. L. Ross and R. J. Angel, *Acta Crystallogr. B*, 60, 263 (2004).
2. N. L. Ross, J. Zhao and R. J. Angel, *J. Solid. Stat. chem.*, 177, 3768 (2004).
3. R. J. Angel, J. Zhao, and N. L. Ross, *Phys. Rev. Lett.* 95, 025503 (2005).

4. J. Zhao, N. L. Ross and R. J. Angel, *J. Phys. Condens. Matter*, 16, 8763 (2004).
5. M. Ardit, G. Cruciani, M. Dondi, M. Merlini and P. Bouvier, *Phys. Rev. B*, 82, 064109 (2010).
6. I. Loa, X. Wang, K. Syassen, H. Roth, T. Lorenz, M. Hanfland and Y- L. Mathis, *J. Phys. Condens. Matter*, 19, 406223 (2007).
7. G. Cruciani, M. Ardit, M. Dondi, F. Matteucci, M. Blosi, M. C. Dalconi, and S. Albonetti, *J. Phys. Chem. A*, 113, 13772 (2009).
8. Y. Zhao, D. Weidner, J. B. Parise and D. E. Cox, *Phys. Earth. Planet. Inter.*, 76, 1 (1993).
9. S. Sasaki, C. T. Prewitt and R. C. Liebermann, *Am. Miner.*, 68, 1189 (1983).
10. J.-S. Zhou, J. A. Alonso, V. Pomjakushin, J. B. Goodenough, Y. Ren, J.-Q. Yan, and J.-G. Cheng, *Phys. Rev. B* 81, 214115 (2010).
11. J.-S. Zhou, J. B. Goodenough, and B. Darbrowski, *Phys. Rev. Lett.*, 95, 127204 (2005).
12. D. Treves, M. Eibschutz and P.Coppens, *Phys. Lett.*, 18, 216 (1966).
13. J.-S. Zhou, and J. B. Goodenough, *Phys. Rev. Lett.*, 89, 087201 (2002).
14. A. Hammersley ESRF Internal Report; Fit 2D V.5 *Reference Manual EXP/AH/95-01*(1995).
15. F. Birch, *Phys. Rev.*, 71, 809 (1947).
16. D. Bloch, *J. Phys. Chem. Solids*, 27, 881 (1965).
17. M. C. Weber, J. Kreisel, P. A. Thomas, M. Newton, K. Sardar, and R. I. Walton, *Phys. Rev. B*, 85, 054303 (2012).
18. M. N. Iliev, M. V. Abrashev, J. Laverdiére, S. Jandl, M. M. Gospodinov, Y. Q. Wang, and Y. Y. Sun, *Phys. Rev. B*, 73, 064302 (2006).
19. J.-S. Zhou, J. A. Alonso,A. Muon˜ z, M. T. Fernández-Díaz, and J. B. Goodenough, *Phys. Rev. Lett.*, 106, 057201 (2011).
20. H. J. Zhao, W. Ren, X. M. Chen, and L. Bellaiche, *J. Phys. Cond. Matter*, 25, 385604 (2013).
21. T. Yamaguchi, and K. Tsushima, *Phys. Rev. B*, 8, 5187 (1973).
22. B. Rajeswaran, D. I. Khomskii, A. Sundaresan and C. N. R. Rao, *Phys. Rev. B*, 86, 214409 (2012).

Chapter 7

Summery and Outlook

The present thesis discusses the importance of Raman scattering as a tool to investigate the structural distortions and thereby understanding the physical properties of the some of the rare-earth based perovskite oxides as a function of temperature and pressure. The summery of the important results presented in this thesis is highlighted below.

The presence of two distinct ferromagnetic ground states has been evidenced in LMCO through spin-phonon coupling effects seen in temperature dependence of Raman mode parameters. This behaviour is retained even in high quality single crystals of LMCO suggesting that the presence of two magnetic ground states is an intrinsic property of LMCO. The microscopic origin of difference in T_C values of LMCO has been qualitatively explained by careful analysis of the distortion dependent Raman modes. This suggests that the two LMCO phases are having difference in octahedral distortions originated from the disorder at Mn/Co site which directly influence the exchange energy and thereby T_C. Developing synthetic strategies to synthesize samples with perfect Mn/Co ordering would be a good future direction which would result in LMCO system with single magnetic phase.

The effect of spin-phonon coupling on Raman mode parameters has been used to investigate the intriguing multiferroic property in rare-earth chromites (RCrO$_3$). Here spin-phonon coupling was observed below T_N^{Cr} (Cr-ordering temperature) only in the case of magnetic rare-earth ions (i.e, *Gd*, *Sm*) in analogues to the ferroelectric property seen in these materials. The present study would lead to two important directions in this class of systems. 1) To establish a theoretical framework to understand the correlation between spin-phonon coupling and multiferroicity in oxides. 2) To perform model calculations of spin ordering effects on phonon lifetimes. The present results would serve as a benchmark to validate these calculations.

The pressure dependence of octahedral distortions in RCrO$_3$ and their relation with the transition temperature T_N^{Cr} has been understood for the first time using Raman scattering. Our Raman results suggest that octahedral distortions increase with pressure at a rate which reduces with the increase in R-ion radii. We predict that for a particular R-ion radius (~1.10Å), rate of change in distortion will be zero and with increasing the R-ion radii further, distortions reduce with pressure. This explains why only LaCrO$_3$ undergoes a structural phase transition to a less distorted phase at higher pressure. The confinement of *R*-ion inside RO_{12} polyhedra plays a crucial role in pressure induced effects on octahedral distortions in perovskite lattice. When *R*-ion is less confined in RO_{12} and with pressure RO_{12} compresses significantly leading to a more distorted structure. Conversely, when *R*-ion is strongly confined inside RO_{12} (less distorted structure) and with pressure RO_{12} compresses less leading to a less distorted structure. This effect was clearly explained from the analysis of pressure dependence of $A_g(1)$ and $A_g(7)$ Raman modes as well as Cr-O bond lengths derived from synchrotron powder x-ray diffraction. The critical rare-earth ion radii predicted from the pressure dependence of cell distortion factor matches well with Raman results. The rare-earth size dependency of $\frac{dT_N^{Cr}}{dP}$ which involves an explicit relation between octahedral bond lengths, tilt angles and T_N^{Cr}. Our analysis suggests that unlike the case of chemical pressure (change in R-ion radii) where change in T_N^{Cr} is mainly due to change in octahedral tilts, in the case of external pressure compressions at Cr-O play dominating role over octahedral tilts in pressure dependent change in T_N^{Cr}. A model calculation to generalize rare-earth size dependence of the pressure induced softmode frequency change (e.g. $\Delta A_g(3)$ and $\Delta A_g(4)$ in $RCrO_3$) would be an interesting future direction to this work.

List of publications relevant to this thesis:

1. M. Viswanathan, P.S. Anil Kumar, **Venkata Srinu Bhadram**, Chandrabhas Narayana, A. K. Bera, S.M. Yusuf. “Influence of lattice distortion on Curie temperature and spin-phonon coupling in $LaCo_{0.5}Mn_{0.5}O_3$”. *J. Phys. Condens. Matter.*, 22, 346006 (2010).

2. Kaustuv Manna, **Venkata Srinu Bhadram**, Chandrabhas Narayana and P. S. Anil Kumar, “Octahedral distortion induced magnetic anomalies in $LaCo_{0.5}Mn_{0.5}O_3$ single crystals” (submitted).

3. **Venkata Srinu Bhadram**, B. Rajeswaran, A. Sundaresan and Chandrabhas Narayana, “Spin-phonon coupling in multiferroic RCrO$_3$ (R-Y, Lu, Gd, Eu, Sm): A Raman study”, *Europhys. Lett.*, 101, 17008 (2013).

4. **Venkata Srinu Bhadram,** Diptikanta Swain, R Dhanya, A. Sundaresan and Chandrabhas Narayana, “Effect of pressure on octahedral distortions in rare-earth chromites (RCrO$_3$): role of R-ion size and its implications” (submitted).

Other miscellaneous work:

1. Diptikanta Swain, **Venkata Srinu Bhadram**, Gopal K Pradhan, Venkata Prasad Bhat, Chandrabhas Narayana, C. N. R. Rao. “Superionic phase transition in $KHSO_4$: A temperature dependent Raman investigation”. *J. Phys. Chem. A.*, 114, 10040 (2010).

2. S. Murugavel, C. Vaid, **Venkata Srinu Bhadram**, Chandrabhas Narayana. “Ionic transport mechanism in glasses: Non-Arrhenius conductivity and nonuniversal features”. *J. Phys. Chem. B*, 114, 13381 (2010).

3. T. Bhuvana, A. Kumar, A. Sood, R.H. Gerzeski, J. Hu, **Venkata Srinu Bhadram**, Chandrabhas Narayana, Timothy S. Fisher. “Contiguous petal-like outgrowths from graphite fibers by plasma CVD”. *ACS Appl. Mater. Inter.*, 2, 644 (2010).

4. P. Mandal, **Venkata Srinu Bhadram**, Y. Sundarayya, Chandrabhas Narayana, A. Sundaresan and C.N.R. Rao, “Spin-Reorientation, Ferroelectricity, and Magnetodielectric Effect in $YFe_{1-x}Mn_xO_3$ ($0.1 \leq x \leq 0.40$)”, *Phys. Rev. Lett.*, 107, 137202 (2011).

5. Supti Das, **Venkata Srinu Bhadram**, Chandrabhas Narayana and Aninda J. Bhattacharyya, “Brillouin Scattering Investigation of Solvation Dynamics in Succinonitrile-Lithium Salt Plastic Crystalline Electrolytes”, *J. Phys. Chem. B,* 115, 12356 (2011).

6. Diptikanta Swain, **Venkata Srinu Bhadram**, Papia Chowdhury and Chandrabhas Narayana, “Raman and x-ray Investigations of Ferroelectric Phase Transitions in NH_4HSO_4”, *J. Phys. Chem. A,* 116, 230 (2012).

7. Narendra Kurra, **Venkata Srinu Bhadram**, Chandrabhas Narayana and G.U. Kulkarni, “Field effect transistors based on graphitized patterns of carbon contamination”, *ACS Appl. Mater. Inter.,* 4, 1030 (2012).

8. Narendra Kurra, **Venkata Srinu Bhadram**, Chandrabhas Narayana and G.U. Kulkarni, “Field effect transistors and photodetectors based on nanocrystalline graphene derived from electron beam induced carbonaceous patterns”, *Nanotechnology*, 23, 425301 (2012).

9. Narendra Kurra, **Venkata Srinu Bhadram**, Chandrabhas Narayana and G.U. Kulkarni, “Few layer graphene to graphitic films: Infrared photoconductive versus bolometric response”, *Nanoscale***,** 5, 381 (2013).

10. Nidhi Singla, **Venkata Srinu Bhadram** , Chandrabhas Narayana and Papia Chowdhury, “White light generation by carbonyl based indole derivatives due to proton transfer: An efficient fluorescence sensor” *J. Phys. Chem. A, 117,* 2738 (2013).

11. Diptikanta Swain, **Venkata Srinu Bhadram**, Gopal K Pradhan, Chandrabhas Narayana, “High pressure Raman investigations of ferroelectric transition in $RbHSO_4$” (submitted).